TESI DI DOTTORATO

UNIVERSITÀ DEGLI STUDI DI NAPOLI "FEDERICO II"

DIPARTIMENTO DI INGEGNERIA ELETTRICA
E DELLE TECNOLOGIE DELL'INFORMAZIONE

DOTTORATO DI RICERCA IN
INGEGNERIA ELETTRONICA E DELLE TELECOMUNICAZIONI

HIGH GRANULARITY APPROACHES FOR EFFECTIVE ENERGY DELIVERY FROM PHOTOVOLTAIC SOURCES

FABIO DI NAPOLI

Il coordinatore del Corso di Dottorato

Ch.mo Prof. Daniele RICCIO

I Tutori

Ch.mo Prof. Santolo DALIENTO

Ch.mo Prof. Diego IANNUZZI

Anno Accademico 2015-2016

a mio Padre,
a mia Madre,
alla famiglia Fumo,
a Zia Amelia,
a Zia Maria,
ai miei Nonni.

Table of contents

Table of figures

Chapter 1

1 Introduction

1.1 Aims of the work

Silicon solar cell technology is a mature technology. The current record efficiency of about 24% was already reached more than 20 years ago [1]. Very few progresses are expected so far since this value is very close to the theoretical limit [2]. For solar panels the record is about 22% [3]. These values of efficiency have been high enough for sustaining the impressive growth of the solar market in the past few years, but the need to compete with other energy sources, both traditional and renewable ones, urges to improve the overall efficiency of a solar system by a more significant amount. Independently of the solar module efficiency, there is a quite high gap, in the order of 20%, between the nominal performance of a solar system and the energy actually produced. The above number groups all possible energy loss terms and is referred as Balance Of System (BOS). It is obvious that the improvement margin given by the reduction of the aforementioned difference is, at least, as large as possible enhancements coming from silicon cell technology. Energy losses attributable to the system comprise, inverter conversion efficiency, mismatch losses, ohmic losses along wiring cables and so on. Among them an often underestimated loss term depends on possible failures of the Maximum Power Point Tracking (MPPT) algorithms. MPPTs have the aim to extract from the solar system the maximum available power dynamically determined. However the algorithm may fail by stabilizing the system at a local maximum instead of the global one, when the output power voltage (P-V) characteristic of the photovoltaic (PV) system exhibits multiple maximum power points.

A PV plant is composed by a great number of elemental PV cells series interconnected thus a unique current flows through the system; this configuration implies as a consequence that a single malfunctioning cell can limit the current affecting the power yield of the whole system. It is worth noting that the term "malfunctioning" has more meanings, it not only applies to real damaged cells but to all conditions where a single cell provides less current than others. This is the case when solar panels are partially shaded thus the solar radiation intensity is not uniform over the panels [4]-[5]. The above "bottleneck effect" is partially solved by inserting bypass power diodes, which ensure that the maximum current supplied by the system is not limited by the worst cell, giving freewheeling current paths. However the activation of bypass diodes introduces strong distortion of the power-voltage characteristic of the system and unavoidable yield losses [6].

Presence of "malfunctioning" is extremely common in many PV plants yet installed, because poorly skilled designers were often involved in their project. An aggressive feed-in tariffs policy has sustained the impressive growth of the PV system during the last years, but with the rapid decrease in the government subsidies an insane haste in plants installation has been generated, resulting in many PV plant no well designed, thus leading to unexpected yield degradations. For these reasons, the budget plans of many PV customers have been compromised because their PV plants are experiencing unsatisfactory energy yields. Therefore effective and innovative monitoring and diagnostic strategies along with new power conversion topologies, aimed to improve system reliability and efficiency, have become fields of interest for the PV market.

In order to better understand how the P-V characteristic of a PV plant is affected by multiple MPPs, an investigation of the limiting factors related to architectural shadow is required. This situation is representative of a large variety of practical cases since many kinds of solar module faults cause reduced current capability. For the sake of simplicity a solar system composed by only two solar panels is considered, each of them protected by an individual bypass diode as schematically shown in Fig 1.1.

Fig 1.1 also shows a shadow, covering part of a solar panel. I-V and P-V curves of the above system are shown in Fig 1.2, their shapes, for a given current photogenerated by the sunny cells, depend on the current delivered by the shaded cells due to the bottleneck effect.

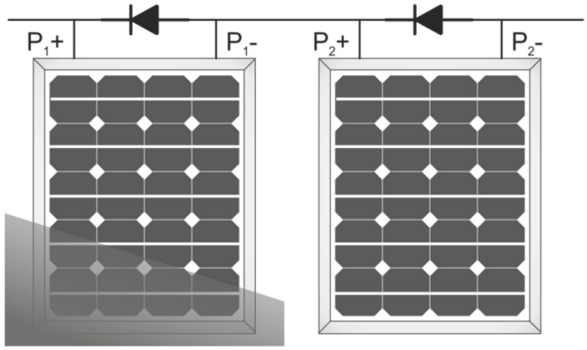

Fig 1.1 Two series connected solar modules with a shaded part.

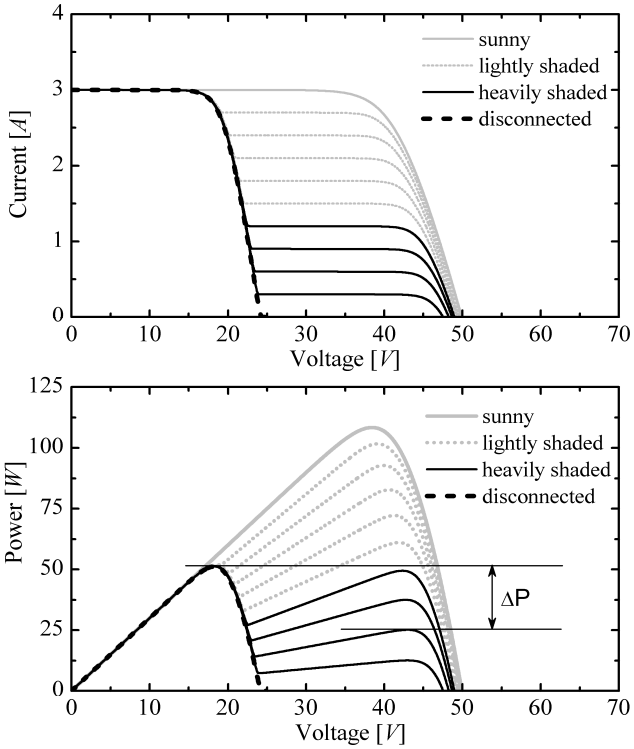

Fig 1.2 I-V and P-V curves of the two PV modules in Fig 1.1.

The effect of a partial shading is a strong deformation of both P-V and I-V characteristics. The intervention of the bypass diodes avoids the reduction of the current of the whole system. The current delivered by the system equals the sunny cell current because the bypass diodes of the shaded cells are turned on. The diodes turn off

when, increasing the voltage, the sunny cell current is the same of the shaded ones. For those voltages the I-V curve becomes almost coincident with that of a completely shaded system; as consequence the P-V characteristics (Fig 1.2b) exhibit MPPs with peaks power that can be strongly reduced with respect to the sunny module.

The power produced by the full illuminated system, namely the peak of the curve indicated as "sunny" in Fig 1.2b can never be recovered because the only way to regain that power value is to eliminate the shadow by simply rearranging the PV system. However an additional loss could arise because it may happen that the MPP tracking system does not recognize the absolute MPP and stabilizes the PV plant operating point in the local MPP. The gap Δp in Fig 1.2b, between the global MPP and the local one is a power loss entirely ascribable to a MPPT fault. This potential fault happens when the PV field is "heavily shaded" so that the maximum on the right side is lower than the maximum on the left side, which is also the one more likely tracked by the MPPT. This occurrence is not a rare event because, even in a bright day, when a solar cell is shaded it only receives the diffused (the one scattered by the surrounding environment) light which is about the 20% of the global (direct plus diffused) light, thus heavily mismatch conditions are generated. It is worth noting that, when the system works at the right side local maximum of Fig 1.2b, the bypass diode corresponding to the shaded panel is in the OFF state. That local maximum could be eliminated from the PV plant characteristic by simply forcing the bypass diode to be ON. Indeed, in this case the curve would be the one indicated as "disconnected" in Fig 1.2 and the MPPT would straightforward track the single absolute maximum. In such condition the P-V curve could be brought back to a single maximum one thanks to a PV plant reconfiguration.

The PV field reconfiguration is not the only method able to decrease these losses, but other solutions, adopted at different levels of a PV system, are presented in literature. This work proposes new strategies to maximize the energy produced by a PV system in all conditions. A PV system, like the other renewable sources is distributed, even if this concept is stressed in a PV plant which is made by thousands of independent sources. This implies two main drawbacks: (i) a PV plant properly operates only in uniform condition and (ii) the diagnostic is quite complex. Fig 1.3 shows a medium size PV plant, it should be noted that in such system is really hard to

guarantee uniform operating conditions, moreover to find a malfunctioning cell is extremely onerous.

Fig 1.3 Example of a PV plant, the red lines indicate respectively a single PV cell and one PV string.

The losses occurring in mismatch conditions depending on the behavior of each single PV source and on the way in which they interact with the power conversion interface. An effective way to improve the efficiency of the whole system is *the monitoring, the modeling and the power conversion at level of the single PV source*. For these reasons all solutions proposed in this work are based on the concept of "high granularity".

The meaning high granularity involves different approaches depending on the level at which these approaches are exploited; anyway the common element of all these solutions is to analyze the PV system as a distributed power source. It is worth noting that the analysis of a PV plant performed at level of each distributed source is the only correct way to investigate it, but it requires much more effort and there have been no effective means so far to accomplish this task. The traditional power conversion approaches and the monitoring ones operate in such a way that the PV plant is observed as a centralized source, for this reason great power losses are experienced in mismatch conditions.

The approaches presented in this work will also perform a second task, providing solutions for some issues and questions which have not been solved by the PV literature so far:

1) How can I find effectively where the problem is located in a PV field?

2) Can I access to a PV field safely?
3) Why my PV field does not provide the return of money I expected?
4) Which is the best power conversion topology in terms of cost and energy yield?
5) Is there a high modular high granularity conversion topology to improve my energy yield?

All these issues depend on the structure of a PV field and its behavior in mismatch conditions.

PV plant high granularity monitoring can make simple the process of locating of malfunctioning cells, while the proposed reconfiguration can ensure safe access to a PV plant. The proposed reconfiguration implies the disconnection of each PV module thus it can solve a potentially harmful risk related to the fact that a PV plant cannot be switched off as long as sunlight reaches solar panels, since the series connection of solar panels generates hundreds Volts during daylight, which exceeds the safety human body threshold. Moreover the combination of these two strategies can reduce the losses related to MPPT faults.

PV plant high granularity modeling can ensure more precise energy yield estimations with respect the commercial software typically employed in PV field design. The proposed model is embedded in an automatic tool which evaluates the yield of the PV plant accounting for potential mismatch effects due to its location and its structure; moreover it describes the PV system like a distributed power source providing analysis required to find the proper conversion topology for a given PV field.

PV field high granularity conversion implies distributed power conversion topology which performs individual MPPT for each PV source. The microinverters perform an individual MPPT for each solar panel; even if they ensure the best MPPT efficiency, avoiding the power losses occurring in mismatch conditions, they did not have success in the PV market. The reason is a trade-off arising in case of large PV plant when also the costs of this conversion topology are taken into account. In this scenario this work proposes a new high granularity high modular conversion topology which can split the PV field in different section made by a different number of PV modules in order to provide the best solution in terms of costs and energy yield.

1.2 State of art

The PV literature has proposed so far solutions in all three aforementioned fields; in the following section a brief overview is presented.

All monitoring approaches, which have been presented so far, operate at "low granularity" level, namely strings, arrays or subplants. They erroneously assume that each problem arising at a panel level propagates to a larger plant portion, and therefore even a "low-granularity" monitoring system can, in principle, detect its effect and that PV panels have a relatively low fault probability (about 15% of the PV system failures [7]) in their life-cycle. These low granularity monitoring systems do not allow indentifying the location of malfunctioning panels and costly in-situ inspection are then required. A rough malfunctioning detection is usually preferred by PV owners without taking into account the additional costs of the process of locating the faults. A subplant-level monitoring approach is presented in [8], [9], this system detects differences between the producible power, estimated by a global model exploiting real-time irradiation and temperature measurements, and the actually produced PV power. Power losses can be identified by comparing performances corresponding to different sections of the PV plant through an inferential algorithm [10], [11], heuristic models [12], and even neural networks [13]. Moreover, in [14] an AC electrical characterization of a PV string is performed in order to detect hot spotting. However, medium/high power plants have a great number of panels which can reach the value of many thousands, thus making fault localization extremely complex, increasing the possibility of maintenance query. Thermographic/visual inspection [15] provides an accurate detection of defects and faults in PV plants. In this case, thermal and visual digital images, collected by light unmanned aerial vehicles equipped with thermal and visual cameras, are exploited to identify the malfunctioning panels by means of pattern recognition methods. The time domain reflectometry technique [16] also provides accurate results, it exploits a voltage signal applied to the PV string and it observes the signal response waveforms in order to locate the fault position. In [17] a fault detection and classification method relying on a temperature distribution analysis is proposed. Unfortunately, these approaches cannot quantify the energy loss due to each issue and, consequently, the returns on maintenance investments, moreover they

are not suitable for real-time monitoring. Real-time "high-granularity" approaches relying on sensors applied to individual PV panels ensure a more effective localization of faults and more accurate estimation of yield degradation. For instance, an accurate power loss mapping can be achieved by equipping the panels with individual DC power optimizers, as described in [18]. In this case the method is based on the assumption that the optimizer always reaches the maximum power point (MPP), thus the energy loss estimation is performed by comparing each panel with the best performing one in the plant in terms of energy production. However, two drawbacks affect this method: first, DC power optimizers may not be compatible with old-generation inverters, thus being often inadequate for the monitoring of already-installed plants; second, it leads to an increase in system complexity and costs.

As underlined in the question number 2, the energy yield evaluation performed during the design of a PV plant is affected by a great discrepancy with respect to the value actually obtained, not ascribable to wrong weather forecasts. Commercial tools adopt approaches to estimate the energy yield which do not take properly into account the effect of shadows due to the following reasons: (i) they are not equipped with a power graphic interface which provides an easy method to represent all architectural structures generating shadow pattern upon the PV modules (i.e., TV antenna, chimneys, poles); (ii) they do not employ high granularity models which describe the PV plant at single cell level; (iii) they do not take into account the electrothermal processes taking place inside a PV panel, which modify the temperature so the behaviour of each cell. For these reasons, in order to optimize the design of a PV plant prior to installation along with the conversion system and for a diagnostic of already installed plants, it is mandatory to evaluate correctly the impact of architectural shading. Various approaches have been proposed in the literature to quantify shading-induced losses, which rely on numerical solution methods handled by e.g., Matlab, Simulink, or a combination of the two. As reported in [19]-[23], the analysis are performed with subpanel/panel-level discretization, which means that a solar panel is described at a subpanel granularity level, in the sense that, instead of the solar cell, the elemental unit to construct a complex system is the series of solar cells protected by a bypass diode. Anyway this approach is not suited to capture the impact of small-area shadows, which are often appreciable and not taken properly into account by the

common belief. In most cases all above models lead to acceptable yield estimation since well designed PV systems are only interested by large temporary shadows. The discrepancies arise when small objects are present, as it is usual in domestic applications or not well designed PV plants. Examples of high resolution cell level discretization are discussed in [24]-[26], in these cases a description of a no uniformly illuminated subpanels is possible, but the methods are too computationally demanding in terms of both memory and CPU time.

The answer of question number 4 is not simple to find because different conversion topologies can be employed in grid-tied PV plant. A PV inverter has to manage energy exchange between solar modules and grid, by guarantying maximum conversion efficiency and high quality of the current injected into the grid, in terms of total harmonic distortion and power factor. The first task is performed through MPPT algorithms exploited in several power conversion topologies. Four main topologies are described in [27], [28]: centralized topology, string and multi-string topology, AC-module topology. The centralize topology is nowadays considered obsolete, in this configuration all PV modules are connected to a single converter which tries to track the MPP of the whole plant, thus minimizing the number of power devices. Under mismatch conditions this topology does not exhibit efficient power conversion. In the string and multi-string approach the solar array is split into several subsections, each equipped with a dedicated MPPT, so that the power losses only affect the section where the mismatch condition occurs. These converters usually consist of two power stages: a front stage made by a boost dc-dc converter, (or more than one parallel connected in case of multi-string), which gets the sufficient dc-bus voltage and performs the MPPT, and an inverter as second stage, which generates the ac output current. The AC-module topology stresses the concept of the multi-string approach, performing the MPPT for each solar module, thus providing the best MPPT efficiency [29]-[31]. The microinverters belong to this class and the main drawback of this converter is the higher voltage gain required to connect a single panel to the grid with respect to the other topologies. This gain is ensured through two stages or a step transformer, so increasing the power conversion losses, which are replicated for each panel. For this reason this solution did not obtained a great success and the efforts have been focused on alternative single stage AC-module converter which provides higher gain as in [29].

1.3 Outline

The work is organized as follow, in the first chapter a new high granularity monitoring and dynamic reconfiguration system is presented, it adopts innovative solution with respect to the other systems presented in literature and it overcomes some security issues related with the structure of a PV system. Fig 1.4 shows a prototype of the PV sensor adopted to exploit the proposed high granularity monitoring strategy.

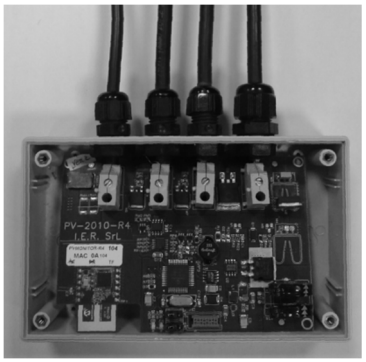

Fig 1.4 Prototype of the proposed high granularity monitoring PV sensor.

In the second chapter an automated high granularity tool developed for fast evaluations of PV plant energy yield, taking into account mismatch conditions and electrothermal effects, is described. It translates an AutoCAD PV plant project, with information about the surrounding environmental, in an electrical circuit netlist describing the whole PV plant at level of single solar cell and exploitable to perform PSpice simulations. Fig 1.5 illustrates, with a simplified block diagram, the proposed tool.

In the third chapter an innovative converter topology, which overcomes the issues related with the microinverter while ensuring the advantages of a distributed power conversion, is investigated. The topology under exam is the Cascaded H-bridge (CHB) multilevel converter topology, its potential use as distributed power converter in PV application is analyzed and an innovative control strategy is proposed.

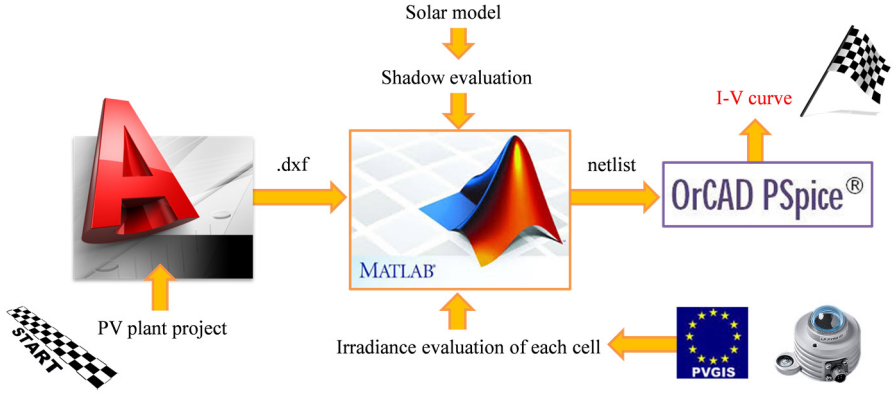

Fig 1.5 Block diagram of the developed tool performing high granularity modeling of a PV plant.

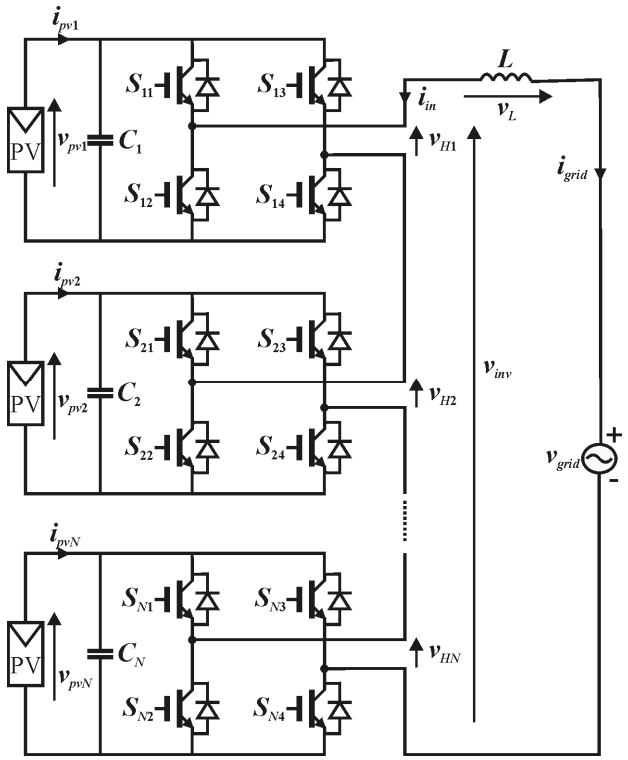

Fig 1.6 Schematic of the single phase CHB multilevel converter.

The schematic of the CHB converter is depicted in Fig 1.6 Conclusion and acknowledgment are drawn in the last section.

1.4 References

[1] J. Zhao, A. Wang, P.P. Altermatt, S.R. Wenham, and M.A. Green, "24% efficient silicon solar cells," in Proc. IEEE Photovoltaic Specialists Conference on Photovoltaic Energy Conversion - IEEE First World Conference on Photovoltaic Energy Conversion, vol. 2, pp. 1477-1480.

[2] W. Shockley e H. J. Queisser, "Detailed balance limit of efficiency of p-n junction solar cells," Journal of Applied Physics, vol. 32, no. 3, pp. 510-519, 1961.

[3] Datasheet "Photovoltaic Module X Series", available online at http://www.sunpowercorp.com.

[4] A. Woyte, J. Nijs, and R. Belmans, "Partial shadowing of photovoltaic arrays with different system configurations: literature review and field test results," Solar Energy, vol. 74, no. 3, pp. 217-233, 2003.

[5] A. Kajihara and T. Harakawa, "Model of photovoltaic cell circuits under partial shading," in Proc. IEEE International Conference on Industrial Technology (ICIT), 2005, pp. 866-870.

[6] M. C. Di Piazza and G. Vitale, "Photovoltaic field emulation including dynamic and partial shadow conditions," Applied Energy, vol. 87, no. 3, pp. 814-823, 2010.

[7] U. Jahn and W. Nasse, "Operational performance of grid-connected PV systems on buildings in Germany," Progress in Photovoltaics: Research and Applications, vol. 12, no. 6, pp. 441-448, 2004.

[8] M. Benghanem and A. Maafi, "Data acquisition system for photovoltaic systems performance monitoring," IEEE Trans. Instrumentation and Measurement, vol. 47, no. 1, pp. 30-33, Feb. 1998.

[9] N. Forero, J. Hernández, and G. Gordillo, "Development of a monitoring system for a PV solar plant," Energy Conversion and Management, vol. 47, no. 15-16, pp. 2329-2336, 2006.

[10] S. Vergura, G. Acciani, V. Amoruso, and G.E. Patrono, "Inferential statistics for monitoring and fault forecasting of PV plants," in Proc. IEEE ISIE, 2008, pp. 2414-2419.

[11] S. Vergura, G. Acciani, V. Amoruso, G. E. Patrono, and F. Vacca, "Descriptive and inferential statistics for supervising and monitoring the

operation of PV plants," IEEE Trans. Industrial Electronics, vol. 56, no. 11, pp. 4456-4464, Nov. 2009.

[12] B.-K. Kang, S.-T. Kim, S.-H. Bae, and J.-W. Park, "Diagnosis of output power lowering in a PV array by using the Kalman-Filter algorithm," IEEE Trans. Energy Conversion, vol. 27, no. 4, pp. 885-894, Dec. 2012.

[13] S. Syafaruddin, E. Karatepe, and T. Hiyama, "Controlling of artificial neural network for fault diagnosis of photovoltaic array," in Proc. ISAP, 2011, pp. 1-6.

[14] K. A. Kim, G.-S. Seo, B.-H. Cho, and P. T. Krein, "Photovoltaic hot spot detection for solar panel substrings using AC parameter characterization," IEEE Trans. Power Electronics (in press); DOI: 10.1109/TPEL.2015.2417548.

[15] P. B. Quater, F. Grimaccia, S. Leva, M. Mussetta, and M. Aghaei, "Light unmanned aerial vehicles (UAVs) for cooperative inspection of PV plants," IEEE Journal of Photovoltaics, vol. 4, no. 4, pp. 1107-1113, Jul. 2014.

[16] T. Takashima, J. Yamaguchi, and I. Masayoshi, "Fault detection by signal response in PV module strings," in Proc. IEEE Photovoltaic Specialists Conference, 2008, pp. 1-5.

[17] Y. Hu, W. Cao, J. Ma, S. J. Finney, and D. Li, "Identifying PV module mismatch faults by a thermography-based temperature distribution analysis," IEEE Trans. Device and Materials Reliability, vol. 14, no. 4, pp. 951-960, Dec. 2014.

[18] A. J. Hanson, C. A. Deline, S. M. MacAlpine, J. T. Stauth, and C. R. Sullivan, "Partial-shading assessment of photovoltaic installations via module-level monitoring," IEEE Journal of Photovoltaics, vol. 4, no. 6, pp. 1618-1624, Nov. 2014.

[19] H. Patel and V. Agarwal, "MATLAB-based modeling to study the effects of partial shading on PV array characteristics," IEEE Transactions on Energy Conversion, vol. 23, no. 1, pp. 302-310, 2008.

[20] A. Mäki, S. Valkealahti, and J. Leppäaho, "Operation of series-connected silicon-based photovoltaic modules under partial shading conditions," Progress in Photovoltaics: Research and Applications, vol. 20, no. 3, pp. 298-309, 2012.

[21] B. Celik, E. Karatepe, N. Gokmen, and S. Silvestre, "A virtual reality study of surrounding obstacles on BIPV systems for estimation of

long-term performance of partially shaded PV arrays," Renewable Energy, vol. 60, pp. 402-414, 2013.

[22] H.-L. Tsai, "Insolation-oriented model of photovoltaic module using Matlab/Simulink," Solar Energy, vol. 84, no. 7, pp. 1318-1326, 2010.

[23] K. Ishaque, Z. Salam, and Syafaruddin, "A comprehensive MATLAB Simulink PV system simulator with partial shading capability based on two-diode model," Solar Energy, vol. 85, no. 9, pp. 2217-2227, 2011.

[24] A. Woyte, J. Nijs, and R. Belmans, "Partial shadowing of photovoltaic arrays with different system configurations: literature review and field test results," Solar Energy, vol. 74, no. 3, pp. 217-233, 2003.

[25] V. Quaschning and R. Hanitsch, "Numerical simulation of current–voltage characteristics of photovoltaic systems with shaded solar cells," Solar Energy, vol. 56, no. 6, pp. 513-520, 1996.

[26] M. C. Alonso-García, J. M. Ruiz, and W. Herrmann, "Computer simulation of shading effects in photovoltaic arrays," Renewable Energy, vol. 31, no. 12, pp. 1986-1993, 2006.

[27] S. B. Kjaer, et al. ,"A Review of Single-Phase Grid-Connected Inverters for Photovoltaic Modules," IEEE Trans. on Industry Applications, vol. 41, no. 5, pp. 1292-1306, Sept. 2005.

[28] S. Kouro, B. Wu, A. Moya, E. Villanueva, P. Correa, J. Rodriguez, "Control of a cascaded H-bridge multilevel converter for grid connection of photovoltaic systems," IECON, 2009, pp.3976-3982.

[29] M. Coppola, P. Guerriero, F. Di Napoli, S. Daliento, D. Lauria, and A. Del Pizzo, "A PV AC-module based on coupled-inductors boost DC/AC converter," in Proc. International Symposium on Power Electronics, Electrical Drives, Automation and Motion (SPEEDAM) 2014, pp. 1015-1020, June 2014.

[30] D. Meneses, F. Blaabjerg, O. García, J.A. Cobos, "Review and Comparison of Step-Up Transformerless Topologies for Photovoltaic AC-Module Application,", IEEE Transactions on Power Electronics, vol.28, no.6, pp.2649-2663, June 2013.

[31] T.K.S. Freddy, N.A. Rahim, H. Wooi-Ping, Hang Seng Che, "Comparison and Analysis of Single-Phase Transformerless Grid-Connected PV Inverters," IEEE Transactions on Power Electronics, vol.29, no.10, pp.5358-5369, Oct. 2014.

Chapter 2

2 High granularity monitoring and diagnostics of PV plants

2.1 Proposed strategy

The proposed high granularity approach is based on innovative monitoring circuits (hereinafter also referred to as “sensors”) mounted on selected host panels for the real-time detection of their operating points [7], [8].

The innovative characteristic with respect to other PV module sensors investigated in e.g., [1]-[6] is the possibility to perform a set of measurements which completely describes the PV panel behavior, namely the open circuit voltage V_{oc}, the short circuit current I_{sc}, the operating voltage V_{panel} and current I_{panel}. The first two measurements are performed by electronically disconnecting the host PV module from the string. The sensor is also equipped with an improved disconnection system to prevent thermal issues under bypass conditions. The proposed sensor can be considered as an electronic frame of the host panel and offers the following features: (i) Accurate detection and localization of degradation issues through the monitoring of I_{sc}; (ii) detailed yield mapping by analyzing the operating points of individual panels [9]; (iii) the measurement of V_{panel} ensures automatic detection and localization of bypass events; (iv) reliable real-time estimation of the maximum producible power of a string by exploiting the model proposed in [10]; (v) quantification of the yield improvements that could be achieved with a proper maintenance/upgrading, thus allowing easy comparison between investments and revenue; (vi) solution to security [12] issues and reliability [11].

2.2 The PV sensor structure

Fig 2.1 illustrates the schematic block diagram of the proposed sensor, which is composed by micro-controller unit (MCU), wireless communication, disconnection system, measurement circuit, power supply section comprising charge circuit, energy storage device (ESD), and DC/DC converter. A consecutive upgrade of the sensor is the integration of a power line communication (PLC) interface which ensures the communication between the sensors through the DC bus where the PV modules are series connected. Each section will be described in detail in the following along with the PLC interface upgrade.

It should be underlined that the host PV panel terminals (P+ and P-) are connected to the sensor, while the sensor terminals (S- and S+) are connected to the adjacent panels of the string. Between P- and S+ a controlled electronic switch separates the panel from the string. Since P- has always the lowest potential in the whole circuit, it is chosen as the electrical reference of the sensor.

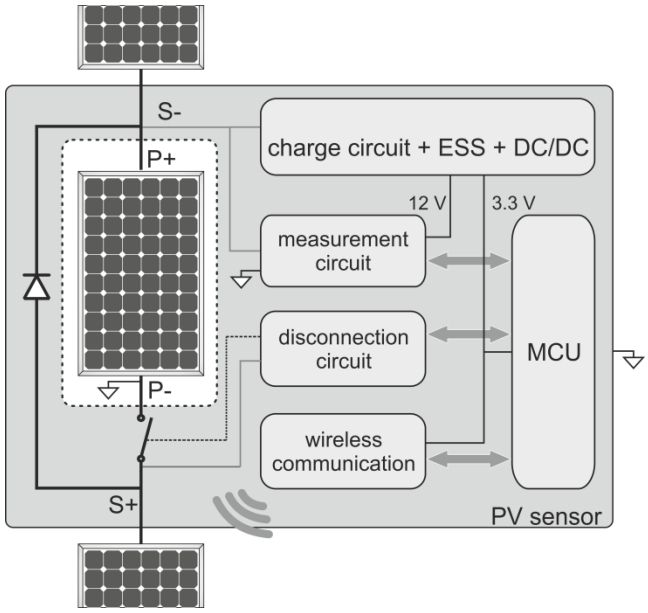

Fig 2.1 Schematic block diagram of the proposed PV sensor.

Both the aforementioned switch and the bypass diode, named D_1 in the Fig 2.2, in parallel to the branch including panel and switch,

are exploited during the disconnection. The switch inhibits the current flow through the panel, while the bypass diode provides an alternative path to the string current I_{string}, thus preventing the interruption of the energy generation. The switch is a power Mosfet referred to as M_1, and its driving circuit is sketched in Fig 2.2.

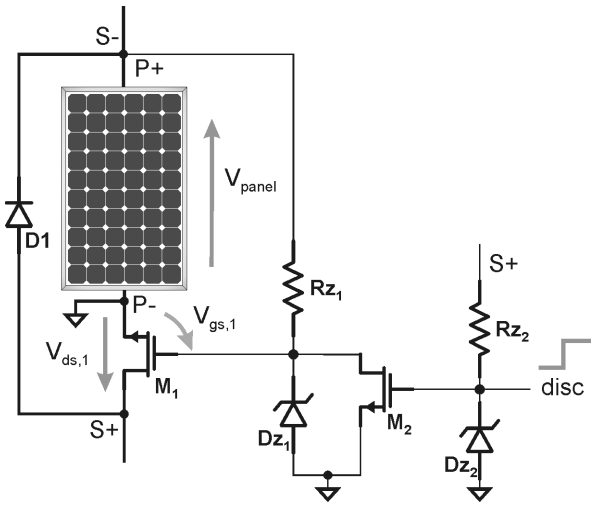

Fig 2.2 Schematic diagram of the disconnection circuit.

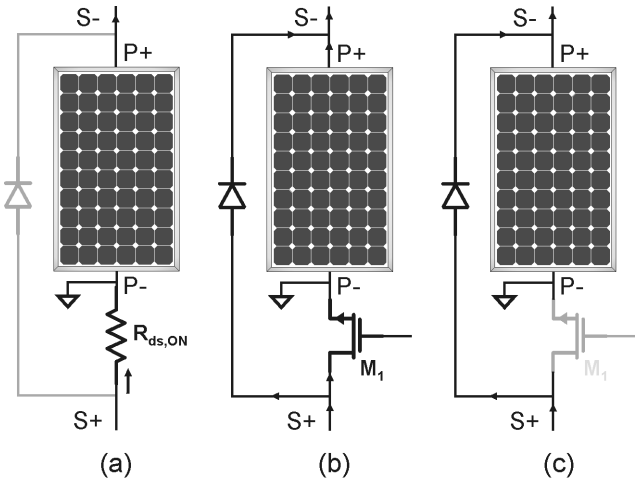

Fig 2.3 Operating modes: (a) normal operation, (b) bypass conditions under mismatch, and (c) disconnection.

The system PV module plus sensor can work in three operating modes, illustrated in Fig 2.3. In particular, Fig 2.3a depicts the normal

operating mode. In this condition the panel is under full irradiation and conducts the whole I_{string}. Most likely it works near the MPP thanks to the inverter tracking algorithm, thus keeping D_1 reverse biased. The panel voltage is high enough to force the Zener diode D_{z1} shown in Fig 2.2 to work at its breakdown voltage (4.7 V), thereby making M_1 operate in the ON state with a negligible voltage drop ($R_{ds,ON}$ is about 5 mΩ).

It is worth noting that V_{panel} never reaches a negative value, i.e., the panel still generates power that is instead dissipated by M_1 [11].

The bypass operating mode is fully reversible, that is, when the irradiance increases and the panel current grows to reach the string current, V_{panel} increases as well, while $V_{ds,1}$ decreases, thus restoring the operating condition described in Fig 2.3a. Under bypass conditions, both V_{panel} and $V_{ds,1}$ are about 2-3 V. Such a low V_{panel} can inhibit power supplying to the sensor; moreover, the sensor might be damaged due to the high dissipation of the MOS transistor. These issues are resolved by a detection of the bypass occurrences and automatically forcing the panel in the disconnection mode shown in Fig 2.3c; for this purpose the power Mosfet M_2 forces the M_1 gate to zero, disconnecting the panel from the string. In this operating condition it is possible to perform reliable measurements of V_{oc} and I_{sc} of the host panel.

The activation of M_2 is forced when $V_{ds,1}$ increases by exploiting the positive feedback of the branch comprising R_{z2} and D_{z2} reported in Fig 2.2. Unfortunately, this operating mode is a stable condition because the panel remains disconnected even if the mismatch event is over. In order to avoid this issue, the MCU periodically applies a digital stimulus (disc in Fig 2.2) trying to force the system in normal mode. When the MCU senses an increase in $V_{ds,1}$ (bypass detection), it sets disc to keep M_2 ON, thereby disconnecting the panel. Afterward the MCU periodically puts disc to 0 in order to let the panel return to normal mode. If the panel remains bypassed ($V_{ds,1}$ still high), disc is set again. In normal operating conditions, the corresponding MCU output is disabled (high impedance status), thus not affecting the circuit behavior.

Through this circuit is also possible to disconnect the panel on demand in spite of its operating condition, this feature improves PV system reliability and safety [12].

As in [1]-[3], [5], each sensor is supplied by the corresponding host panel thus avoiding additional cables. The operating area of the sensor must cover the whole I-V curve for a wide range of temperature and irradiance levels, even under partial shading conditions. In other words the power supply section should be able to work properly in spite of the operating point imposed to the panel by the inverter MPP tracking. Moreover an ESD is mandatory in order to guarantee energy to the PV sensor during the measurement phase (when the panel is isolated for V_{oc} and I_{sc} measurements).

As shown in Fig 2.4, the proposed power supply section is composed by two stages, and it overcomes some issues presented in previous works. For instance in [13]-[15], wireless sensors are powered by small PV panels according to traditional energy harvesting approaches. These sensors exploit DC-DC converters with dedicated MPPT to adjust the operating point of the panel according to the energy requirements of the overall circuit. Such a strategy is not suitable for the proposed application because the operating point is fixed by the inverter MPPT. In this case linear voltage regulators are adopted (i.e., [1]-[3], [5]). However also this solution suffers of a drawback due to the narrow input voltage range of the regulators which can cause the sensor to turn off in case of partial shading, MPPT failures, and bypass. Those sensors could in principle turn OFF just when they should detect a malfunctioning event.

The proposed solution is composed by a first stage, which consists of a voltage regulator offering a suitable voltage level to the ESD and providing energy to the second stage. The voltage regulator comprises R_{z3}, D_{z3} and M_{pwr}, while the ESD is a 2 F supercapacitor denoted as SuperCap. This stage is directly connected to the panel terminals. The driving network R_{z3}/D_{z3} is devised to charge the SuperCap to a voltage level of about 3 V, the charge voltage is limited by the D_{z3} threshold (4.7 V), the gate-source voltage of M_{pwr} (typically 1.5 V), and the voltage drop across the 10 Ω resistor R_{lim}. At the sensor start-up when the ESD is completely discharged, R_{lim} limits the charge current to 300 mA, thus preventing the overheating of M_{pwr}.

The second stage consists of integrated DC-DC step-up converters with an input voltage range between 1.8 to 3.3 V. In normal operation (SuperCap voltage equals to 3 V), the second stage derives a current of 25 mA to feed the circuit. The ESD must mainly operate as a back-up energy storage element during the measurement phase which takes up to 10 ms. During this period, M_{pwr} is

intentionally switched OFF and the SuperCap feeds the DC-DC with the nominal current (25 mA), thus ensuring a small voltage drop. Actually, the ESD capability (2 F) allows supplying the sensor for about 20 s without being charged. The PV sensor is designed to harvest energy also at a low V_{panel} (down to 4.7 V, i.e., the breakdown voltage of the Zener diode D_{z3}). This threshold is lower than the subpanel V_{MPP} reduced by the forward voltage of the bypass diodes for most commercial PV panels. Moreover, in case of mismatch, the disconnection system keeps the panel first bypassed and then disconnected, thus not interrupting the power feeding of the sensor. The sensor turns off when the V_{panel} decreases without current mismatch, otherwise the panel will be bypassed so the disconnection section will force the panel in open circuit thus ensuring a rapidly charging of the SuperCap and regaining its normal operation.

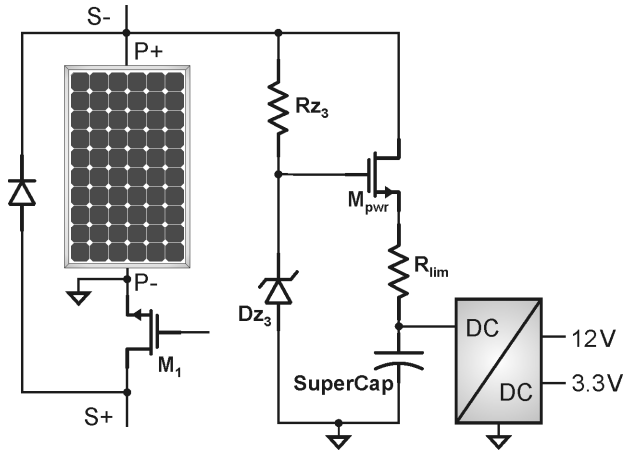

Fig 2.4 Schematic diagram of the power supply section.

The sensor provides a monitoring and diagnostic action by performing electrical measurements of the host panel. As in [1]-[3], [5] it measures the actual operating point, namely V_{panel} and I_{panel}, which depend on the inverter MPPT choice, and both V_{oc} and I_{sc}. While V_{panel} and I_{panel} provide only information about the actual produced PV power and allow achieving an accurate power mapping of the whole plant, they do not indicate the potentially producible power and the health status of the panel. A complete characterization can be accomplished only by adding the last two measurements. It is worth noting that, in normal operation, V_{oc} mainly depends on

temperature, while I_{sc} is proportional to the irradiance level [10]; in addition, their product is proportional to the potentially producible power [9]. Better results could be achieved by performing V_{oc} and I_{sc} measurements on each subpanel, thus providing a local irradiance and temperature maps at subpanel level, but this approach is not suitable for commercial panels since the electrical terminals of the subpanels are physically series connected, thus not allowing the sensor insertion.

Fig 2.5 depicts the measurement circuit composed by two sensing sections. The current sensing section, based on a shunt resistance, can be connected both in parallel to and in series with the panel. In particular, in disconnection mode (M_1 OFF), as M_{meas2} is activated, the current sensing section can measure I_{sc} due to the low value of the shunt resistance. Moreover, as M_{meas1} is kept ON and M_1 OFF, I_{string} flows through the current sensing section, which performs the I_{panel} measurement. The voltage sensing section is implemented by a resistive divider in parallel to the panel and is used to measure both V_{panel} (M_1 ON) and V_{oc} (M_1 OFF).

The measurement circuit works properly even in bypass conditions, and V_{oc} and I_{sc} can be monitored also if the panel is intentionally kept disconnected (on demand disconnection).

While V_{panel} is solely related to the panel behavior, the operating voltage drop V_{S-S+} offers information on how the system panel plus sensor is interacting with the rest of the string. In normal operation, V_{S-S+} is almost equal to the measured V_{panel} due to the negligible voltage drop across M_1; when the panel is under bypass conditions (M_1 OFF and $V_{panel}=V_{oc}$), V_{S-S+} is equal to the negative of the forward voltage of D.

The sensor is designed to perform V_{oc} and I_{sc} measurements in 3 ms, this feature is mandatory because during this period the panel needs to be disconnected from the string without generating an undesired disturb on the operating point of the whole string. Such short time is well below the inertia of the large input capacitance of the inverter so no perturbation affecting the inverter input; furthermore, only one panel at a time is disconnected.

The MCU section is composed by a Microchip PIC18LF4620. In order to minimize power consumption, the sleep mode of MCU is widely adopted. The MCU is awakened from sleep mode by the occurrence of two different kinds of interrupts: (i) watch dog interrupt, which periodically manages the bypass detection, and (ii) external interrupt, which is generated by the wireless transceiver as soon as a

message is received from the coodinator (see system configuration in the next paragraph). The message contains a measurement request and the desired disconnection status.

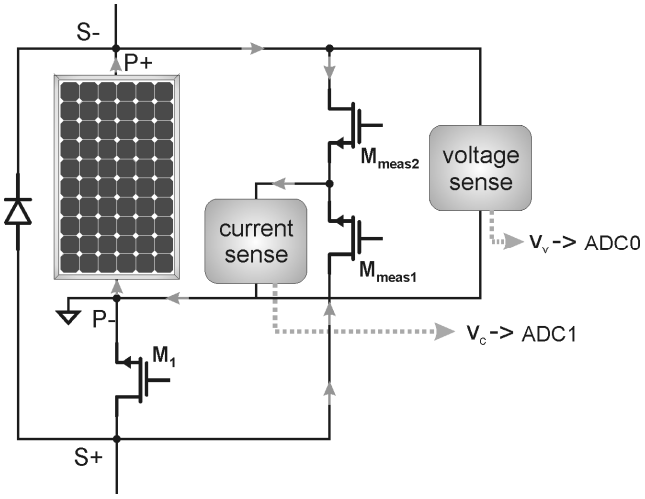

Fig 2.5 Simplified scheme of the measurement circuit.

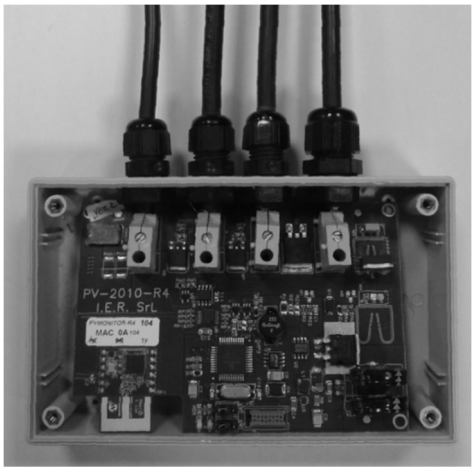

Fig 2.6 Prototype of the PV sensor equipped with the wireless communication interface.

The adopted sensor is 100 V/10 A rated, while the maximum voltage that can be safely applied to the panel terminals is 120 V (i.e., $V_{ds,max}$ of device M_1).

The wireless communication is based on Microchip MiWi (IEEE 802.15.4 compliant, 2.4 GHz frequency). Each PV sensor is equipped with a MRF24J40MA transceiver (up to 400 ft range, throughput of 250 kbps), which allows low power consumption (typically 19 mA in RX, 23 mA in TX, 2 μA in sleep). Each PV sensor of the network is univocally identified with its own address, thus the single malfunctioning panel is immediately detected also in large PV plants, thereby avoiding the need of in-situ inspections.

Fig 2.6 shows a prototype of the proposed PV sensor.

2.3 PLC on DC bus with PV modules series connected

The proposed sensor can be equipped with a Power Line Communication (PLC) interface instead of a wireless one [16], this option has great interest when large distance has to be covered, since the wireless approach entails a considerable rise in energy consumption.

The PLC is a wired protocol adopting as physical layer the power lines [17] and, in order to efficiently integrate monitoring systems into Smart Grids [18], a PLC is to be preferred [19]. The world widest PLC network was developed by the Italian electricity supplier company [20]. There are other examples at a smaller scale which perform PLC in domotic application through the home electricity grid. Above examples exploit AC power lines, but the idea can be easily extended with DC power bus. However in [21] a different solution was exploited in case of DC bus with DC/DC converters parallel connected, in that case the converter have switching frequency which can be modulated to induce electric perturbations on the power line which are recognized by a devised transceiver.

However, none of standard PLC equipments can perform a communication on a power bus with series-connected PV modules, since there are some issues to be faced with and a new PLC scheme is required. Fig 2.7a shows a standard PLC scheme, it consists of transmitting/receiving (TX/RX) transceivers parallel connected in the PL bus. Information data are transferred by TX to the bus in the form of high frequency signals which are superposed to the power signal;

this operation is accomplished by means of the high frequency (1:1) transformer. In the same way information signals are revealed by RX.

However, when the DC bus consists of series connected solar panels the scheme of Fig 2.7a does not work properly. In fact, from Fig 2.7b, where, instead of Fig 2.7a the power line was substituted by the solar string, some problems clearly appear.

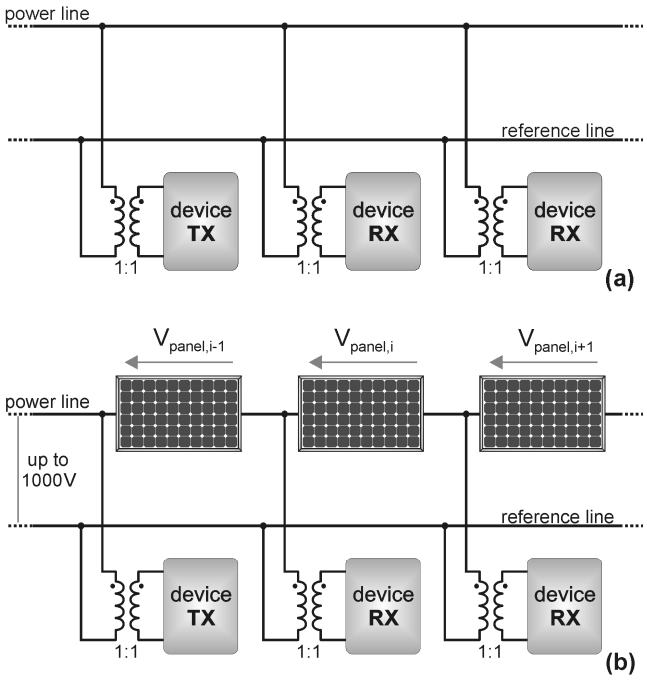

Fig 2.7 Schematic drawing of two PLC standard approaches: (a) parallel insertion on a standard physical bus, (b) parallel insertion on a bus consisting in a PV string.

First, each transceiver sees a different voltage along the power line, thus they should be either all oversized, in order to sustain the larger possible voltage appearing in the circuit, or singularly adjusted, in order to match each transceiver with the voltage corresponding to the particular position along the string; moreover, as the string can exhibit very high voltages, possible faults on the power line that could be reflected by the 1:1 transformer on the signal side would destroy the transceiver. Second, the high frequency signal should travel through each solar panel, but the solar panel is characterized by a strong reactive behavior, thus the signal would probably be lost;

furthermore the operating point of the solar panel could be affected by the voltage signal with a resulting degradation of the maximum power point tracking efficiency. Third, the reference cable is actually not available in a solar string, thus additional wiring should be provided.

All aforementioned issues can be solved if communication can be achieved on a single wire scheme. Fig 2.8 shows the innovative designed scheme. The main difference with respect to conventional PLC schemes is the presence of the inductor $L_{TX/RX}$. As the signal current flowing through the receivers is unique the voltage signal across $L_{TX/RX}$, imposed by the PLC transceiver, corresponds to an analogous perturbation of the voltage across the inductors $L_{TX/RX}$ of the receiving systems (RXs).

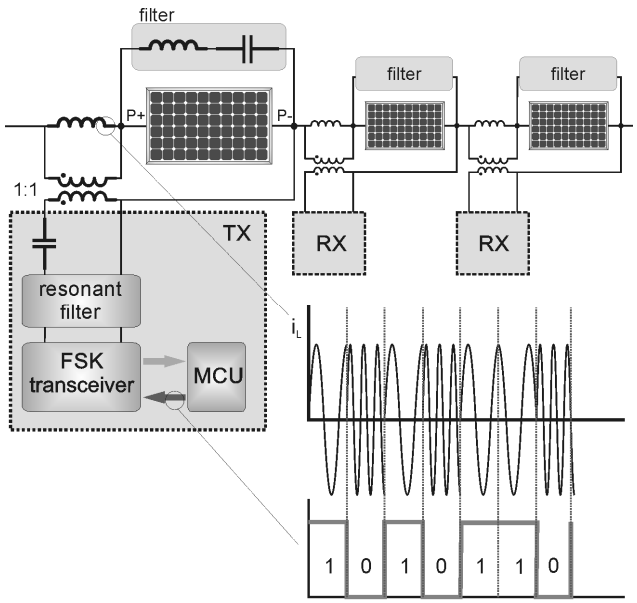

Fig 2.8 Schematic drawing of the proposed PLC approach.

In order to provide a low impedance path for the signal frequencies a LC series filter is parallel connected across each solar panel, so the information signal does not travel through the solar panels without affecting the operating point of the modules during transmission, thus avoiding degradation in MPPT. The LC impedance is chosen to act as a bypass path for the signal frequencies, while it does not affect at all the DC solar current.

The prototype adopts a commercial Frequency Shift Keying (FSK) transceiver ST7540 [22] to achieve a PLC at 132.5 kHz (i.e., European CENELEC standard C-band). The LC series filter across to each panel has the resonant frequency in the same band.

A further issue that should be considered depends on possible noises coming from the inverter input which produces voltage harmonics due to the switching operation. These frequencies could be interpreted as information data. For this reason a custom communication layer protocol was adopted in order to guarantee the rejection of false PLC messages. It adopts a "header recognition" function, which ensures the transfer of messages from the power line side to the microcontroller side only if a specific word of 16 bits is detected. The CENELEC standard C-band was chosen for the FSK modulator in order to satisfy the need to guarantee a proper spectral gap between signal frequencies and those coming from typical inverter switching frequencies. The transceiver is only devised to physical communication, while managing of the other communication layers is demanding to the MCU. In the receiving mode an input FSK signal coming from the power line is demodulated and the digital output is made available to the microcontroller. In the transmission mode the device modulates digital signals coming from the SPI in a FSK sinusoidal output.

A PLC interface prototype with a dedicated MCU is depicted in Fig 2.9. It is possible to recognize the PLC transceiver, the microcontroller, the toroidal inductor which acts as $L_{TX/RX}$ and the L-C series resonant filter.

The PLC interface continues to be supplied by the PV sensor harvesting stage, which must correctly supply the whole circuit.

The reliability of data communication was tested with reference to a string composed of 10 panels, each of which equipped with a prototype board. The structure of the PL messages is shown in Fig 2.10. It is worth noting that a "header startup" is included, which assures that all transients occurring when the transceiver starts to communicate are finished and from the communication view point it represents dummy bytes. The PL transceiver amplifier delay is shown in Fig 2.11. The time length of the dummy bytes is about 5 ms so that the signal has enough time to stabilize. The robustness of the communication was further improved by adding a "PLC Driver Header", which ensures the transfer of incoming messages to the PIC side only if a specific word of 16 bits is detected.

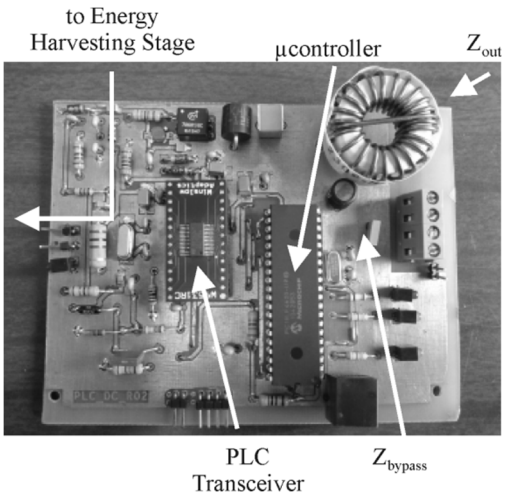

Fig 2.9 Picture of the fabricated prototype.

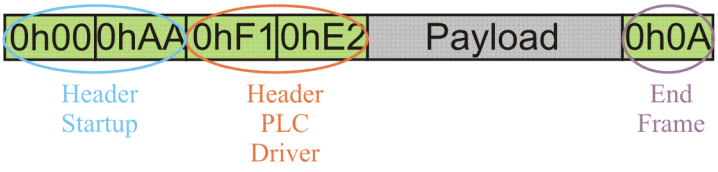

Fig 2.10 Structure of the PLC frame at data-link layer of the communication stack.

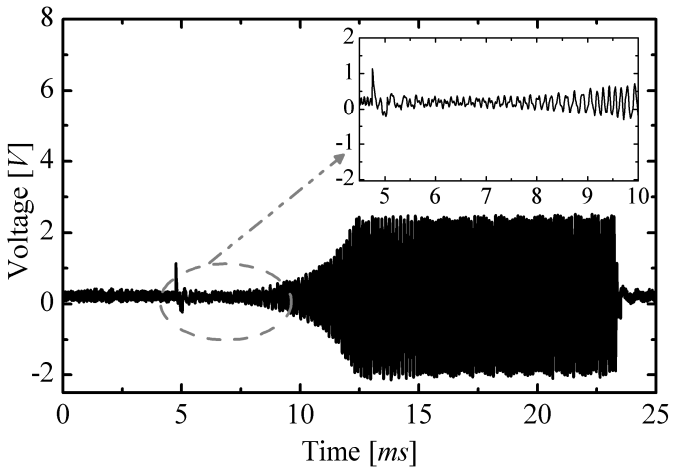

Fig 2.11 Experimental PLC signal at the output of transceiver, the waveform is highlighted during the internal PL amplifier start-up.

This is a solution adopted to overcome the noise introduced by the inverter and to avoid that the MCU continuously manages the reading of false messages. Fig 2.12 shows the transmission of the PLC Driver Header bits generated by the microcontroller and the corresponding FSK (bit 1 and bit 0 are associated to a low frequency sinusoidal signal and a high frequency sinusoidal signal respectively) codified voltage across $L_{TX/RX}$; the insets of Fig 2.12 show two magnifications of the FSK signal corresponding to bit 1 and to bit 0, the frequencies are very close each other as they are 131.4 kHz and 133.7 kHz respectively.

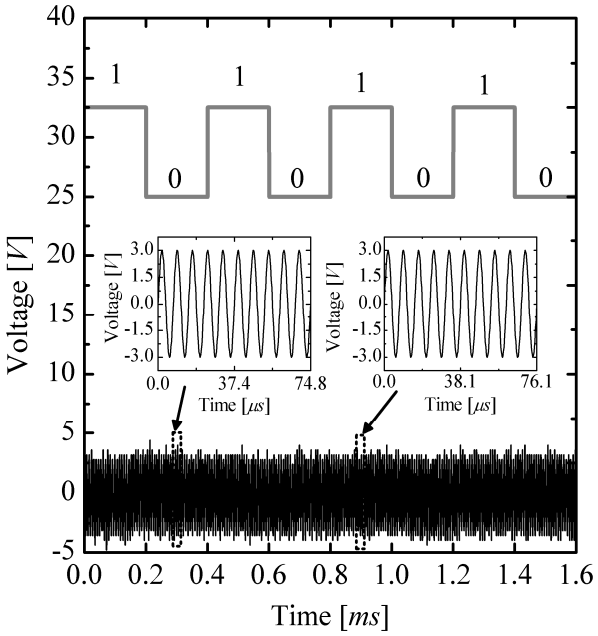

Fig 2.12 Binary sequence generated by the microcontroller and the corresponding FSK modulated voltage signal across $L_{TX/RX}$ of a receiver. In the insets two magnifications of the signal corresponding to bit 0 and bit 1.

Fig 2.13 shows the voltage signal across the $L_{TX/RX}$ inductor of the transmitting board of the whole message, as can be seen the spectral content of this signal is centred at 132.5 kHz, and it spreads over the whole CENELEC C-band since the sent message contains both low and high digital levels.

Fig 2.14 shows the signal across an $L_{TX/RX}$ inductor of a receiver board. The figure reveals that the voltage amplitude exhibits a

strong attenuation; however, the spectral analysis evidences that the information content was preserved.

The voltage drop across the solar panels (Fig 2.15) and the voltage at the input of the inverter (Fig 2.16) were measured and analyzed in the frequency domain.

The comparison between Fig 2.15a (signal travelling through the bus) and Fig 2.15b (no signals on the bus) along with the spectral analysis assesses that the presence of the PL signal does not affect the static voltage. The static voltage at the input of the inverter is reported in Fig 2.16a (presence of signal) and Fig 2.16b (no signal).

In the design of the communication scheme it should be considered that all inductors $L_{TX/RX}$ can be viewed as connected in a closed loop in the equivalent circuit at the PLC carrier frequency.

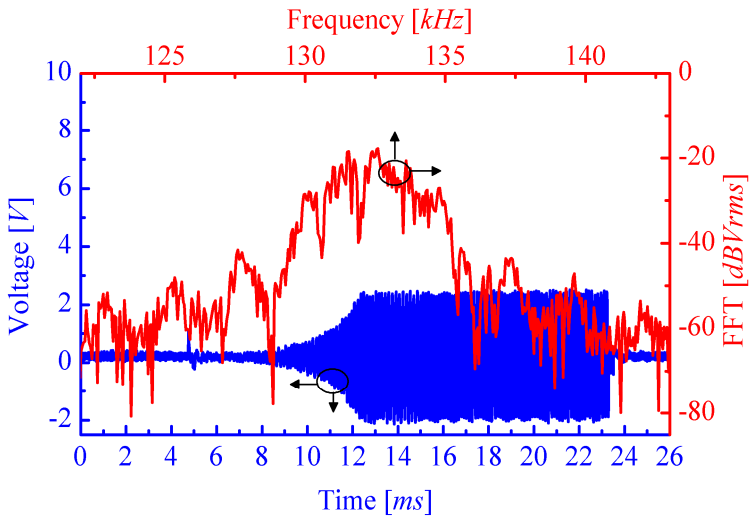

Fig 2.13 Voltage drop magnitude (blue curve) and corresponding FFT (red curve) at the transceiver output of the TX board.

The input terminals of the inverter where the string is connected are, indeed, "short circuited" for the signal frequencies by means of an LC filter, analogously to what happens for the solar panels.

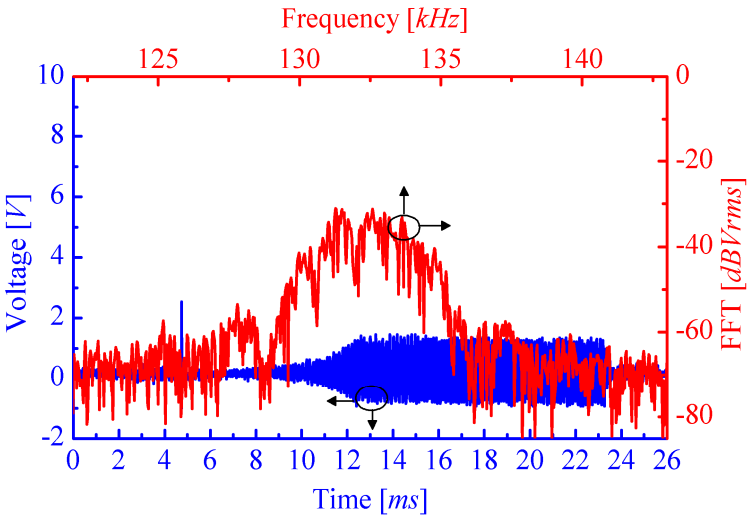

Fig 2.14 Voltage drop magnitude (blue curve) and corresponding FFT (red curve) at the transceiver input of the RX board.

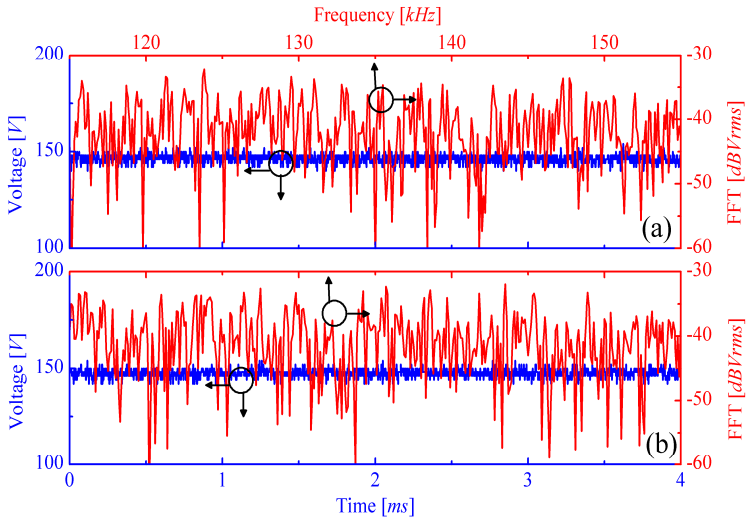

Fig 2.15 Voltage drop magnitudes (blue curves) and corresponding FFTs (red curves) across 8 panels between the transmitting and the receiving board for the case of transmission of message (a) and no message (b).

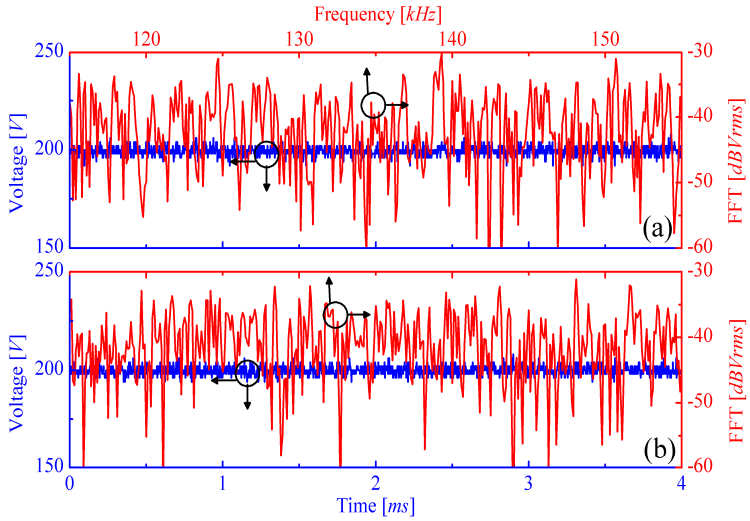

Fig 2.16 Voltage drop magnitudes (blue curves) and corresponding FFTs (red curves) at inverter input for the case of transmission of a message (a) and no message (b).

This precaution prevents communication signals from affecting the inverter behavior and confines those signals to the string side. Hence, the series of the RX inductances behaves as parallel connected to the TX inductance and the voltage perturbation imposed by the TX across its output inductor is shared among the input inductances of the RXs. In order to correctly decode a message, the amplitude of the voltage at the input of each RX should be inside the detection input range of the transceiver, which, for the ST7540, is in the range of 250 μVrms. According to the closed loop connection the sum of all voltages is zero, thus the amplitude of the signal V_{rx} manifesting at the input terminals of all RX blocks, when a signal with an amplitude V_{tx} is transmitted by a TX, is simply described by the following equation:

$$V_{rx} = \frac{V_{tx}}{N-1} \quad (2.1)$$

where N is the total number of transceivers connected to the power line; hence the amplitude of the transmitted signal (2 Vrms for the proposed prototype) should be accordingly adjusted.

2.4 System Configurations

The PV sensors can be adopted in different configurations along with one of the two communication interfaces, previous illustrated, in order to provide an effective monitoring and diagnostic system capable to give real-time alarms and accurate fault localization as first requirement, along with the capability to quantify actual potentiality of each section of the PV field as well. The original proposed approach is illustratively sketched in Fig 2.17 with reference to a single PV string composed by the series of N panels. In this case, all panels are equipped with a wireless sensor.

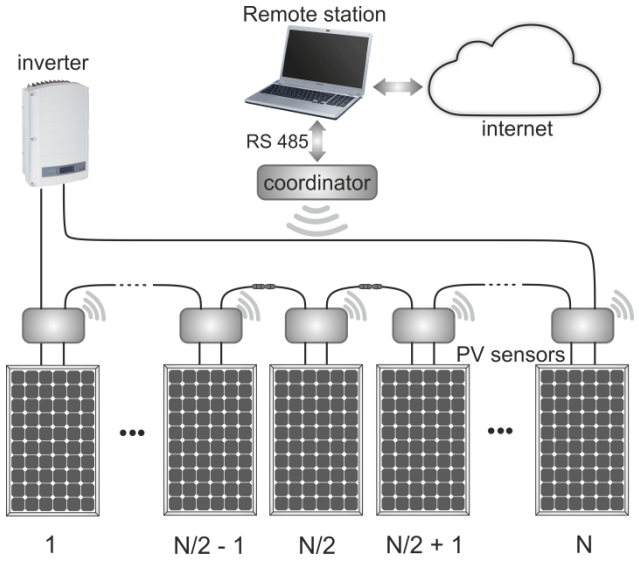

Fig 2.17 Block diagram illustrating the wireless approach applied to a PV string.

A coordinator unit manages the network by periodically sending to the sensors both measurement requests and desired disconnection status. The sensors allow data collection with arbitrary time scheduling, down to one second and less between each measurement. The network can be equipped by more coodinators each of them manages different section of the PV field and transfers data to a remote station via serial bus RS-485 through a MODBUS protocol. The remote station stores and analyses the data, moreover it makes data available on the internet by means of a web-based user interface. It must be remarked that one coordinator unit can handle up to 256

sensors. Moreover, the maximum number of coordinator units on the same serial bus is 256, while the length of the serial cable is up to 1000 meters.

Fig 2.18 shows how PV sensors are mounted behind each PV modules.

Obviously, when the distance to be covered are greater or in some special case (for instance fire protection as illustrated in the next paragraphs) where a wired communication is preferred, the PLC interface can substitute the wireless one as shown in Fig 2.19.

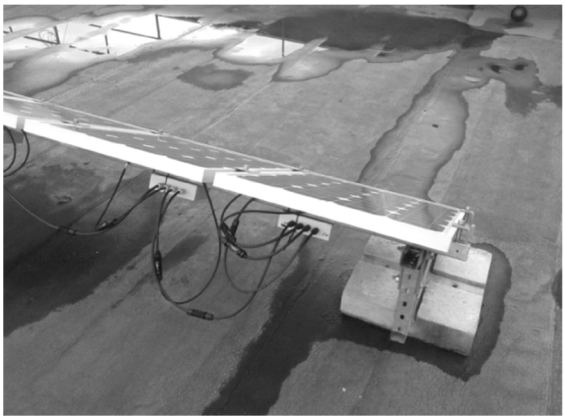

Fig 2.18 Picture of mounted PV sensors behind PV modules.

Depending on PV plant dimension, to adopt a monitoring system at this high granularity level could imply too high costs in case of large PV field, nevertheless systems operating only at inverter level cannot detect all fault condition occurrences moreover these systems cannot give information neither about which kind of fault occurred neither where it is localized. In order to provide a more flexible match between costs and sufficient granularity level when large plants are involved, another configuration of the proposed PV sensor can be adopted as illustrated in Fig 2.20 [9].

In this last configuration each string is equipped with two PV sensors named "string monitor" and "panel monitor". The "panel monitor" is the same PV sensor previous proposed and performs the measurement of the four fundamental parameters (I_{sc}, V_{oc}, I, V) of the host solar panel, it is mounted in the middle of the string but it is possible to eliminate it or to add more "panel monitor" in a single

string in order to gain additional information about the operation of the string.

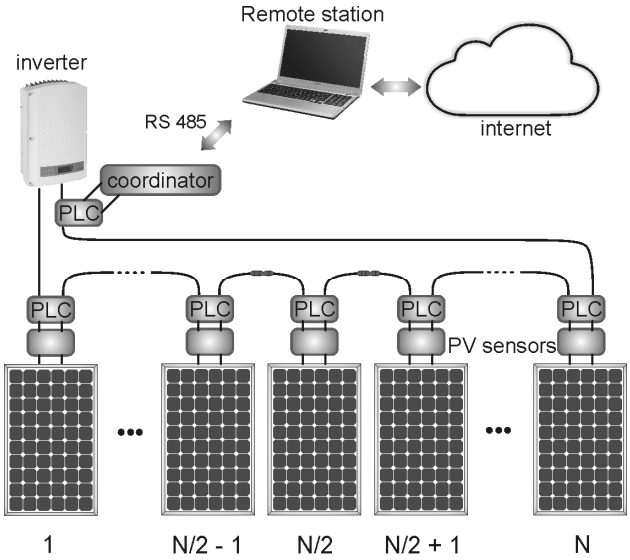

Fig 2.19 Block diagram illustrating the PLC approach applied to a PV string.

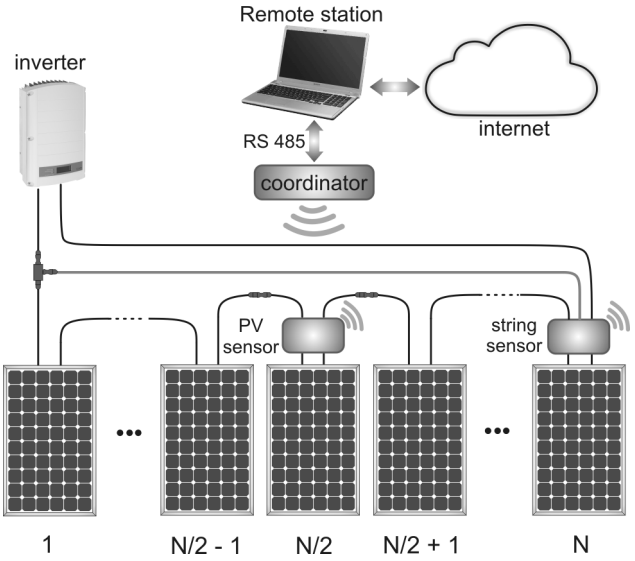

Fig 2.20 Block diagram illustrating the wireless approach applied to a PV string of a very large plant.

It is worth recalling that the panel monitor measurements give the power produced by the solar module, but are strongly affected by other modules connected in the string, because the current flowing through the string is unique. On the contrary I_{sc} and V_{oc} are reliable parameters for assessing module "health". The string monitor is mounted on the last solar panel of the string. It adds to the functionalities of the "panel monitor", the measurement of both string current and string voltage, in this case a new wire is needed for string voltage measurement but this cable is downsized because no power current flows through it.

2.5 Experimental results

The effectiveness of the proposed monitoring strategy was assessed by a wide experimental campaign. The analysis was conducted on different plants adopting the different aforementioned configurations. The first one (Fig 2.17) was tested on a roof-top plant of 4 kWp composed by two PV strings. The first experiment analyzed the effect of small-sized architectural shading which is commonly believed to entail a negligible degradation in the yield of domestic roof plants, since the energy loss is commonly, yet erroneously, associated to the shaded area. Fig 2.21 shows the behavior of I_{sc} and the operating voltage corresponding to the panels affected by the small shadow (i.e., #6 and #7) during a whole day. The other panels, including panel #4, belonging to the same string, are not affected by the shadow, thus exhibiting an even behavior in terms of I_{sc} and operating voltage.

The string current I_{string} is unique and equals to the I_{panel} of each module no bypassed (Fig 2.21a). An I_{sc} drop affecting panel #7 is observed from 3:00 PM until evening, which proves that all its subpanels are shaded; it is indeed well known that a partial shading event does not degrade the short-circuit current of a panel until all subpanels are obscured. Fig 2.21b provides additional information: the operating voltage corresponding to panel #7 exhibits the typical ladder shape due to the gradual bypass of the subpanels; the shadow falls on the panel at about 1:00 PM sequentially involving the three subpanels, while V_{S-S+} drops by about 1/3 of the nominal V_{oc} as each subpanel is bypassed. It is worth noting that a marked temporary perturbation in the operating behavior of the string appears when the first subpanel of

panel #7 is forced in bypass conditions. In this case, the string operating current dramatically decreases, while the string operating voltage slightly increases, thus resulting in a large power loss.

A further inspection of Fig 2.21b reveals that the shadow propagates over the string by gradually affecting also panel #6. More in general, from a diagnostic viewpoint, the propagation of bypass events over the string that seems to be consistent with the trajectory of the Sun, must be ascribed to architectural shading. This conjecture can be confirmed by comparing the data collected in several days in order to verify that the bypass events repeatedly take place in the same time window.

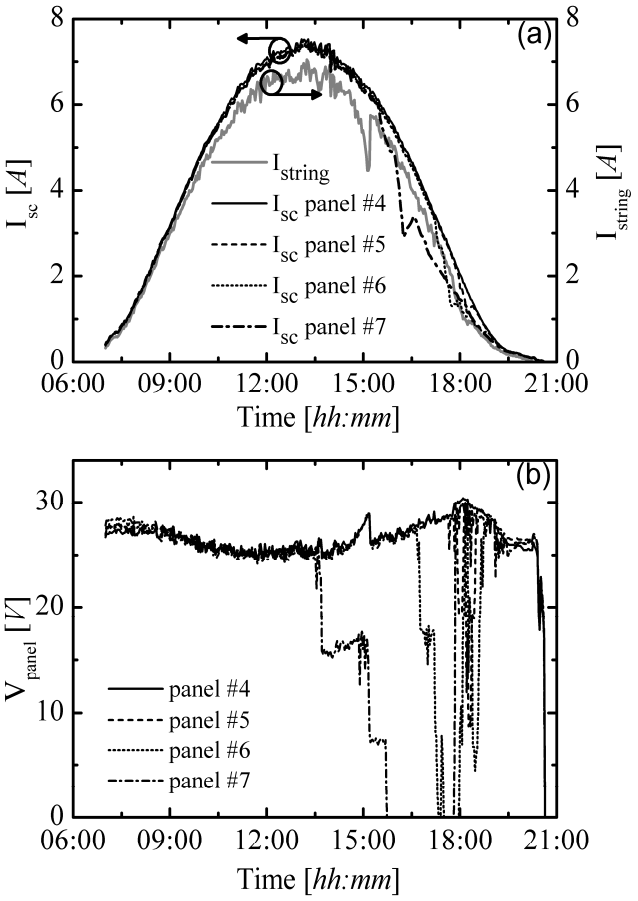

Fig 2.21 Experimental (a) short-circuit currents I_{sc} and (b) operating voltages against time for some panels of the same string. In (a), the string current I_{string} is also depicted.

The second experiment was conducted on the second string in order to investigate the effect of a single malfunctioning panel. Fig 2.22 depicts I_{sc} and the operating voltage monitored during a whole day, referring to panel #1 and panel #2; I_{sc} of panel #1 is constantly lower with respect to others (including panel #2) as shown in Fig 2.22a, this can be reasonably attributed to the presence of dirt on its surface. As a result, the string current coincides with the operating current I_{panel} of panel #2.

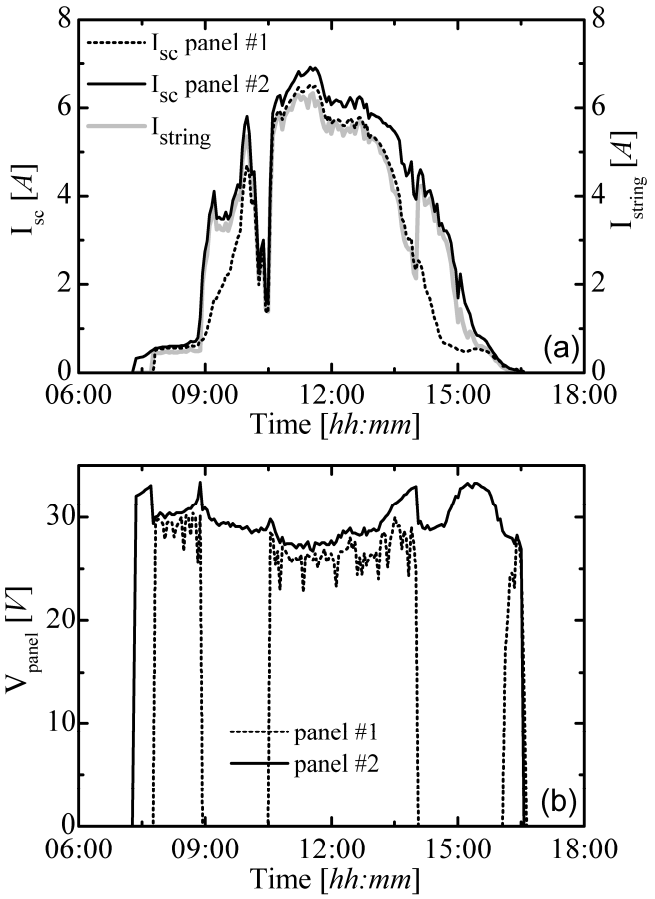

Fig 2.22 Experimental (a) short-circuit currents I_{sc} and (b) operating voltages $V_{S\text{-}S+}$ against time for panels #1, and #2 belonging to the same string. In (a), the string current I_{string} is also shown.

Fig 2.22b shows the occurrence of two bypass events affecting panel #1 between 9:00 AM and 10:30 AM and between 2:00 PM and

3:30 PM, respectively. In this case, I_{string} is close to I_{sc} of panel #2, thus proving that the string reaches the global MPP. Conversely, around noon, panel #1 is still active, thus limiting the string current and causing a significant power loss. It is interesting to note that I_{string} regains the expected value as panel #1 falls bypassed.

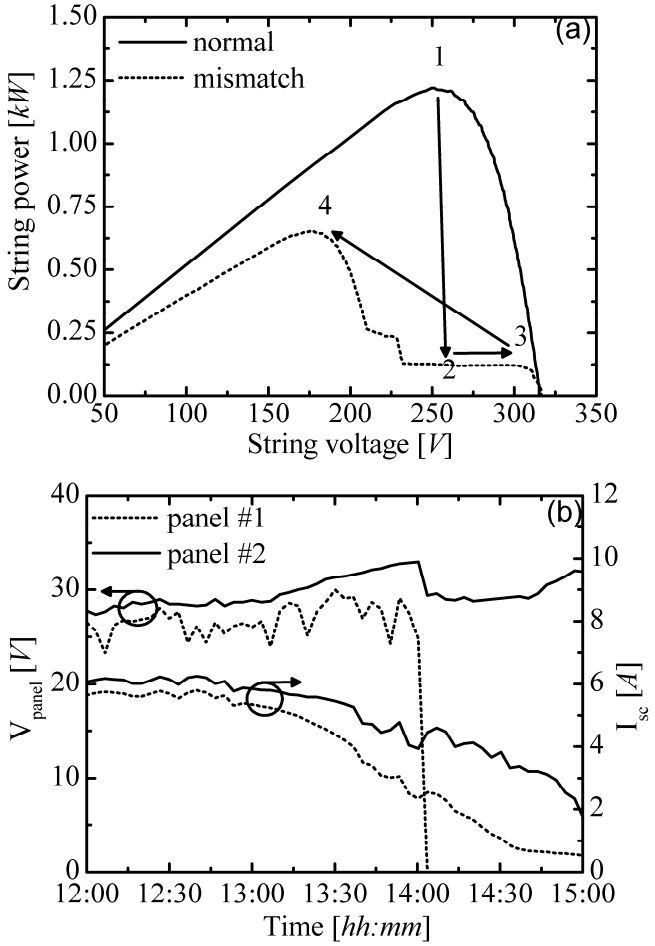

Fig 2.23 Effect of mismatch event: (a) typical step sequence performed by the MPPT algorithm; (b) evolution of V_{S-S+} and I_{sc} of selected panels. Fig 2.23b is the magnification of Fig 2.22 over the time interval between 12:00 PM and 3:00 PM.

Fig 2.23a shows the typical step sequence followed by the MPPT algorithm which causes the limiting action observed through

the monitoring data, namely the increase in operating voltage and the decrease in operating current due to a malfunctioning panel.

The MPPT sequence is this: at the beginning, the string is completely sunny (1); then the producible power gradually decreases due to a mismatch effect (2); subsequently, the MPPT algorithm forces an increase in V_{panel} by assuming a uniform condition and, undesirably, tracks a local maximum instead of the absolute one located at a lower voltage (3); finally, the MPPT algorithm (likely after a complete scanning of the power-voltage curve) drives the operating point to the absolute maximum by reducing the voltage (4).

This allows explaining the behaviour of the operating voltages depicted in Fig 2.23b: panel #1 limits the string current (2) due to its poor I_{sc} with respect to the rest of the string. First, the inverter pushes other panels to work far from their MPP by increasing V_{panel} and consequently reducing I_{panel} (3). Eventually, the MPPT action keeps panel #1 bypassed at about 2:00 PM, thus making the other panels of the string regain their normal behavior (4).

The above results evidence that the monitoring approach based on the proposed sensors reliably reveals temporary MPPT failures, which represent a significant part of the yield degradation under mismatch conditions.

The PV sensor mounted in the configuration shown in Fig 2.20 was exploited to investigate the performances of a 83 kWp PV plant installed on the rooftop of a car retailer in the south of Italy. Fig 2.24 shows the layout of the system.

The system exploits three 30kW double input inverters with a dedicated MPP tracker for each input, thus the plant, composed by 18 strings of 18 panels each, is divided into subfields each of which composed by three parallel connected strings. In Fig 2.24 there are different colors indicating the subfields.

The PV plant under test is new and well performing, anyway the high accuracy of the monitoring system has identified those subfields which could perform better than nowadays.

Fig 2.25 shows the operating voltage profiles supplied by string #1 during two different days.

The figure shows that the "malfunctioning" event is confined at a given time and it is repetitive, thus it is generated by some architectural shadowing. This assumption is enforced by the particular shape of the voltage recovery, which occurs by means of discrete steps

corresponding to the turning off of the bypass diodes when the shadow moves away.

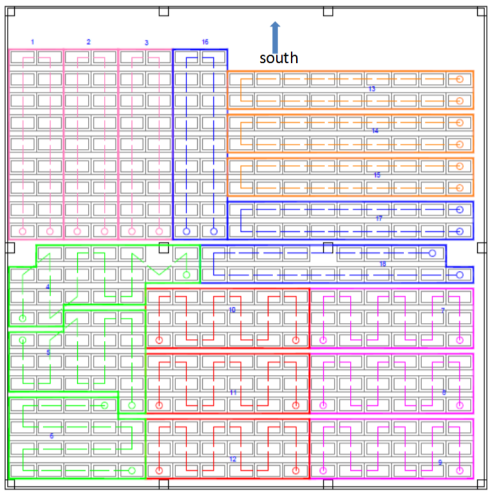

Fig 2.24 PV plant layout. The system employs three double MPP tracker inverters, each of which connected to a parallel of the 3 strings.

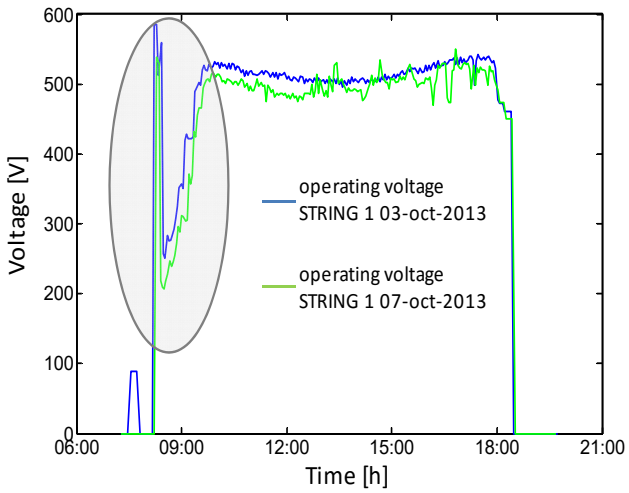

Fig 2.25 The behavior of string operating voltage of the string #1 in two different days. Around 9 AM, a bypass event affects several modules.

Fig 2.26 shows the current supplied in a same day by string #1, string #2 and string #3, which belong to the same subfield thus they are connected in parallel to the same inverter input.

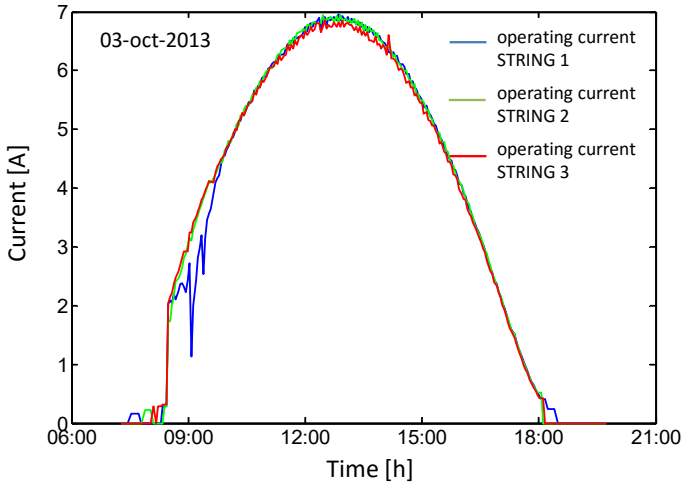

Fig 2.26 Comparison of the operating current referring to three PV strings in parallel belonging to the same subfield.

The figure reveals that only string #1 is affected by a shadow. Moreover, it is likely that the shading effect is amplified by the inverter MPPT. In case of mismatch the shaded string shows indeed a maximum power point voltage lower than the sunny ones, when the inverter forces the parallel to work in the global MPP the shaded string is affected by an additional current drop. The monitoring of the performances of single solar panels allows full understanding of string operation. In Fig 2.27, the operating current of string #1 is compared with the short circuit current of two monitored panels, namely module #1 and module #9 of the same string. Early in the morning, the short circuit current referring to module #9 drops down with respect to the string current, thus evidencing that the module is in a bypass condition, while the string current is substantially unaffected, thanks to the activation of the corresponding bypass diodes.

Fig 2.28 shows the analysis of the operating voltage of the two modules monitored in string #1. The sudden voltage drop, to about 1/3 of the operating voltage, proves that in module #9 two submodules are bypassed. Subsequently the inverter tracks a local maximum at higher voltage, causing an increase of the actual voltage of sunny panels as it

can be seen for module #1 (same effect previous described through Fig 2.23a).

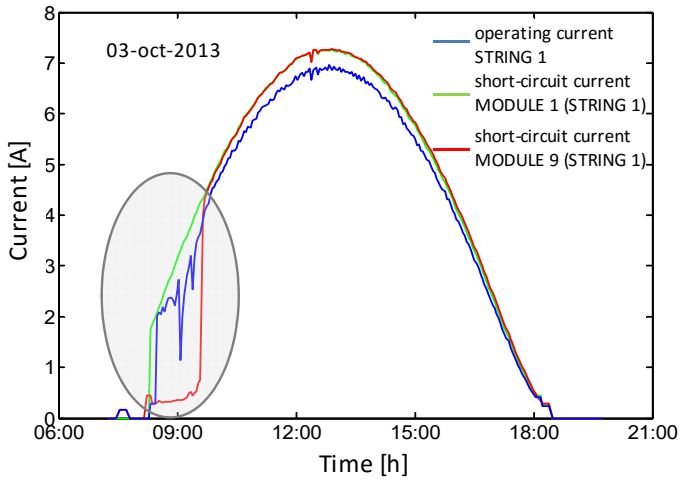

Fig 2.27 String #1 operating current is compared to the short circuit currents of the two modules in the same string.

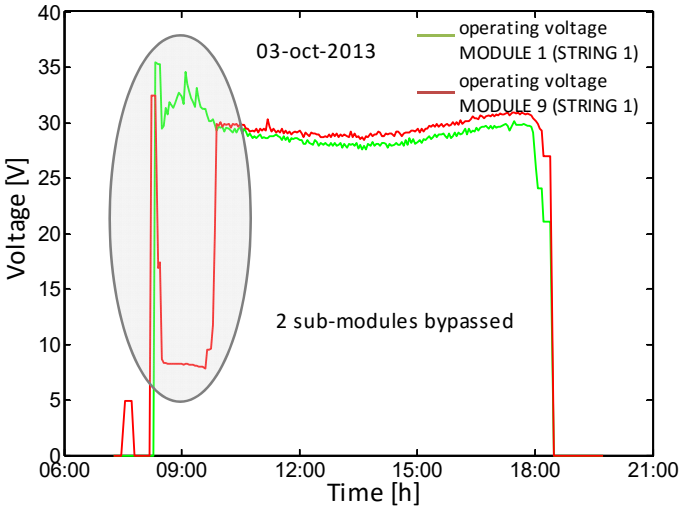

Fig 2.28 Comparison of the operating voltages corresponding to both module #1 and module #9. A bypass event occurs for module #9 around 9 AM.

A main challenge for both proposed configurations is the management of the large amount of collected data. The measures

along a whole day can give a lot of information to a highly skilled engineer. However an effective diagnostic system should be capable to automatically analyze collected data. This task can only be accomplished by defining proper rules allowing unambiguous events recognition. The first issue to face with is the need to find an automatic algorithm capable to distinguish between losses due to atmospheric irradiance changes and losses due to "malfunctioning" like those previous investigated.

The rules implemented are based on the isochronal comparison among events recognized as loss in the PV energy yield. Each loss event is characterized by a start time and a stop time. If losses event occur in different day and they are time correlated, they are recognized as "malfunctioning" event. When the system is configured as in Fig 2.17 and Fig 2.19 it is possible also to spatially correlate loss events associated to individual panel in order to provide one single event which collects the "malfunctioning" events occur in a particular location of the PV plant caused by the same reason. An estimation of the losses is extremely useful since the PV plant owner can schedule an intervention of maintenance only if the loss heavily affects the energy yield. An automatic tool was developed which reads the database of the measurements and creates another database where all detected loss events are collected. The block diagram of the software is shown in Fig 2.29. In the second database, created by the tool, all the malfunctioning events are stored in a table, then post processing routines analyze the records of this table in order to spatial correlate events associated to a same problem. Thus a second table is created where each record collects different records of the first table. Finally events associated to different days recorded in the second table are gathered together in one single record of a third table, if they are time correlated. The information provided by the second table can be synthesized in a graph as in Fig 2.30. These two bypass events are strictly time correlated so they are recognized as a single event in the last table. This tool can provide both run time information about the losses and post processing of daily collected data.

As an example of post processing of the monitoring data, collected on the PV plant equipped with the PV sensor configuration of Fig 2.20 and with the layout of Fig 2.24, is the energy loss map shown in Fig 2.31.

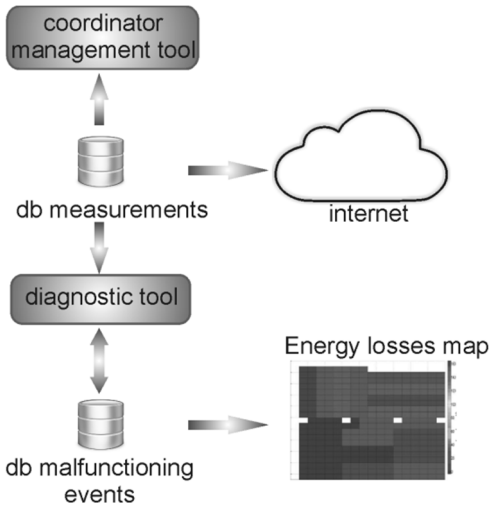

Fig 2.29 Block diagram of the proposed automated monitoring and diagnostic tool.

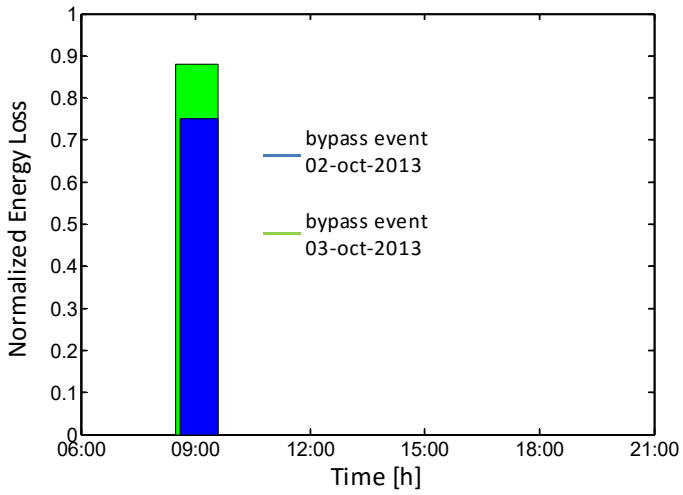

Fig 2.30 Example of bypass events of different modules in string #1 recognized as a unique loss event.

Comparing the PV plant layout and the loss map, it is evident that the string #1 exhibits a strong reduction in energy yield, this loss was caused by the bypass events occurred around 9 AM everyday and previous illustrated in Fig 2.25.

The subsequent analysis "on the field" evidenced the presence, on the east side, of some trees whose effect was previously

underestimated. It is worth noticing that the analysis was only performed on the basis of measurement data which were automatically elaborated without direct inspection on the site. The feedback was automatically generated and passed to the customer.

The creation of an energy loss map of the PV field is not the only way to exploit the information gained by this high granularity monitoring system, in the following paragraphs two other examples of applicability will be illustrated, both imply automatic operations performed or on the conversion system or in the PV plant configuration.

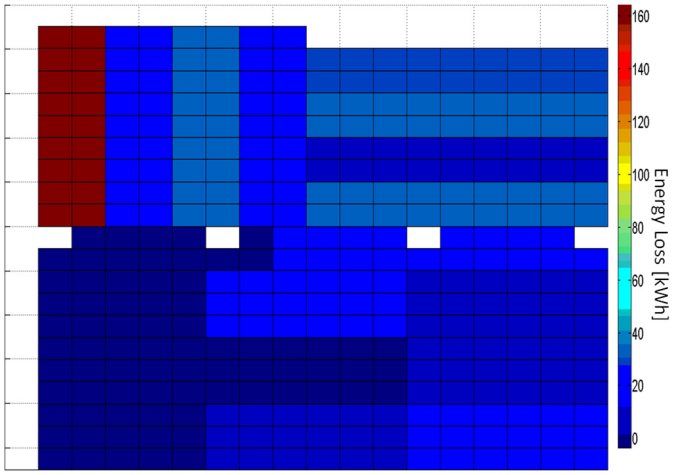

Fig 2.31 Detailed map of overall energy losses along an observation period of about two months.

2.6 Information based maximum power point tracking (iMPPT)

The information gained by the PV sensors can be adopted to improve the MPPT because it can avoid losses for two reasons: (i) the information can increase the convergence speed to the MPP, (ii) the information can avoid that the MPPT fixes as operating point a local maximum instead of the global one. Tracking procedures start with the measurement of the open circuit voltage of the PV system and assumes that the voltage corresponding to the maximum power lies at about 90% of the V_{oc} (constant fractional approach) [23]. This

assumption is quite well verified when solar panels are uniformly illuminated. Instead no rules can be given about V_{MPP} in mismatch conditions and the tracking algorithm, which continues to suppose uniform illumination, might fail. This paragraph deals with the behavior of a tracking algorithm ([24], [25]) able to univocally drive the operating point of the photovoltaic system toward the absolute maximum of the P-V curve, independently of how many local maxima the curve exhibits. Hereafter this algorithm is denoted as information based MPPT (iMPPT) since the whole procedure is based on real-time measurements of I_{sc} and V_{oc} for each solar panel. These two parameters provide direct information about the irradiance (I_{sc}) and the module temperature.

The idea of the proposed MPPT algorithm assumes that it is possible to reconstruct an approximate version of the actual current-voltage (I-V) curve of a partially shaded string, formed by N series connected solar panels, taking into account the couple I_{sc} and V_{oc} for each panel. The algorithm estimates the voltage corresponding to the absolute maximum power point (V_{MPP}) and set this value as starting point for a standard Perturb & Observe (P&O) tracking procedure [26]-[29]. Reconstruction of the string I-V curve is performed by superposing a simplified form of the single panel I-V curves which are approximated by trapezoidal shapes. Namely, once both V_{oc} and I_{sc} of a given panel are known, the coordinates of the maximum power point are calculated according to the following relations:

$$\begin{aligned} V_{MPP} &= k_V \cdot V_{oc} \\ I_{MPP} &= k_I \cdot I_{sc} \end{aligned} \quad (2.2)$$

where the coefficients k_V and k_I are taken from panel datasheets and then they are corrected in temperature according to [25]. The trapezoidal I-V curve of the solar panel is drawn as shown in Fig 2.32, where the actual I-V curve is also reported for comparison.

Fig 2.33 shows an example of string characteristic reconstruction. In particular Fig 2.33a shows the "actual" I-V and P-V curves evaluated by means of standard circuit simulations assuming a one diode model for the solar panel and a PV string made by three PV modules with three different irradiance values. Fig 2.33b reports the corresponding approximated curves, as can be seen all voltages corresponding to the maxima are almost coincident for the two cases.

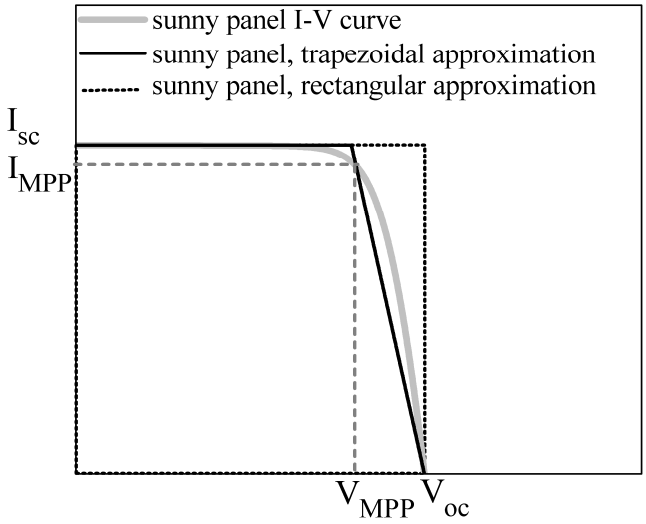

Fig 2.32 Trapezoidal approximation employed in the iMPPT.

Experiments were conducted on the string of Fig 2.34 with the aim of experimentally verify the correct behavior of the whole system comparing the proposed algorithm with the operation of a commercial inverter. As can be seen semi-transparent dyed sheets were employed to induce an uneven illumination frame.

Two cases were considered. In the first the string was kept under uniform illumination. The resulting measured P-V curve is shown in Fig 2.35a. The operation of the standard MPPT (constant fractional + P&O) is monitored in Fig 2.35. The string voltage started at V_{oc} (225 V), subsequently it jumped to a guess value corresponding to 0.9 V_{oc} (i.e., 200 V) and then decreased according to a positive gradient mechanism until V_{MPP} was reached (180 V). The convergence was achieved in about 10 s (Fig 2.35b). After that the operating point showed a small oscillation around the MPP, as expected for P&O algorithms. Fig 2.36 shows the behavior of the proposed tracking algorithm on the same P-V curve. In this case the starting voltage guess value (i.e., about 180 V) was estimated from the knowledge of I_{sc} and V_{oc} and this value is very close to the V_{MPP}. As a consequence, the convergence time is reduced.

The performances of the two algorithms in uniform illumination are compared in Fig 2.37 were the output powers versus time are reported.

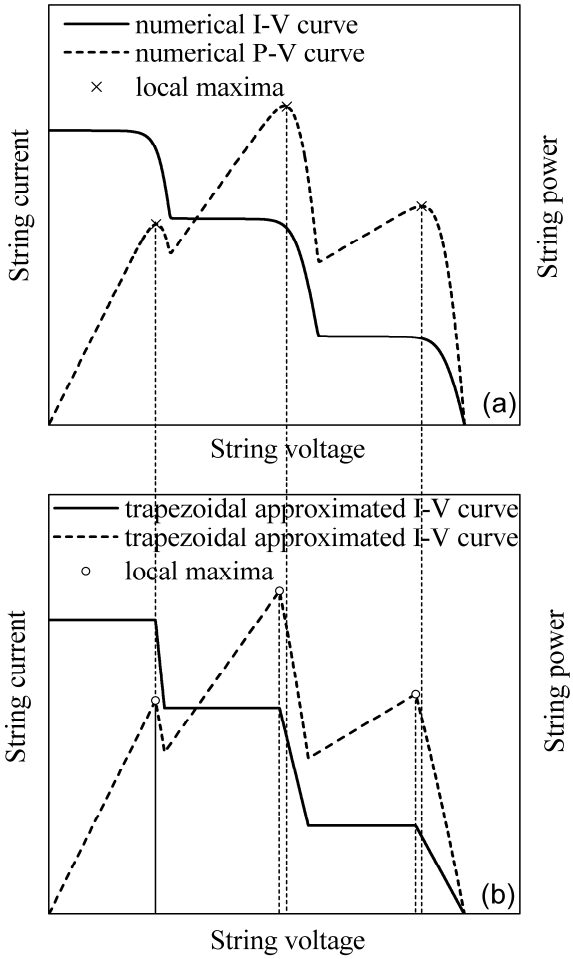

Fig 2.33 (a) Simulated I-V and P-V curve. (b) Trapezoidal approximation.

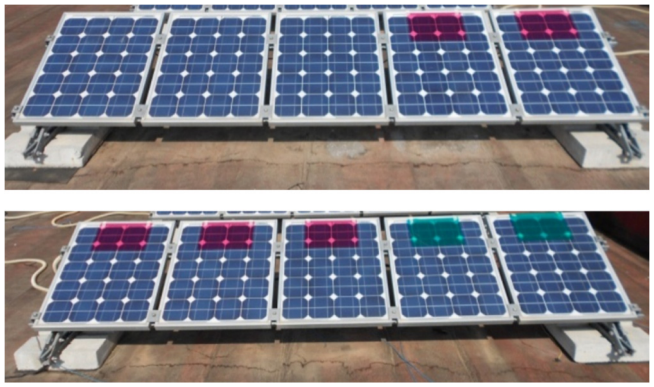

Fig 2.34 Ten panel PV string covered by optical plastic film.

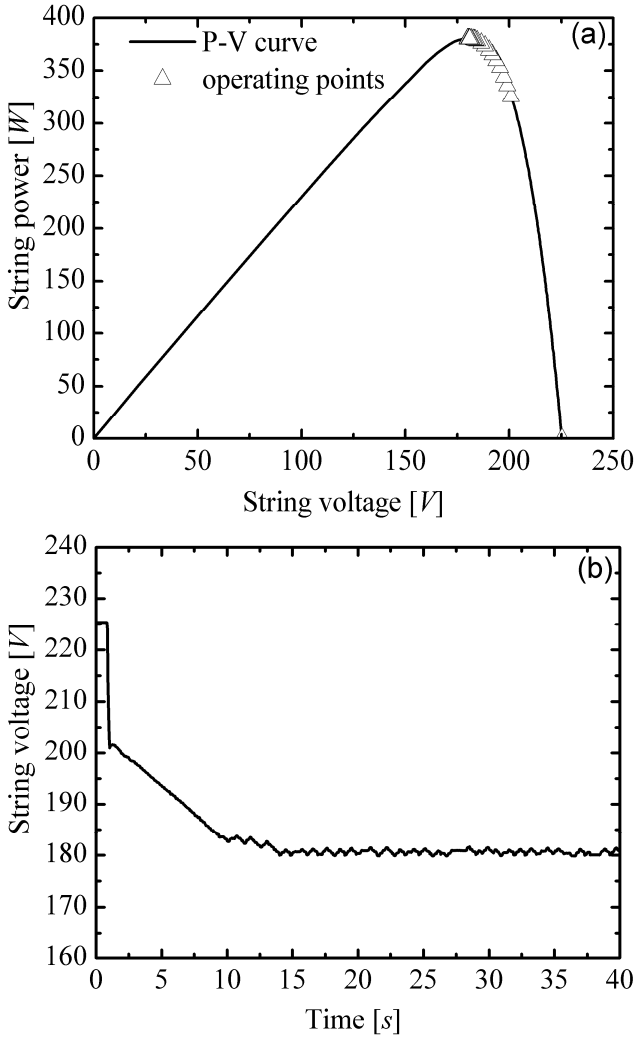

Fig 2.35 Sunny case. (a) Experimental power-voltage characteristic of the test string under full irradiation. The operating points of the string by adopting a classic P&O algorithm are shown. (b) String power against the time.

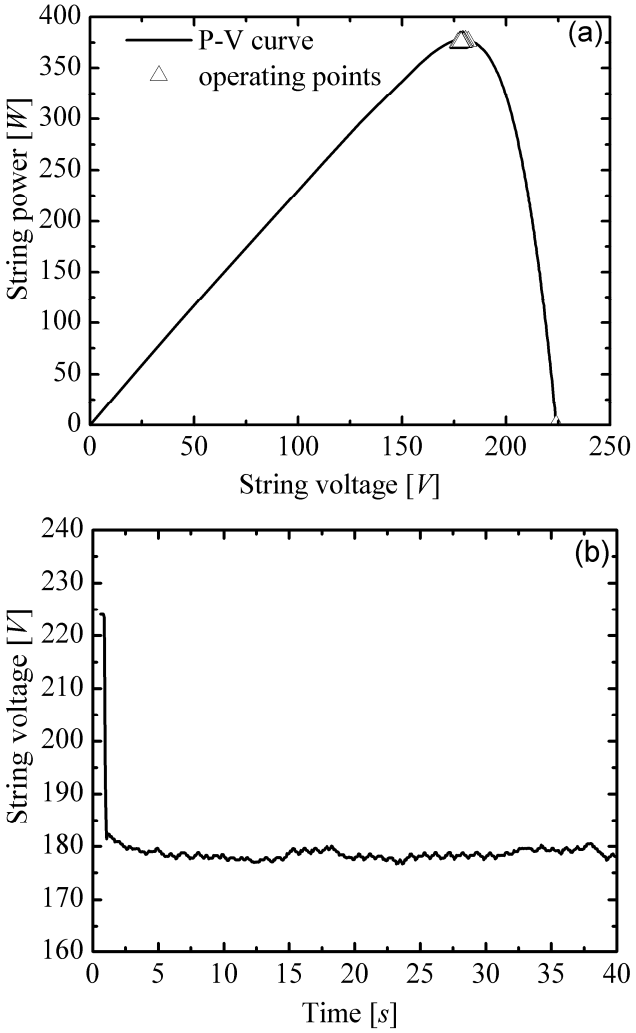

Fig 2.36 Sunny case. (a) Experimental power-voltage characteristic of the test string under full irradiation. The operating points of the string by adopting the iMPPT algorithm are shown. (b) String power against the time.

As can be inferred the proposed information based MPPT keeps the MPP faster. It required about two extra seconds to carry out the guest voltage estimation due to the measurement and data processing time. Nevertheless, the convergence was achieved in about 2.5 s.

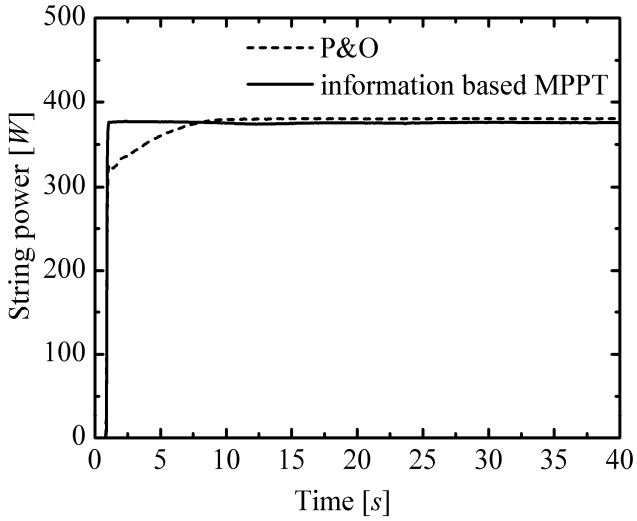

Fig 2.37 Comparison of string power behavior against the time corresponding to both P&O and iMPPT algorithms.

In the second case the illumination was not uniform, so as to have the P-V curve shown in Fig 2.38a. Also in this case the performances of the standard algorithm with respect to the proposed one are compared. Fig 2.38b shows the output voltage given by the standard one. Again, the algorithm starts from V_{oc} and tries, as starting guess point, 90% of that value; then the voltage is increased to stabilize at about 200 V. The convergence was achieved in 25 s. As expected, the guess voltage value provided by the standard MPPT algorithm is quite the same as the previous case, and the positive gradient mechanism makes the operating point converge to a local V_{MPP} located at the right side (high voltage) of the P-V curve.

Fig 2.39 shows the operation of the iMPPT. In this case the starting guess point is located very close to the global V_{MPP} as a consequence the convergence is immediately reached (5 s) by the system as shown in Fig 2.39b.

The iMPPT correctly recognizes the absolute maximum thus giving a power gain of about 75 W over the standard system.

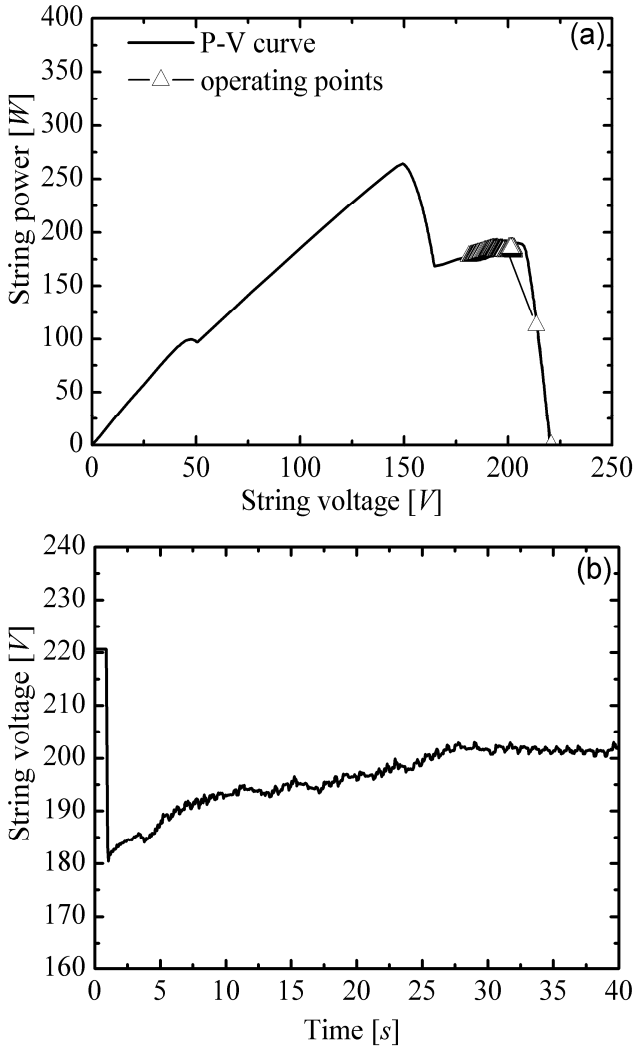

Fig 2.38 Partial-shading case. (a) Experimental power-voltage characteristic of the test string under partial-shading conditions. The operating points of the string by adopting a classical P&O algorithm are shown. (b) String power against the time.

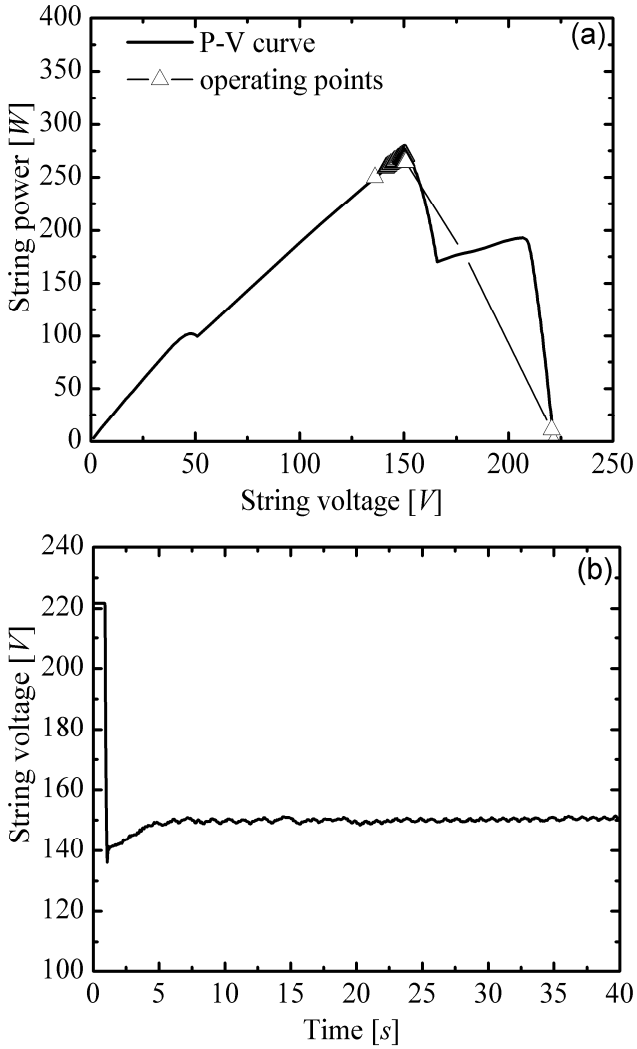

Fig 2.39 Partial-shading case. (a) Experimental power-voltage characteristic of the test string under partial-shading conditions. The operating points of the string by adopting the iMPPT algorithm are shown. (b) String power against the time.

Fig 2.40 reports the maximum producible string power corresponding to the hypothetical case where each panel would work individually (i.e., not limited by the other panels in the string) close to its MPP, along with the power produced in the case of an inverter adopting an iMPPT and the real power produced by the string under test. Under uniform irradiance and temperature conditions the three curves would coincide; in case of mismatch, the power loss due to the

mismatch is quantified by the gap between the maximum producible power and that estimated by the iMPPT algorithm, while the drop between the latter and the measured one represents the power loss caused by the MPPT failure.

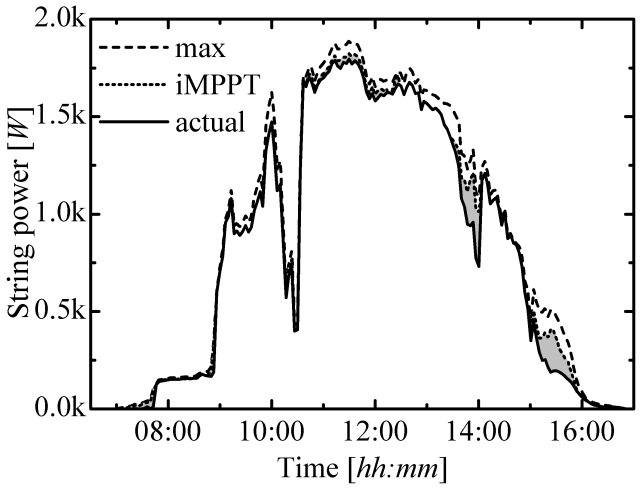

Fig 2.40 Experimental string power against time compared to maximum producible power and to MPP estimation obtained by means of the iMPPT algorithm. The grey area indicates the power loss due to the MPPT failures.

The iMPPT adopts the information gained by the PV sensors to perform active operation on the conversion system in order to improve the MPPT efficiency, nevertheless it can be employed at least to estimate the amount of energy loss when a standard inverter is adopted. Anyway also in the last case, an active action can be performed by the PV sensors network, since each board is equipped with a disconnection section which can force a PV module in bypass on demand. This on demand disconnection feature can be employed to mitigate the power degradation due to MPPT failures, in particular, the panels limiting the power production (i.e., the active panels exhibiting an I_{sc} lower than the estimated I_{MPP}) can be intentionally disconnected. As a result, the local maxima located at a voltage higher than V_{MPP} will be eliminated, thus helping the inverter to force the string close to the global MPP. Unfortunately, it is not possible to eliminate the local maxima located at a voltage lower than V_{MPP} without affecting the global maximum power. In the next paragraph

the potential dynamic reconfiguration feature of the PV sensors will be investigated.

2.7 Dynamic reconfiguration of PV plant

The reconfiguration approaches are based on the idea to rearrange the PV plant structure in order to ensure a regular shape of the PV characteristic with a single MPP; the aim is to avoid MPPT failures. The P-V curve exhibits multiple maxima in presence of mismatch conditions, in principle the P-V curve could be brought back to a single maximum by disconnecting limiting panels. In literature the reconfiguration methods, which have been presented so far, did not perform limiting panel disconnection; they consist of complex switch matrix allowing parallel and/or series connection of groups of series connected solar panels, eventually constituted by only one panel. The aim is to find the most productive configuration, however those works did not analyzed the topic in a complete way since they present only theoretical studies [30] or experiments limited to very small test plants and many practical problems are misrecognized. For instance in [31] the presence of the blocking diode in case of modules parallel connected was not taken into account along with the effect of increased ohmic losses coming from the strongly increased currents as well the cost of increased wire section.

In those systems the research of the optimum configuration required the knowledge of the spatial irradiation profile otherwise, in absence of this information in [32] it is proposed to check the power produced by all possible switch configurations before choosing the best one. Nothing is said neither about which kind of switch could be used nor about the time required to complete the sorting procedure.

Thanks to the iMPPT algorithm and to the PV sensor network, the proposed high granularity reconfiguration system [33] is able to (i) recognizes all cases where a single solar panel is limiting the power delivered by a solar plant, (ii) recognizes whether or not disconnection of the limiting panel can be beneficial (iMPPT) (iii) performs disconnection through the PV sensor disconnecting section.

In this application the disconnecting section is forced by the microcontroller to the state of open circuit when a wireless or power line command is sent. The decision of disconnecting a panel requires the knowledge of the effect on the global power producible by the

whole string and the PV sensor circuit allows this feature, thanks to its measurement section, which continues to provide measurements even if the panel is disconnected. After this real-time evaluation, an automated software can send a message to a specific board, requiring the bypass of specific panel.

The correct operation of the on demand disconnection is illustrated in Fig 2.41 which shows measurements performed on a solar panel, embedded in a ten solar modules string.

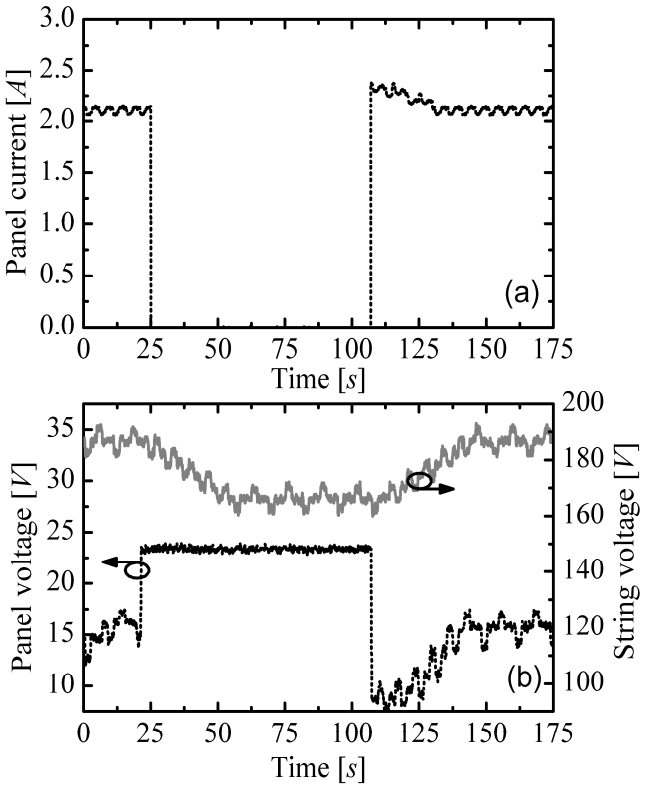

Fig 2.41 Host solar panel current (a), host solar panel voltage (b), string voltage (b) during a disconnection request.

The panel operating current is reported in Fig 2.41a. At t=25 s a disconnection request forces to zero the current flowing in the PV module. At t=100 s, the PV sensor receives a request of reconnection and the current recovers the normal operating value. Fig 2.41b shows the panel voltage and the overall string voltage. Before disconnection, the operating voltage is imposed by the inverter which tracks the MPP

of the string, the oscillations superposed to the string voltage are related to the MPPT. After disconnection (t=25 s) the solar panel is isolated from the string (oscillations of the voltage disappear) and its operating point is forced to the open circuit voltage. On the other hand the string voltage decreases by a corresponding amount, thus evidencing that disconnection of a single panel does not compromise the operation of the remaining string.

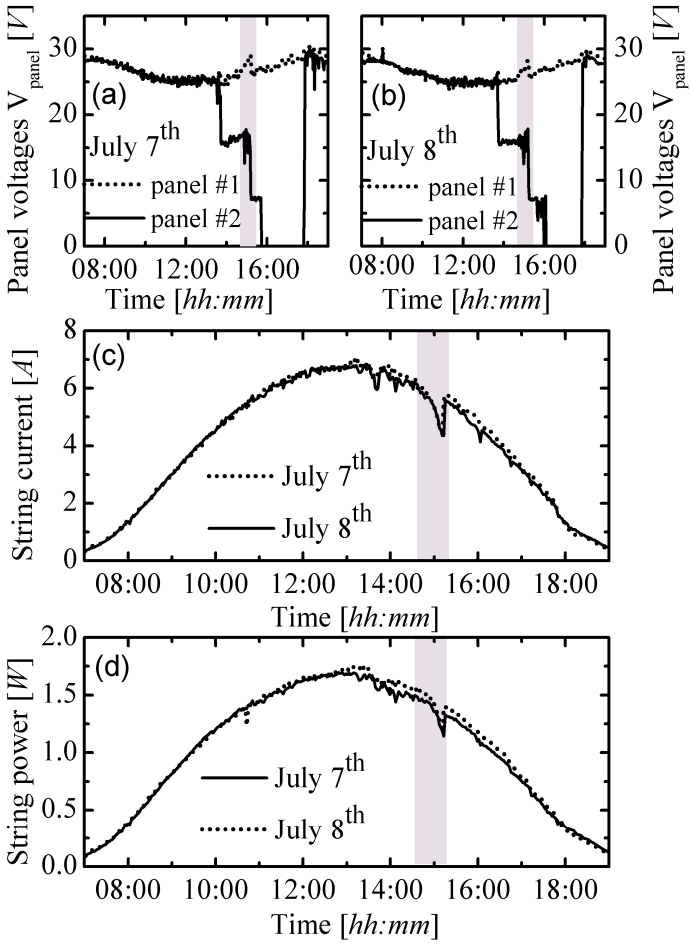

Fig 2.42 Monitoring results during two summer days for the string under test.

The reliability of the proposed dynamic reconfiguration for achieving power recovering in shaded strings is based on the capability of the proposed monitoring system to recognize conditions

in which the bypassing of some modules can be beneficial in terms of energy yield.

Monitoring results, achieved during two summer days for a 2 kWp solar string composed by 10 panels each of which equipped with three bypass diodes, are shown in Fig 2.42.

Namely, Fig 2.42a and Fig 2.42b show the operating voltages of two solar panels (panel #1, and panel #2) during the two days. In Fig 2.42a a bypass event affects the panel #2 and the ladder shape of the operating voltage suggests that a shadow is advancing over the solar panel by progressively activating the bypass diodes of the shaded subpanels. A slight increase of the voltage across panel #1 can be also observed, this is a symptom that the string is not working properly. Fig 2.42b simply shows that exactly the same behavior is observable in the following day, thus indicating that the shadow covering panel #1 was generated by an architectural obstacle.

Fig 2.42c shows the string current in the same two days. As can be seen, when panel #2 gets bypassed the string current decreases. This "unexpected" behavior is coherent with the increasing of the panel voltage previously observed. Lastly, Fig 2.42d shows the effect of the shadow on the power delivered by the string. The void shown in the figure will be recovered by reconfiguration. The inspection of Fig 2.42 indicates that no bypassed sections of panel #2, whose shadowing level is increasing, are limiting the string current; they are not yet bypassed because the MPPT is forcing the system in a local maximum in the right side of the overall P-V curve where the sunny panels work at a current lower than their I_{MPP} and, hence at a voltage higher than their V_{MPP}. Events like that are automatically detected by the remote control system tool. To this end the control system evaluate also the power P_{by} that could be produced by the string when the shaded panel is fully bypassed. P_{by} is defined according to the following formula:

$$P_{by} = \sum_{\substack{i=1 \\ i \neq J}}^{N} \left(k_i \cdot I_{SCi} \cdot k_v \cdot V_{OCi} \right) \quad (2.3)$$

where N is the number of series connected panels, I_{SCi} and V_{OCi} are measured by the monitoring system and the index J indicates the shaded panel. P_{by} is then compared with the actually produced string power, as illustrated in Fig 2.43.

The figure shows that at around 3 PM the actual produced power is lower than P_{by}, thus indicates that forcing the disconnection of the shaded solar panel allows recovering the energy corresponding to the grey area highlighted in the figure.

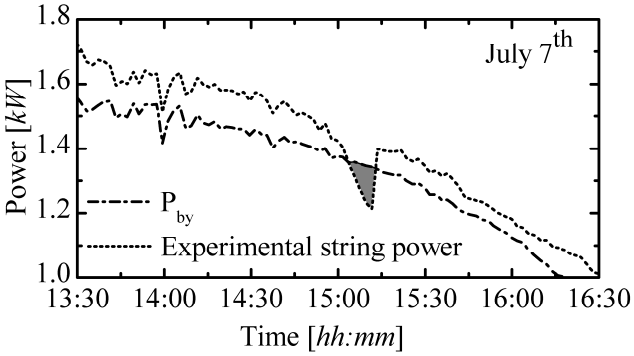

Fig 2.43 Comparison between actually produced string power and the model (2.3).

Experimental results of this method are shown in Fig 2.44. Fig 2.44a shows the normalized panel voltages measured on July 7th (no forced bypass) and on July 10th. On July 10th panel #2 is forced in disconnection at around 2.30 PM. Disconnection was anticipated with respect to time where a power gain was expected, for this reason in Fig 2.44b the power produced on July 10th is, immediately after the disconnection, lower than that produced on July 7th; while, at 3 PM, when right conditions predicted by the model occur, a higher power is measured, so the behavior predicted in Fig 2.43 was obtained. Moreover, Fig 2.44c shows that the effect of panel bypassing is to avoid string current limitation induced by the shaded panel.

The on demand disconnection of the PV sensor is an appealing feature suitable to solve security issues related to a PV plant too. The next paragraph deals with a different way to employ the developed system in order to provide safe access on PV plants, thus it can be seen as a deviation from the main topic of this work.

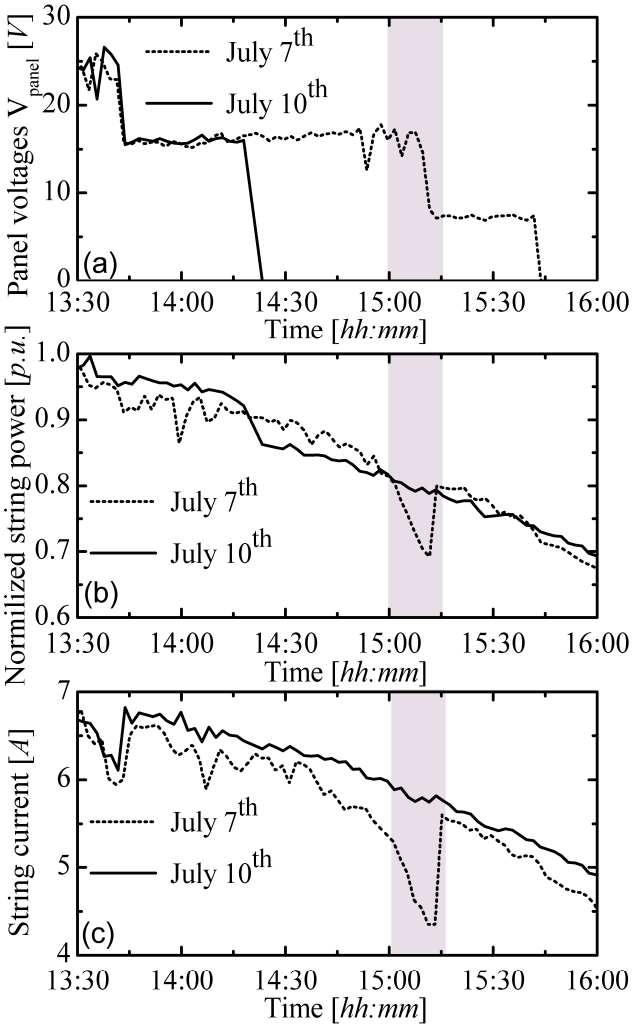

Fig 2.44 (a) panel voltage, (b) normalized string power, and (c) string current corresponding to the forced disconnection experiment.

2.8 Voltage zeroing system for safe access on PV plants

The structure of a PV field implies a harmful security risk due to the fact that also the medium size solar fields are composed by hundreds or thousands of solar panels permanently connected each

other and during daylight this involves the presence of voltages greater than hundreds of Volts, well exceeding the safety human body threshold. In other word the PV field cannot be switched off as long as the sunlight reaches solar panels.

Such high voltages can be hazardous in case of maintenance or blaze alarms. It should be noticed that the latter occurrence is nowadays dramatically rising; In Italy, where there are about 600000 PV fields, interventions raised from 1 in 2003 to 453 cases during this period [34]. Standardization rules has not prescribed specific constraints so far, mostly because reliable equipments for voltage zeroing have not been proposed yet. As a consequence, interventions in case of blaze alarms, as well as usual maintaining operations, require extreme care and highly skilled people. Moreover the firefighter intervention cannot be effective since they need to operate in absence of dangerous voltages.

The optimal features that a reliable PV plants safety system should provide have been discussed in [35] taking into account the German Association for Electrical, Electronic & Information Technologies (VDE) application guide “VDE-AR-E 2100-712:2013-05 [36]. Individual modules short circuiting was selected as the most effective solution, nevertheless there are only few examples of approaches at level of single module to accomplish this task.

It should be clearly said that PV systems exploiting distributed conversion topologies such as AC-module converters [37]-[39] or PV optimizers [40]-[43], inherently solve safety problems because in this case there is not a series connection of PV modules. Thus this paragraph only focuses on those systems adopting centralized conversion schemes, where the panels need to be series interconnected in order to reach the inverter input voltage range.

In [44] the proposed safety system is made by remote driven switches, parallel connected to each solar panel, which, either automatically, in case of specific alarms, or after pushing a devised button, short circuit the solar modules. The main drawback of this system is the need of additional wires for communication and for boards supplying.

The PV sensors with simple upgrades can be adopted as an advanced single module safety system capable to zero both voltages and currents in a solar field in a fully controllable way [45]. For this application, the PLC interface is preferable to the wireless one because it ensure a greater inner level of security, as it will be shown

later. The required upgrade is a parallel connected bistable relay with the corresponding driving circuitry. Fig 2.45 shows a block diagram of the new system with the two new required features.

It is worth noting that the disconnection system based on the Mosfet M and diode, parallel connected the PV modules plus disconnecting Mosfet, could be, in principle, considered by itself as a safety system. However, norms on circuit sectioning usually require the adoption of electromechanical devices. Both the device M and an electro-mechanical Single-Pole Single-Throw (SPST) bistable relay, parallel connected to the externally accessible connectors (S+ and S- in Fig 2.46), gives very effective performances by allowing simultaneous zeroing of both current and voltages throughout the string.

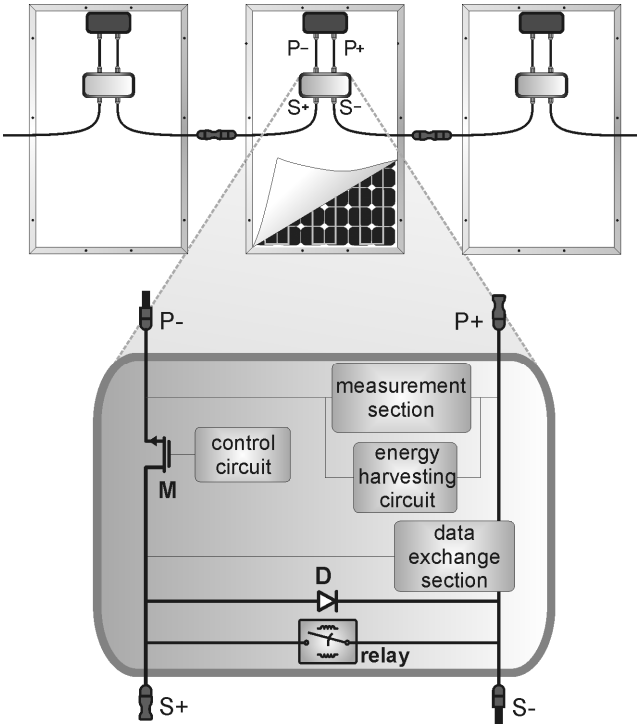

Fig 2.45 Block diagram of the proposed upgraded PV sensor.

Fig 2.46 shows the driving section of the relay. The relay is pushed in either the open or closed state through the Mosfets M_{R1} and M_{R2} which are driven by the microcontroller. In normal operating conditions the microcontroller waits, as in [5], for an "heartbeat"

coming, through the PLC, from a remote control unit; the detection of the "heartbeat" is interpreted as no alarms conditions and the relay is left open (Fig 2.47a). If the heartbeat is missed the microcontroller first opens the series Mosfet M, thus disconnecting the panel (the diode D immediately turns on and assures the continuity of the string currents during the longer switching time of the relay), then closes the relay (Fig 2.47b).

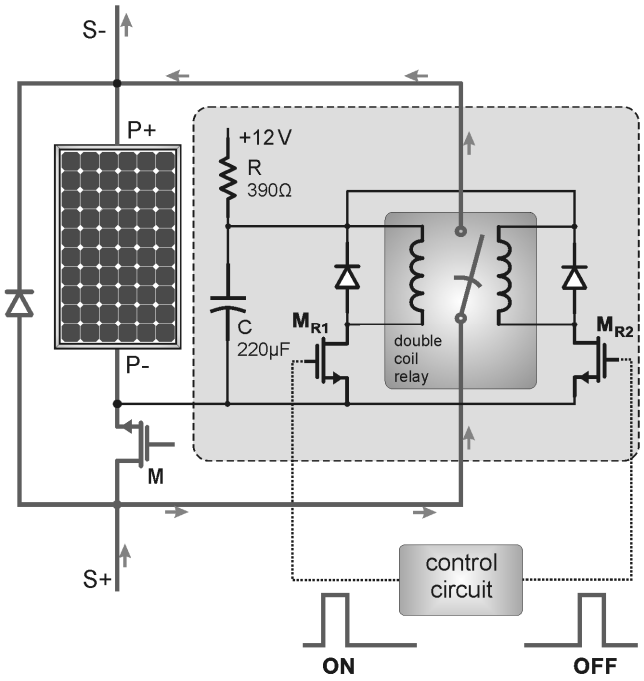

Fig 2.46 Block diagram of the upgraded disconnection section.

The heartbeat missing can be induced by simply disconnecting the string by means of a hand operated sectioning device; thus, voltage zeroing happens both when the string is voluntarily disconnected, as it is the case when someone has to intervene on the solar field, and when interruption is caused by a fault (for example when a wire is broken by fire). The system straightforward intervenes when there is lack of voltage on the grid side as well because the remote control is powered by the grid. Thanks to the presence of the series Mosfet, the circuit continues to be supplied so the disconnection state is fully reversible Fig 2.47b shows that the panel operates in V_{oc} but its externally

accessible terminals have been short circuited. Proper codified messages can be sent to eventually disconnect just single PV modules of a string as well.

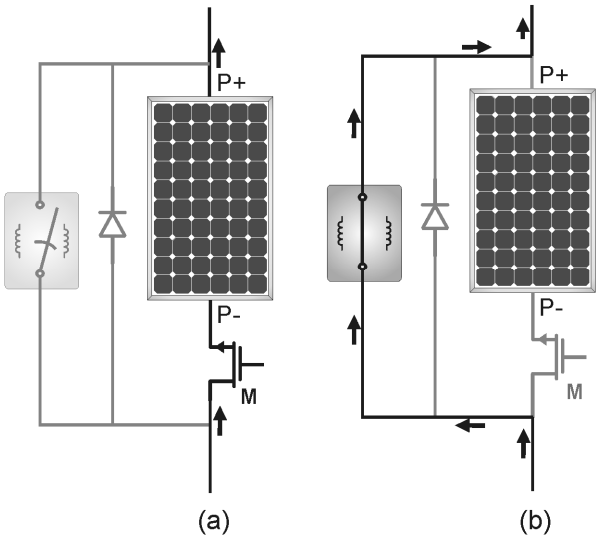

Fig 2.47 Normal operating configuration (a) and disconnection configuration (b).

The bistable relay was adopted because it has zero power consumption in both stable states. A current spur is only required to sustain the switching. In order to avoid an undesired drop in the supply of the whole circuit, the devised RC branch shown in Fig 2.46 is exploited; The capacitor C is charged through the resistor R which limits the charging current while during the relay commutation the energy is provided by the capacitor, the time constant corresponding to capacitor charging is about 80 ms.

The PV sensors of 10 modules of a solar string were equipped with this additional interface in order to experimentally test the PV string zeroing system. Fig 2.48 shows what happens when all voltages must be zeroed. In this case the heartbeat is on purpose annihilated (t=20 s in Fig 2.48) thus starting the switching of all the relays.

However, as can be inferred from the figure, in order to avoid the insurgence of a huge current spike in the input capacitance of the converter, each control circuit was instructed to wait a proper delay time before closing the corresponding relay. In the experiment, the control circuits individually calculate the corresponding delay as the

product of an assigned time period (i.e., 20 s) and their own identification number (ID). The initial gradual decrease of the voltage observable in Fig 2.48 depends on the attempt of the inverter to track the new MPP of the resulting "shorter" string. After about 60 s the string voltage becomes lower than the minimum converter input voltage, which, therefore, automatically switches off, disconnecting the input capacitor from the string. After that the string is effectively disconnected from the converter, each solar panel exhibits its open circuit voltage and the string voltage decreases step by step according to the relays short circuiting sequence.

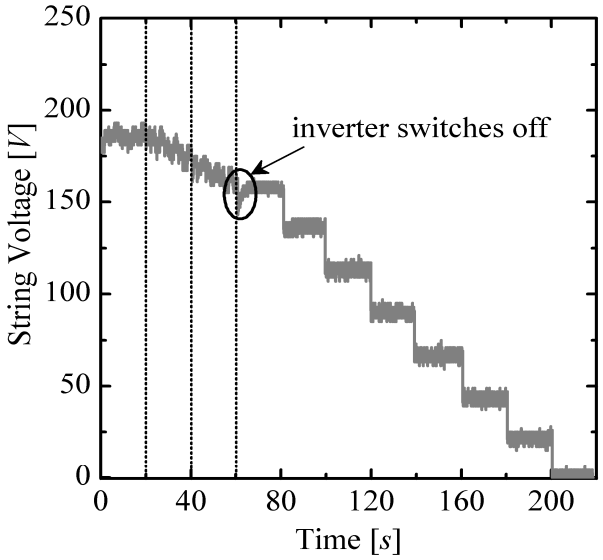

Fig 2.48 String voltage zeroing sequence.

2.9 References

[1] M. Resadi, S. Costa, and M. Cesana, “Control and signalling device for photovoltaic modules,” European Patent Application EP2159766 A1, 2010.

[2] Available: http://www.spimsolar.it/.

[3] L. Ciani, L. Cristaldi, M. Faifer, M. Lazzaroni, and M. Rossi, “Design and implementation of a on-board device for photovoltaic panels monitoring,” in Proc. IEEE I2MTC, 2013, pp. 1599-1604.

[4] J. Han, C.-S. Choi, W.-K. Park, I. Lee, and S.-H. Kim, “PLC-based photovoltaic system management for smart home energy management system,” IEEE Transactions on Consumer Electronics, vol. 60, no. 2, pp. 184-189, May 2014.

[5] F. J. Sanchez-Pacheco, P. J. Sotorrio-Ruiz, J. R. Heredia-Larrubia, F. Perez-Hidalgo, and M. Sidrach de Cardona, “PLC-Based PV plants smart monitoring system: Field measurements and uncertainty estimation,” IEEE Trans. Instrumentation and Measurement, vol. 63, no. 9, pp. 2215-2222, Sep. 2014.

[6] B. Ando, S. Baglio, A. Pistorio, G. M. Tina, and C. Ventura, “Sentinella: Smart Monitoring of Photovoltaic Systems at Panel Level,” IEEE Transactions on Instrumentation and Measurement, vol. 64, no. 8, pp. 2188-2199, Aug. 2015.

[7] M. Gargiulo, P. Guerriero, S. Daliento, A. Irace, V. d’Alessandro, et al., “A novel wireless self-powered microcontroller-based monitoring circuit for photovoltaic panels in grid-connected systems,” in Proc. IEEE Int. Symposium on Power Electronics, Electrical Drives, Automation and Motion, 2010, pp. 164-168.

[8] P. Guerriero, V. d’Alessandro, L. Petrazzuoli, G. Vallone, and S. Daliento, “Effective real-time performance monitoring and diagnostics of individual panels in PV plants,” in Proc. IEEE Int. Conf. on Clean Electrical Power, 2013, pp. 14-19.

[9] P. Guerriero, G. Vallone, M. Primato, F. Di Napoli, L. Di Nardo, V. d’Alessandro, and S. Daliento, “A wireless sensor network for the monitoring of large PV plants,” in Proc. IEEE Int. Symposium on Power Electronics, Electrical Drives, Automation and Motion, 2014, pp. 960-965.

[10] P. Guerriero, G. Vallone, V. d’Alessandro, and S. Daliento, “Innovative algorithm for true maximum detection based on individual PV panel sensor network,” in Proc. IEEE Int. Conf. on Clean Electrical Power, 2013, pp. 42-47.

[11] V. d’Alessandro, P. Guerriero, and S. Daliento, “A simple bipolar transistor-based bypass approach for photovoltaic modules,” IEEE Journal of Photovoltaics, vol. 4, no. 1, pp. 405-413, Jan. 2014.

[12] P. Guerriero, F. Di Napoli, V. d'Alessandro, and S. Daliento, "A wireless controlled circuit for PV panel disconnection in case of fire," in Proc. IEEE Int. Symposium on Power Electronics, Electrical Drives, Automation and Motion, 2014, pp. 982-986.

[13] F. Simjee and P. H. Chou, "Everlast: long-life, supercapacitor-operated wireless sensor node," in Proc. IEEE Int. Symposium on Low Power Electronics and Design, 2006, pp. 197-202.

[14] A. S. Weddell, N. R. Harris, and N. M. White, "An efficient indoor photovoltaic power harvesting system for energy-aware wireless sensor node," in Proc. Eurosensors, 2008, pp. 1544-1547.

[15] C. Alippi and C. Galperti, "An adaptive system for optimal solar energy harvesting in wireless sensor network nodes," IEEE Trans. Circuits and Systems I: Regular papers, vol. 55, no. 6, pp. 1742-1750, Jul. 2008.

[16] F. Di Napoli, P. Guerriero, V. d'Alessandro, and S. Daliento, "A Power Line Communication on DC bus with photovoltaic strings," in Proc. Renewable Power Generation Conference (RPG), 2014, pp.1-6.

[17] H. C. Ferreira, H. M. Grovè, O. Hooijen, A. J. Han Vinck. "Powe Line Communication: An Overview," in Proc. IEEE AFRICON, 2, pp. 558-563, (1996).

[18] A. Ipakchi, F. Albuyeh. "Grid of the Future," IEEE Power and Energy Magazine, 7, pp. 52-62, (2009).

[19] S. Galli, A. Scaglione, Z. Wang. "Power Line Communication and the Smart Grid," in Proc. IEEE International Conference on Smart Grid Communications (SmartGridComm), pp. 303-308, (2010).

[20] V. Giordano, F. Gangale, G. Fulli, et al. "Smart Grid projects in Europe: lessons learned and current developments," European Commission Joint Research Centre, (2011).

[21] W. Stefanutti, S. Saggini, P. Mattavelli, M. Ghioni, "Power Line Communication in Digitally Controlled DC-DC Converter Using Switching Frequency Modulation," IEEE Transaction Industrial Electronics, 55, no. 4, pp. 1509-1518, (2008).

[22] STMicroelettronics, "ST7540 FSK Power Line Transceiver," (2006).

[23] S. Daliento, V. d'Alessandro, and P. Guerriero, "Dispositivi e sistemi fotovoltaici", Edises, 2014.

[24] P. Guerriero, F. Di Napoli, V. d'Alessandro, and S. Daliento, "Accurate Maximum Power Tracking in Photovoltaic Systems Affected by Partial Shading," International Journal of Photoenergy, vol. 2015, Article ID 824832, 10 pages, 2015.

[25] P. Guerriero, F. Di Napoli, V. d'Alessandro and S. Daliento, "Experimental comparison between an "information based" MPPT algorithm and standard P&O in both partial shading and uniform illumination," in Proc. IEEE International Conference on Clean Electrical Power (ICCEP), pp 610-616,2015.

[26] D.P. Hohmand, and M.E. Ropp, "Comparative study of maximum power point tracking algorithms," Progress in Photovoltaics: Research and Applications, vol. 11, no. 1, pp. 47–62, 2003.

[27] M.A.G. de Brito, L. Galotto, L. P. Sampaio, G. de Azevedo e Melo, and C. A. Canesin, "Evaluation of the Main MPPT Techniques for Photovoltaic Applications," IEEE Transactions on Industrial Electronics, vol. 60, no. 3, pp. 1156-1167, Mar. 2013.

[28] K. Ishaque and Z. Salam, "A review of maximum power point tracking techniques of PV system for uniform insolation and partial shading condition," Renewable and Sustainable Energy Reviews, vol. 19, pp. 475–488, Mar. 2013.

[29] N. Onat, "Recent Developments in Maximum Power Point Tracking Technologies for Photovoltaic Systems," International Journal of Photoenergy, vol. 2010, Article ID 245316, 11 pages, 2010.

[30] M.Z.S. El-Dein, M. Kazerani, and M.M.A. Salama, "Optimal Photovoltaic Array Reconfiguration to Maximize Power Production under Partial Shading," in Proc. 11th International Conference on Environment and Electrical Engineering (EEEIC), 2012, pp. 255-260.

[31] G.V. Quesada, F. Guinjoan-Gispert, R. Piqué-López, M. Román-Lumbreras, and A. Conesa-Roca, "Electrical PV Array Reconfiguration Strategy for Energy Extraction Improvement in Grid-Connected PV Systems," IEEE Transactions on Industrial Electronics, vol. 56, no. 11, pp. 4319-4331, Nov. 2009.

[32] E. Storey, P.R. Wilson, and D. Bagnall, "The Optimized-String Dynamic Photovoltaic Array," IEEE Transactions on Power Electronics, vol. 29, no. 4, pp. 1768-1776, April 2014.

[33] P. Guerriero, F. Di Napoli, V. d'Alessandro and S. Daliento, "Dynamic reconfiguration of solar systems for avoiding MPPT faults due to

architectural partial shading," in Proc. IEEE 15th Internetional Conference on Environment and Electrical Engineering (EEEIC15), 2015, pp 1229-1234.

[34] G. Zaccarelli, “Pannelli fotovoltaici & incendi - Quali i principali rischi?,” available online at http://orizzontenergia.it.

[35] S. Spataru, D. Sera, F. Blaabjerg, L. Mathe, and T. Kerekes, “Firefighter safety for PV systems: Overview of future requirements and protection systems,” IEEE Energy Conversion Congress and Exposition (ECCE), pp. 4468-4475, 2013.

[36] "VDE-AR-E 2100-712:2013-05 Measures for the DC range of al PV installation for the maintenance of safety in the case of fire fighting or technical assistance,” VDE, 2013.

[37] D. Meneses, F. Blaabjerg, O. García, and J.A. Cobos, “Review and Comparison of Step-Up Transformerless Topologies for Photovoltaic AC-Module Application,” Power Electronics, IEEE Transactions on, vol. 28, no. 6, pp. 2649-2663, Jun. 2013.

[38] S.B. Kjaer, et al. , “A Review of Single-Phase Grid-Connected Inverters for Photovoltaic Modules,”IEEE Trans. on Industry Applications, vol. 41, no. 5, pp. 1292-1306, Sept. 2005.

[39] M. Coppola, P. Guerriero, F. Di Napoli, S. Daliento, D. Lauria, and A. Del Pizzo, “A PV AC-module based on coupled-inductors boost DC/AC converter,” International Symposium on Power Electronics, Electrical Drives, Automation and Motion (SPEEDAM), 2014, pp.1015-1020.

[40] N. Femia, et al., “Distributed Maximum Power Point Tracking of Photovoltaic Arrays: Novel Approach and System Analysis,” IEEE Trans. on Industrial Electronics, vol. 55, no. 7, pp. 2610-2621, 2008.

[41] G. Petrone, G. Spagnuolo, and M. Vitelli, “An analog technique for distributed MPPT PV applications,” IEEE Transaction on Industrial Electronics, vol. 59, no. 12, pp. 4713–4722, Dec. 2012.

[42] B.V.P. Chong and L. Zhang, “Controller design for integrated PV-converter modules under partial shading conditions,” Solar Energy, vol. 92, pp. 123–138, Jun. 2013.

[43] S.M. Chen, T.J. Liang, K.R. Hu, “Design, Analysis, and Implementation of Solar Power Optimizer for DC Distribution System,” IEEE Transactions on Power Electronics, vol. 28, no. 4, pp. 1764-1772, 2013.

[44] BFA-EX Solteq Datasheet, available online at: http://www.solteq.eu.

[45] F. Di Napoli, P. Guerriero, V. d'Alessandro, and S. Daliento, "Single panel voltage zeroing system for safe access on PV plants," IEEE Journal of Photovoltaic, vol. 5, no. 5, pp. 1428-1434, Sept. 2015.

Chapter 3

3 Evaluation of PV plant yield through high granularity model

3.1 Proposed strategy

In this chapter, for the first time, an high granularity model [1]-[3] accounted for small shadow effects and electrothemal behavior is presented. The photogenerated current of each cell is individually evaluated, depending on the actual irradiance distribution and its shaded area. The model is employed in an automated tool which translates a PV plant drawing made in AutoCAD [4] in the MATLAB environment. AutoCAD is a standard for architectural designers and through its powerful graphic editor is possible to draw every kind of architectural elements surrounding the PV system, while MATLAB solves the problem to find the Sun position with respect to the PV plant and the shadow evaluation. According to the shadow, MATLAB evaluates the photogenerated current for each PV cell and generates a PSpice netlist, which describes the whole PV plant at a single cell granularity level.

It should be noticed that the tool is fully automated in the sense that from the AutoCAD drawing the electrical I-V characteristics are directly generated and no specific skills regarding MATLAB and PSpice are required.

In the next paragraphs details concerning the main formulations employed by the model to evaluate the relative position between the Sun and the PV system, as well as to determine the incident solar irradiance are explained along with the algorithms to identify the shadow falling on the plant and the method to account for self-shading and masking taking place in row-composed plants.

3.2 Solar irradiance and shadow evaluation model

First the Sun position with respect to a PV panel needs to be evaluated, thus the model accounts for a complete set of parameters which describes the Sun position. In the following all angles are expressed in degrees.

Geographical information about the position of the PV plant is provided through this set of parameters:

- The longitude λ: the angular location east or west of Greenwich (positive to east, negative to west). Two values of longitude need to be defined, namely the local longitude (λ_{local}) and the longitude of the standard meridian ($\lambda_{standard}$).
- The latitude ϕ: the angular location north or south of the equator (positive to north, negative to south).
- The solar declination δ: the angle between the Sun rays (i.e., the beam radiation) and the equatorial plane, and it is positively defined in the northern hemisphere. This value can be reasonably assumed constant during a day, while changing day by day (*n* indicates the day of the year) according to the empirical Cooper's relation

$$\delta = 23.45 \cdot \sin\left[\frac{360}{365} \cdot (284 + n)\right] \quad (3.1)$$

The time at which the analysis has to be performed is another input parameter and it is indicated as clock time (CKT), this time differs from solar time, named true local time (TLT). The link between these two parameters is expressed by

$$TLT = CKT - \frac{4}{60}(\lambda_{standard} - \lambda_{local}) + \frac{Eqt}{60} \quad (3.2)$$

and

$$TLT = CKT - 1 - \frac{4}{60}(\lambda_{standard} - \lambda_{local}) + \frac{Eqt}{60} \quad (3.3)$$

where Eqt is a characteristic time referred to as *equation of time* (expressed in minutes) and it accounts for the dependence of the rate of rotation of the Earth around its axis on the day of the year due to the perturbations induced by the motion around the Sun. Its expression is presented in [1]. The relation (3.3) is valid for the days in which the daylight saving convention is adopted.

The hour angle ω is the angular displacement of the Sun east or west of the local meridian compared to the case in which TLT=12 due to the rotation from west to east of the Earth around its axis; ω is negative in the morning and positive in the afternoon. The relation between ω and TLT is given by

$$\omega = 15 \cdot (TLT - 12) \quad (3.4)$$

With this information the position of the Sun can be evaluated, by identifying the following parameters:

- The solar altitude α: the angle between the plane of horizon and the Sun rays; α is a function of latitude ϕ, solar declination δ and hour angle ω according to [5]-[7]

$$\alpha = \arcsin(\sin\delta \cdot \sin\phi + \cos\delta \cdot \cos\omega \cdot \cos\phi) \quad (3.5)$$

- The zenith angle of the Sun θ_z: the angle formed by the Sun rays and the vertical (pointing to the zenith), thus being complementary to α, and is given by [7]-[9]

$$\theta_z = \arccos(\sin\alpha) = \\ = \arccos(\sin\delta \cdot \sin\phi + \cos\delta \cdot \cos\omega \cdot \cos\phi) \quad (3.6)$$

- The solar azimuth γ_s: the angular displacement of the projection on the plane of horizon of the Sun rays from north, conventionally positive to east. It depends upon ϕ, TLT, δ, and α according to the following relations [8]

$$\gamma_s = \begin{cases} 180° - \arccos\left(\dfrac{\sin\alpha \cdot \sin\phi - \sin\delta}{\cos\alpha \cdot \cos\phi}\right) & TLT \le 12 \text{ h} \\ 180° + \arccos\left(\dfrac{\sin\alpha \cdot \sin\phi - \sin\delta}{\cos\alpha \cdot \cos\phi}\right) & TLT > 12 \text{ h} \end{cases} \quad (3.7)$$

The following step is the evaluation of the relative position of the Sun with respect to each PV module, for this reason the following parameters are employed:

- The tilt angle β: the angle between the panel and the plane of horizon.
- The azimuth angle of the panel γ: the angle formed by the south direction and the projection on the plane of horizon of the normal to the panel, conventionally considered positive from south to west (γ=0° for a south-oriented panel).
- The angle of incidence θ: the angle between the beam radiation on a tilted surface (e.g., a PV panel) and the normal to that surface, and can be evaluated from the other angles as [6], [7], [9], [10]

$$\begin{aligned} \cos\theta = &\left(\sin\phi \cdot \sin\beta \cdot \cos\gamma + \cos\phi \cdot \cos\beta\right) \cdot \cos\delta \cdot \cos\omega + \\ &+ \sin\delta \cdot \left(\cos\beta \cdot \sin\phi - \sin\beta \cdot \cos\phi \cdot \cos\gamma\right) + \\ &+ \cos\delta \cdot \sin\omega \cdot \sin\gamma \cdot \sin\beta \end{aligned} \quad (3.8)$$

The solar irradiance G [W/m^2] represents the Sun-provided power for unit area, and is given by the sum of the *beam* (or *direct*) irradiance G_b and the *diffuse* irradiance G_d. Hereinafter G_{bh} and G_{dh} refer to the beam and diffuse irradiance on the plane of horizon, respectively. It is found that (e.g., [6],[7],[11]-[13])

$$G_b = G_{bh} \cdot \frac{\cos\theta}{\sin\alpha} = G_{bh} \cdot \frac{\cos\theta}{\cos\theta_z} \quad (3.9)$$

The diffuse irradiance on a tilted panel (with width W_{panel} and height H_{panel}) for an *isotropic* sky (i.e., a homogeneous celestial hemisphere isotropically radiating, like an evenly cloudy sky) can be

obtained by multiplying G_{dh} by a view factor F_i (<1) accounting for the reduction of the sky dome due to the tilt angle. The procedure to determine F_i makes use of the cross-string approach [14] and its expression can be evaluated as [15]

$$F_i = \frac{1+\cos\beta}{2} = \cos^2\frac{\beta}{2} \quad (3.10)$$

Although more complex expressions for F_i have been determined (e.g.,[12]), (3.10) represents a widely accepted result [5]-[7], [16]-[19], and it is sometimes referred to as Kondratyev's view factor [20].

If the sky is *anisotropic* (e.g., clear or partially cloudy), G_{dh} must be multiplied by a view factor F_a accounting for horizon brightening and circumsolar radiation. It was adopted a model proposed in [11] reported also in e.g., [7], [13] given by

$$\begin{aligned} F_a &= F_{a1} + F_{a2} \\ &= F_i \cdot (1 - A_i) \cdot \left[1 + \sqrt{\frac{G_{bh}}{G_{bh}+G_{dh}}} \cdot \sin^3\left(\frac{\beta}{2}\right) \right] + A_i \cdot \frac{\cos\theta}{\sin\alpha} \end{aligned} \quad (3.11)$$

where F_{a1} is view factor associated to the isotropic portion of the sky with a correction to include horizon brightening;

F_{a2} is the view factor of the circumsolar portion of the sky.

In (3.11), $A_i=G_{bh}/G_0$ is the anisotropic index, G_0 being the irradiance incident on a horizontal plane outside the atmosphere (extraterrestrial irradiance on a horizontal surface), given by

$$\begin{aligned} G_0 = G_{sc} \cdot \left[1 + 0.033 \cdot \cos\left(\frac{360}{365} n\right) \right] \cdot \\ \cdot \left(\cos\delta\cos\phi\cos\omega + \sin\delta\sin\phi \right) \end{aligned} \quad (3.12)$$

where G_{sc} is the solar constant, equal to 1353 W/m^2. It should be noted that for a fully isotropic sky (3.11) reduces to (3.10) since G_{bh}=0 W/m^2 and thus also A_i=0.

A method based on simple geometric considerations was developed to evaluate the shadow point projected on a tilted PV panel by an individual and arbitrary point. The coordinate system is shown in Fig 3.1, where the plane of horizon is at z=0 and the x and y axes coincide with east and north, respectively according to AutoCAD world coordinate system. The coordinates (x_P, y_P, z_P) of the shadow point P_M produced by point P on a tilted panel with vertices A, B, C, D can be determined according to the following procedure. From the geometrical view point P_M is the projection of P on the PV panel plane long the Sun direction. The panel vertices are sorted according to the right hand rule, in order to obtain an orthogonal unit vector to the surface with positive z coordinate. First, it can be easily found that the unit vector parallel to the Sun rays is given by

$$\hat{i} = \left(\cos\alpha \sin\gamma_s, \cos\alpha \cos\gamma_s, \sin\alpha\right) \quad (3.13)$$

The P_M coordinates can be found as the intersection between the straight line passing through P with direction defined by î, namely, the collection of points r=(x, y, z) given by

$$r = P + t \cdot \hat{i} \qquad t \in \mathbb{R} \quad (3.14)$$

and the plane to which the module belongs, i.e., the collection of points σ=(x, y, z) obeying

$$\sigma = wB' + uD' + A \qquad u, w \in \mathbb{R} \quad (3.15)$$

where B'=B-A and D'=D-A.

The research of P_M coordinates implies the solving of this linear equations system

$$P + t \cdot \hat{i} = wB' + uD' + A \quad (3.16)$$

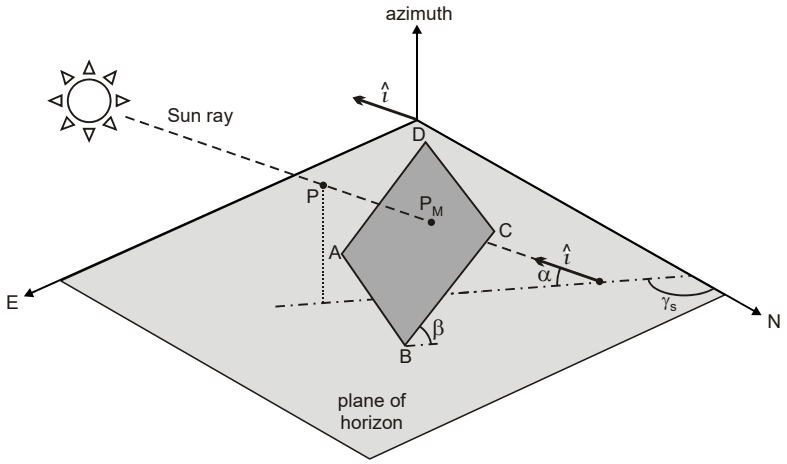

Fig 3.1 3-D sketch illustrating the shadow evaluation approach.

PV plants are usually arranged on the top of buildings in several rows in order to increase the PV area, however this implies two drawbacks: (i) *self-shading* (a row obscures the row behind) and (ii) *masking* (the portion of the hemisphere visible by a row is reduced by the row in front). These effects were investigated in various studies [6],[17]-[19], [21]-[25], they can in principle affect all the rows except for the first and depend on the spacing between rows and module heights, and are more likely to arise at low solar altitudes, namely, in the morning, in the evening, and during wintertime.

The self-shading prevents the Sun rays to reach a portion of the row behind, so that the beam irradiance G_b reduces to 0 W/m^2 over the cells belonging to that portion. The masking entails a decrease in the diffuse irradiance G_d, which is to be properly evaluated. In order to obtain the diffuse irradiance on a tilted panel in the presence of masking for an isotropic sky, G_{dh} must be multiplied by a view factor F_{im}, for the derivation of which two procedures have been proposed in the literature. The first method is based on the cross string approach and provides (3.17). Fig 3.2 represents an illustrative scheme for the evaluation of the view factor through the cross string approach.

$$F_{im} = \frac{H_{panel} + S - \overline{AD}}{2 \cdot H_{panel}} = \frac{H_{panel} + S - \sqrt{\left(H_{panel} \cdot \sin\beta\right)^2 + \left(S - H_{panel} \cdot \cos\beta\right)^2}}{2 \cdot H_{panel}} \quad (3.17)$$

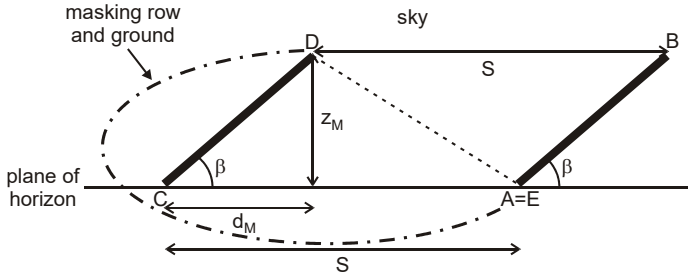

Fig 3.2 Illustrative scheme for the evaluation of the view factor between a tilted row and the isotropic sky accounting for the masking effect induced by the adjacent row in front (first method).

The second method is illustrated with reference to Fig 3.3a, the angle ψ, denoted as masking (or screening) angle, is a function of *h* according to [6], [17]

$$\psi(h) = \arctan\left(\frac{z_M - z_h}{S - d_M + h\cos\beta}\right) = \arctan\left[\frac{\left(H_{panel} - h\right)\cdot\sin\beta}{S - \left(H_{panel} - h\right)\cdot\cos\beta}\right] \quad (3.18)$$

A simplified, yet approximate, approach involves the evaluation of a mean angle

$$\psi_{AV} = \frac{1}{H_{panel}} \int_0^{H_{panel}} \psi(h)dh \quad (3.19)$$

so that

$$F_{im} = \cos^2\left[\frac{\beta + \psi_{AV}}{2}\right] \quad (3.20)$$

Both approaches have been compared for typical values of H_{panel} and $\beta=30°$, and it was found that they provide almost identical results.

Lastly, the view factor F_{am} accounting for masking for an anisotropic sky can be easily obtained by generalizing (3.11) as

$$F_{am} = F_{im}\cdot(1-A_i)\cdot\left[1+\sqrt{\frac{G_{bh}}{G_{bh}+G_{dh}}}\cdot\sin^3\left(\frac{\beta}{2}\right)\right] + A_i\cdot\frac{\cos\theta}{\sin\alpha} \quad (3.21)$$

F_{im} being given by (3.17) or (3.20).

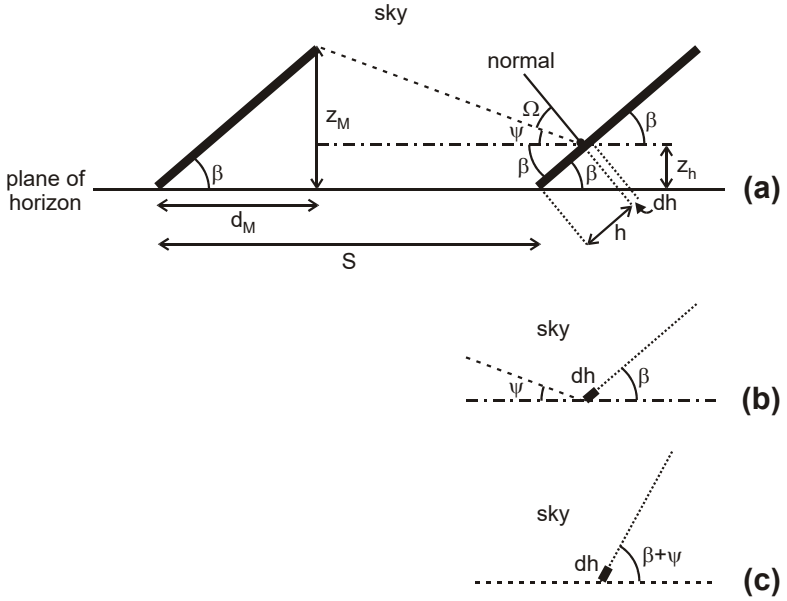

Fig 3.3 Illustrative scheme for the evaluation of the view factor between a tilted row and the isotropic sky accounting for the masking effect induced by the preceding row (second method).

3.3 Individual cell electrothermal model

The cell model proposed takes into account electrothermal (ET) effects occurring into the PV panel, namely under illumination the temperature increases, but when the module delivers power, its temperature decreases. Reliable analyses of PV systems must properly account for these ET effects because: (i) the efficiency degrades with increasing temperature, (ii) if some cells are shaded, their voltage reverses to allow the conduction of the current imposed by the sunny cells, thus giving rise to power dissipation. This may turn into hot-spot occurrences [33]-[35], which reduce the cell reliability leading to permanent damages. In order to perform correctly ET simulation the following features are required:

- a cell model allowing the variation of the temperature-sensitive parameters during the simulation run;
- a strategy to associate an individual temperature to each cell;
- an approach to enable the dynamic thermal feedback, i.e., the evaluation of the temperature of each cell at a chosen time instant from the powers dissipated by all cells, and to account for the dependence of such a temperature on the physical structure (materials, geometry) of the panel, and on the environmental conditions (wind, ambient temperature).

The above tasks are not simple to accomplish and the literature has not presented a complete solution so far, for instance in [36], a temperature-dependent model was presented for the whole module. A cell model was proposed in [37], [38] and subsequently used in [39], which includes only the temperature dependence of the inherent diode. [40], [41] deal with other models accounting for all temperature-sensitive parameters, yet neglecting avalanche effects. All attempts to perform dynamic ET simulation with a cell level granularity relay on classical approaches based on Matlab and/or Simulink, they require so much effort in terms of CPU time and memory storage, which makes them intolerable for electrical only analyses. This drawback can be minimized by employing commercial SPICE-like circuit simulators so as to exploit their robust solving engine [31]. However, these tools treat the temperature as (i) constant during the simulation and (ii) uniform for all devices; as a consequence, they cannot predict temperature gradients within a panel.

Many valuable approaches have been presented in recent years, which are based on thermal networks or numerical simulations (e.g., [35], [41], [42]-[46]) accounting for dynamic thermal model of the panel; however, the following limitations can be identified: (i) in [35], the study refers to a single cell only; (ii) in [42]-[44] it is adopted a module-level discretization; (iii) with the exception of [41], where the cell model is sequentially coupled to finite-element thermal simulations, the panel is not electrically solved, that is, the ET analysis is not enabled.

In this paragraph a strategy to perform PV plant dynamic ET simulations at level of the single cell is presented, which, for the first time, satisfies all the aforementioned tasks. The approach was developed by improving and merging the contributions presented in [47]-[49], and is based on the following strategy: (i) each module of a PV plant is represented with an equivalent electrical macrocircuit accounting for the ET behavior, which can be solved by the optimized engines of SPICE-like simulators. (ii) the macrocircuit portion describing the power-temperature feedback is automatically constructed by making use of an innovative method, which allows exceptionally fast dynamic ET analyses.

The ET simulations can also be exploited to assist the analysis and interpretation of experimental data obtained by the widely-used thermography drones [50]; the mere observation of thermal maps cannot indeed offer insight into (i) the reasons leading to temperature non-uniformities (as an example, temperature peaks are usually, yet sometimes erroneously, associated to faults), and (ii) dynamic temperature evolutions taking place within the plant.

The approach to perform ET high granularity simulation is based on the following steps which require an improved version of the PV cell circuital model, to take into account all these effects.

The PSpice temperature parameter of all components embedded in the circuit is forced to the reference value T_0=27°C. In order to make the temperature a variable which can change during the simulation and to force different temperature values for each device, the thermal equivalent of the Ohm's law is exploited, that is, the temperature rise is represented as a voltage while the dissipated power is represented as a current. The dynamic thermal behavior is accounted for through an equivalent electrical network.

The PV cell model is an enriched version of the single diode model which provides the possibility to modify the temperature-

sensitive physical parameter through the macromodeling technique which implies supplementary current/voltage-controlled sources, denoted as Analog Behavioral Modeling (ABM) parts in PSpice, which allow implementing linear and nonlinear algebraic equations. Moreover two additional terminals are embedded into the PV cell subcircuit, the first is an input port reading the rise $\Delta T=T-T_0$ (T being the cell temperature), and the other one is an output node corresponding to the dissipated power P_{cell}, which is negative as the cell generates power.

Both thermal equivalent of the Ohm's law and macromodeling technique allow each cell to be associated to a specific temperature (which is a voltage from the PSpice viewpoint) and moreover the cell modifies its behavior according to its temperature. As a result, a spatially-variable temperature field over the module can be simulated.

A thermal feedback block (TFB) is adopted to evaluate the temperature rises of all cells given their dissipated powers, which are in turn calculated as the sums of (a) the (always positive) components P_{G1}, P_{G2}, …, P_{GM} (M being the number of series-connected cells in the panel) dictated by the solar irradiances G_1, G_2, ..., G_M, each of which depending on the shaded area and (b) the macromodel outputs P_{cell}. The TFB contains an equivalent electrical circuit that fully describes the dynamic thermal behavior of the panel under test, including the thermal coupling among cells. This circuit is automatically determined in a pre-processing stage by the highly efficient tool presented in [51], which requires:

- a 3-D mesh of the panel structure with all material parameters;
- convective and radiative boundary conditions on the front and back surfaces;
- ambient temperature;
- wind direction and velocity.

As a result, the individual temperature of each cell will be modified according to the dissipated powers during the simulation run.

A sketch of the macromodel, highlighting the temperature dependence of the key parameters, is represented in Fig 3.4, along with the TFB. It can be inferred that P_{cell} is calculated as $-(I_{cell} \bullet V_{cell})$, thus being positive only when V_{cell} is negative.

The photogenerated current exhibits a positive temperature coefficient (PTC) due to the bandgap shrinking; the model adopted for this parameter is [6]

$$I_{ph} = I_{scnom} \cdot \frac{G}{G_{nom}} + \kappa \cdot (\Delta T + 2) \quad (3.22)$$

where I_{scnom} is the short-circuit current under standard test conditions (STC), i.e., nominal irradiance G_{nom}=1000 W/m^2 and cell temperature equal to 25°C, G is the actual irradiance incident on the cell, and κ [A/°C] is a temperature coefficient. Parameters I_{scnom} and κ can be obtained from the module datasheet.

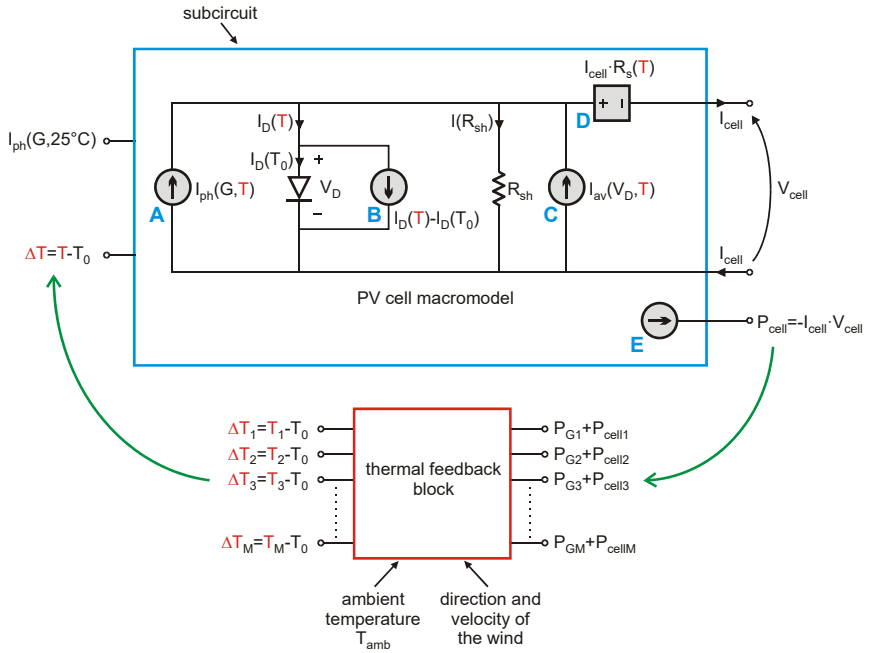

Fig 3.4 Schematic of the proposed macromodel for PV cells evidencing the ABM parts, along with the TFB.

The strategy to implement (3.22) can be described as follows. The value of G is evaluated as function of the day of the year, the TLT, the geographic location, and the shadow area upon the cell. I_{ph}(G, 25°C) is then evaluated for each cell and provided to the cell subcircuit; finally, as shown in Fig 3.4, the actual PV current I_{ph}(G, T), i.e., the LHS of (3.22), is calculated within the macromodel by the ABM component denoted as **A**, which adds κ·(ΔT+2) to I_{ph}(G, 25°C).

As far as the temperatures are more conveniently expressed in Kelvin.

The diode current I_D can be expressed as a function of voltage V_D according to the well-known Shockley equation

$$I_D = I_0 \cdot \left[\exp\left(\frac{V_D}{V_T} \right) - 1 \right] \quad (3.23)$$

where I_0 [A] is the reverse saturation current density and V_T=kT/q [V] is the thermal voltage, T [K] being the junction temperature and k=8.62×10^5 eV/K the Boltzmann's constant. The temperature dependence is hidden in the thermal voltages and in the reverse saturation current [52], and this relation is implemented for the intrinsic diode current temperature dependence:

$$I_D = I_0(T_0) \exp\left(\frac{V_D + \phi_0 \cdot \Delta T}{n V_{T0} + n \frac{k}{q} \cdot \Delta T} \right) \quad (3.24)$$

where ϕ_0 is given by [47]

$$\phi_0 = n \frac{k}{q} \cdot \left\{ 4 - m + \ln\left[\frac{C T_0^{4-m}}{I_0(T_0)} \right] \right\} \quad (3.25)$$

and *m* is the positive power factor presented in the expression of the reverse saturation current.

Fig 3.5 depicts the characteristics of the intrinsic diode for various temperatures, as determined by using (3.24).

Equation (3.24) was implemented in the macromodel through the following approach. The standard PSpice diode conducts a current $I_D(T_0)$ since the whole circuit is kept to the reference temperature T_0. The ABM part denoted with **B** in Fig 3.4 is employed to force $I_D(T)$-$I_D(T_0)$, $I_D(T)$ being given by (3.24); consequently, the current derived by the diode branch in the macromodel will be equal to $I_D(T)$.

The proposed model takes also into account the impact-ionization (II) mechanism arises for those cells which exhibit reverse voltage due to shaded conditions. This effect is taken into account by extending the model proposed in [26]: the total current I_{cell} is given by the sum of the current that would flow in the absence of II, and an avalanching current I_{av} computed by the ABM **C** and given by

$$I_{av} = -\frac{V_D}{R_{sh}} \cdot a_{II} \cdot \left[1 - \frac{V_D}{BV(T)}\right]^{-m_{II}} \quad (3.26)$$

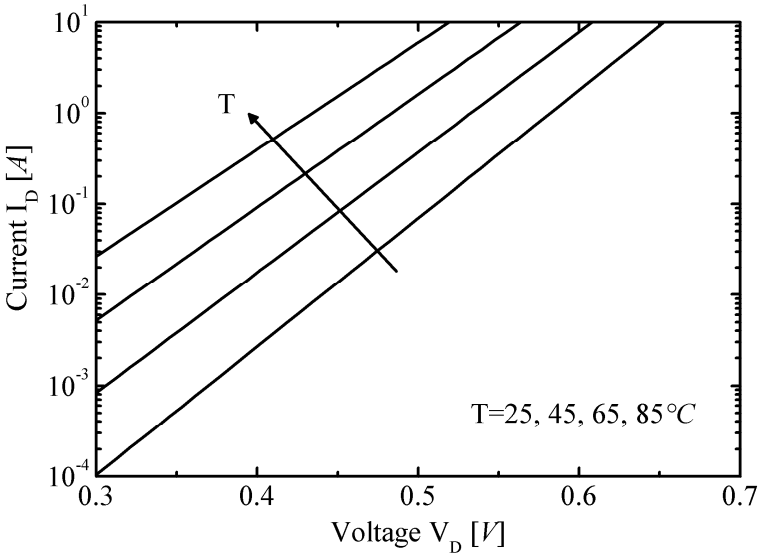

Fig 3.5 I_D-V_D characteristics, as determined through (3.24) for various temperatures.

where R_{sh} is the shunt resistance [Ω], coefficient a_{II} and power factor m_{II} are dimensionless fitting parameters, and BV (<0 V) is the breakdown voltage of the cell, the temperature dependence of which can be enabled through the relation

$$BV(T) = BV(T_0) \cdot \exp(b_{II} \cdot \Delta T) \quad (3.27)$$

b_{II} [K^{-1}] (>0) being another fitting parameter.

A PTC for the series resistance R_s [Ω] is accounted for by adding a voltage drop given by the product between the cell current I_{cell} and R_s, for which a power dependence on temperature is considered, i.e.,

$$R_s(T) = R_s(T_0) \cdot \left(\frac{T}{T_0}\right)^{m_R} = R_s(T_0) \cdot \left(\frac{T_0 + \Delta T}{T_0}\right)^{m_R} \quad (3.28)$$

with m_R dimensionless fitting parameter > 0, although in principle any other laws (e.g., exponential [53] or linear) can be implemented. This is put into practice by making use of the ABM designated as **D** in Fig 3.4, which accepts the temperature rise ΔT and the current I_{cell} (transformed into a voltage) as inputs, and imposes the drop $I_{cell} \cdot R_s(T)$. Fig 3.6 illustrates the approach to follow in order to simulate a non linear resistor characteristic.

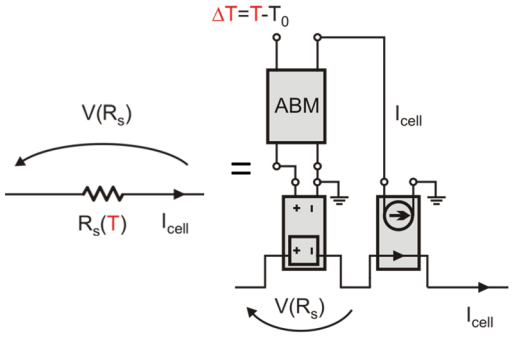

Fig 3.6 Magnification of the ABM designated as D in Fig 3.4.

The shunt resistance is instead assumed to be temperature-insensitive; nevertheless, R_{sh} might exhibit an NTC induced by the thermal trapping-detrapping of carriers through the defect states in the space-charge region [54], which can be effortlessly included by using an approach similar to that applied to R_s.

In this work a macromodel of the cells embedded in the ET-M54050 50 Wp solar panel [55] is presented. All the parameter values used for the simulations shown in the chapter are reported in Tab 3.1.

Parameter	**Value**
I_{scnom}	2.8 A
K	1.69 mV/°C
$I_0(T_0)$	8 nA
N	1.2
ϕ_0	4.4 mV/°C
$BV(T_0)$	-10 V
a_{II}	0.1
m_{II}	1.1
R_{sh}	100 Ω
$R_s(T_0)$	12 mΩ
m_R	1.5

Tab 3.1 Values of the macromodel parameters.

Fig 3.7 shows the isothermal I_{cell}-V_{cell} curves for different temperature values obtained through the proposed macromodel. In this case the TFB was deactivated since a static analysis, with all cells at same temperature, was performed. Also the characteristics in STC and normal operating cell temperature (NOCT) conditions (namely, G_{nomT}=800 W/m^2 and T=45°C) are simulated.

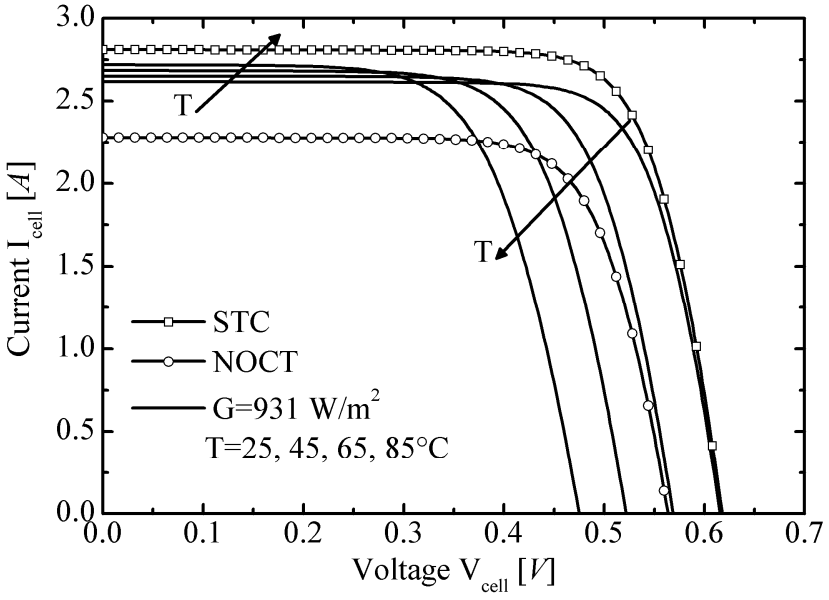

Fig 3.7 I_{cell}-V_{cell} characteristics evaluated through the proposed macromodel for various operating conditions.

The dynamic power-temperature feedback is modeled for each panel (panels are assumed to be thermally-independent, the thermal coupling is only evaluated among cells of the same PV module) by means of TFB, which is built in a preprocessing merely-thermal analysis through the following procedure. First, according to datasheet and to the information about material parameters and geometry (Fig 3.8, Tab 3.2 and Tab 3.3), a 3-D mesh representing the panel is generated. In this work, the commercial software package Comsol [56] was adopted, by exploiting the selective meshing features since the horizontal dimensions are much larger than the thicknesses. The external aluminum was neglected due to its small size.

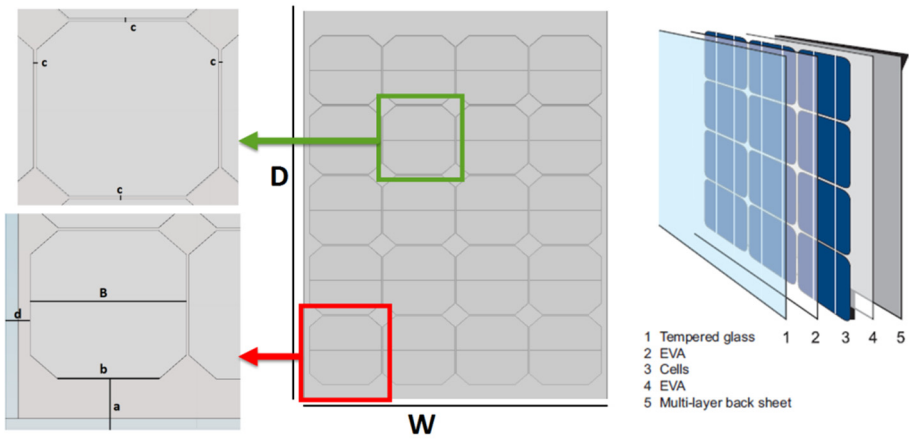

Fig 3.8 Solar panel geometry data.

Thickness [mm]	**Module** [mm]	**Cell** [mm]	**Spacing** [mm]
Glass = 3 EVA = 2.15 Si celss = 0.15 Back = 1	D = 719 W = 555	B = 127.25 b = 82	a= 32 d = 20 c = 2

Tab 3.2 Values of the geometric parameters depicted in Fig 3.8.

Material	ρ [kg/m^3]	c [J/kgK]	k [W/mK]
Glass	3000	500	1.8
EVA	960	2090	0.35
Si cells	2330	677	148
Tedlar	1200	1250	0.15

Tab 3.3 Values of the material parameters (mass density ρ, specific heat c, thermal conductivity k).

An important issue is the choice of the correct boundary conditions (BCs) for the model. The following BCs have been considered, as depicted in Fig 3.9.

The top surface of the panel is subject to the incident wind. Therefore both forced and free convection are considered. Moreover, radiant heat is emitted towards the sky from the top surface.

The bottom surface is assumed to be shielded from the wind, i.e., only free convection and radiant heat towards the ground are considered.

The side surfaces are assumed adiabatic, i.e. the thermal exchange through them is assumed negligible due to their small dimensions with respect to the top and bottom surfaces.

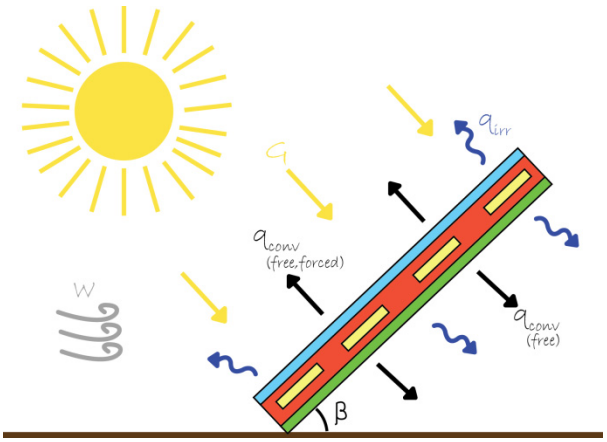

Fig 3.9 Schematic representation of the BCs.

The free convection is modelled according to the approach described in [43]; the forced convection is described by slightly modifying results obtained in [57] according to information on the wind speed available from [58]. The heat transfer coefficient *h* accounting for both free and forced convection on the front is then determined as [43]

$$h = \sqrt[3]{\left(h_{free}^2 + h_{forced}^2\right)} \quad (3.29)$$

The power densities [W/m^2] exchanged between front/back surfaces and ambient due to the radiative contribution are given by [43]

$$q_{irr,front} = F_{front}\varepsilon_{front}\sigma_{front}(T_{front}^4 - T_{sky}^4) \quad (3.30)$$

$$q_{irr,back} = F_{back}\varepsilon_{back}\sigma_{back}(T_{back}^4 - T_{ground}^4) \quad (3.31)$$

where ε is the emissivity (for the back is the emissivity of tedlar and for the front the emissivity of glass), σ [W/m^{2}K^4] is the Stephan-Boltzmann constant, T_{sky} =T_{ground} =T_{amb}, T_{amb} being the

ambient temperature, F_{front} and F_{back} are the front-sky and back-ground view factors expressed as

$$F_{front} = \frac{1+\cos\beta}{2} \quad (3.32)$$

$$F_{back} = \frac{1-\cos(180-\beta)}{2} \quad (3.33)$$

β being the tilt angle of the panel.

Each solar cell is modeled with a heat source; moreover, in order to model the nonlinear radiant heat BCs, additional heat sources on the top and the back surface are considered by discretizing the surfaces with rectangles on top of the cells. The total number of heat sources is 122 while the PV panel is composed by 40 cells. Each heat source corresponds to a pair of terminals: an input node for dissipated power and an output one for average temperature rise over ambient. The dissipated power inputted to the cell is given by the sum of a first positive contribute due to the incident power from the Sun, diminished by the reflection and absorption of the layer on top of the cells, and a negative contribute due to the generated electrical power obtained from the circuit cell model. The power and temperature corresponding to surface discretization are closed in an internal feedback loop with a nonlinear arbitrary generator in order to model the radiant heat transfer and are not available from the outside.

The TFB of the panel is automatically built from the BCs and the 3-D Comsol mesh by resorting to an advanced in-house code [51].

The TFB evaluates the temperatures of all cells for each time instant. The subcircuits of the cells belonging to the same panel are automatically connected to the TFB. Panel circuits can be in turn connected to give rise to a macrocircuit representing a PV plant, the solution of which is demanded to PSpice. As a result, all voltages and currents (including those corresponding to temperatures and powers, respectively) are determined for each time instant.

3.4 The tool

The block diagram of the tool is sketched in Fig 3.10. Starting from user provided information concerning λ_{local}, $\lambda_{standard}$, ϕ, n, CKT, the following parameters are evaluated δ, ω, α, θ_z, γ_s, θ.

Those works [17], [19], [23] provide the possibility to determine only the shadows cast by obstacle with simple geometry, even if they exploit complex mathematical formulations, while the proposed tool allows describing arbitrary obstacles. The approach is based on the following steps:

- The whole scenario under analysis, namely, the PV plant and the surrounding obstacles, are drawn within the AutoCAD environment. The external surface of an obstacle is constructed by composition of elementary polygons.
- A custom parsing routine transfers the AutoCAD scene into the Matlab environment by preserving all the geometrical information. The parsing procedure reads the .dxf file, which is an exchange format text file produced by AutoCAD and identifies both the coordinates of obstacles and PV cells.
- The shadow cast by an obstacle on the plant is obtained by "overlapping" the individual shadows of the aforementioned polygons, each of which is identified by the shadow points corresponding to the polygon vertices.

The tool receives the hourly horizontal irradiance and ambient temperature (T_{amb}) as input data; this information can be provided by measurements through sensors directly mounted on the PV field under analysis or by means of databases, which collect historic weather observations for different locations and provide this information for the "mean" day of a chosen month. For the simulations presented in this chapter the online database PhotoVoltaic Geographical Information System (PVGIS) [30] was exploited. This database is made available by the Joint Research Center of Ispra (Italy). It offers the evolutions of the total horizontal irradiance (G_{bh}+G_{dh}) for real and clear sky conditions, as well as of the diffuse horizontal irradiance (G_{dh}). Once the shadow pattern is defined, the beam (G_b) and diffuse (G_d) irradiances for each cell are determined by invoking the aforementioned formulations.

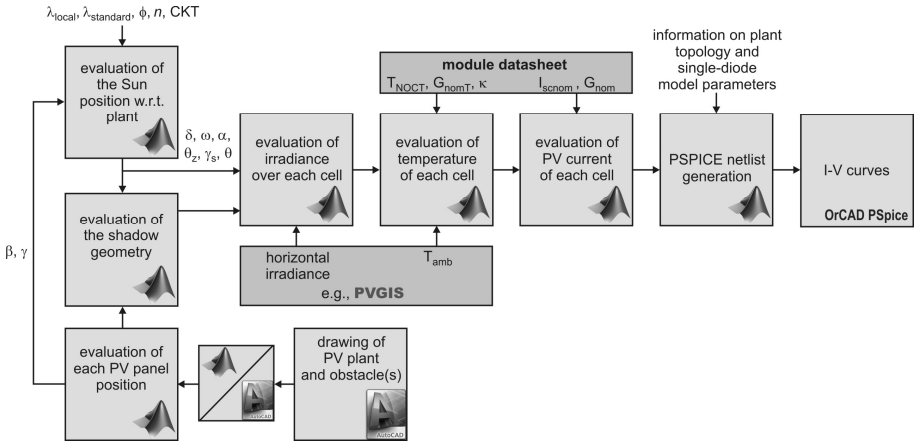

Fig 3.10 Block diagram of the proposed tool.

The total irradiance G hitting the cell is then calculated as G_b+G_d, G_b being set to 0 W/m^2 for shaded areas. If the cell is partially shaded, I_{ph} is computed by first determining the area of the shaded portion A_{shaded}, and then resorting to the weighted average

$$I_{ph} = \frac{1}{A_{cell}}\left[I_{ph,unshaded} \cdot \left(A_{cell} - A_{shaded} \right) + I_{ph,shaded} \cdot A_{shaded} \right] \quad (3.34)$$

where A_{cell} is the cell area, and $I_{ph,unshaded}$ and $I_{ph,shaded}$ are the PV currents corresponding to the unshaded and shaded cell fractions, respectively.

Afterward, starting from information on the parameter values of the ET cell model, a Matlab code automatically generates the netlist corresponding to the whole PV plant, where each cell exhibits its own I_{ph} and T. All cells belonged to the same PV module are connected to a unique TFB and the couple PV module subcircuit and TFB are linked according to the PV field electrical schematic. Lastly, the netlist is solved by PSpice.

3.5 Experiments

Fig 3.11 shows the string under test composed by 10 mono-crystalline silicon 50 Wp ET-M54050 modules each of which composed by two subpanels (Fig 3.8, Tab 3.1, Tab 3.2 and Tab 3.3). The string is mounted on the rooftop of the Department of Electrical

Engineering and Information Technology, Naples, Italy. The panels are inclined with β=30°; the azimuth angle γ was estimated to be -16°. The static I-V characteristics were measured through an H&H ZS3060 electronic dc load rated for 3 kW and 800 V, and a data acquisition section involving two PC-controlled 2000 Keithley multimeter units synchronized by a home-made board to improve the measurement accuracy.

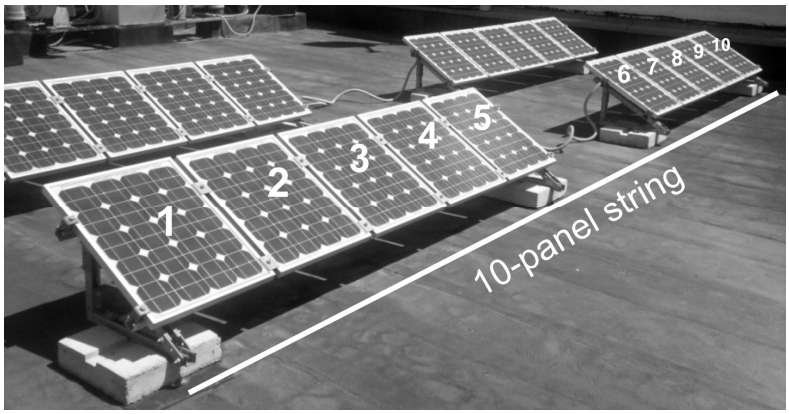

Fig 3.11 String under test (the string behind is inactive).

The first analysis was performed in order to verify the greater accuracy of the proposed tool with respect to a commercial wide adopted tool. In this test a pole standing in front of the string at a 1 m distance was considered. Fig 3.12a and Fig 3.12b illustrate the favorable matching between the real shadow which affects module #10 at noon, December 17 (n=351), and the one computed by the proposed tool.

Fig 3.12c reports the I-V characteristic experimentally determined and the simulated one by the PSpice section of the proposed tool. The agreement is fairly good, the discrepancy being ascribable to the unavoidable error affecting the input G_{bh} and G_{dh} data, which are not measured but obtained from PVGIS. For the 400-cell string under test, the CPU time corresponding to the PSpice simulation of an I-V curve was found to be about 40 seconds on a normal PC. Fig 3.12c also shows the I-V curve simulated through an advanced commercial software devised for energy yield estimation of PV systems. Both the string and the obstacle were constructed in the

software environment, and the parameters of the individual modules were set to the values taken from the datasheet.

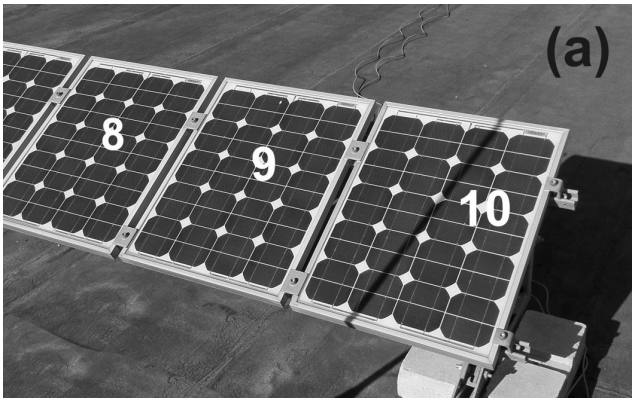

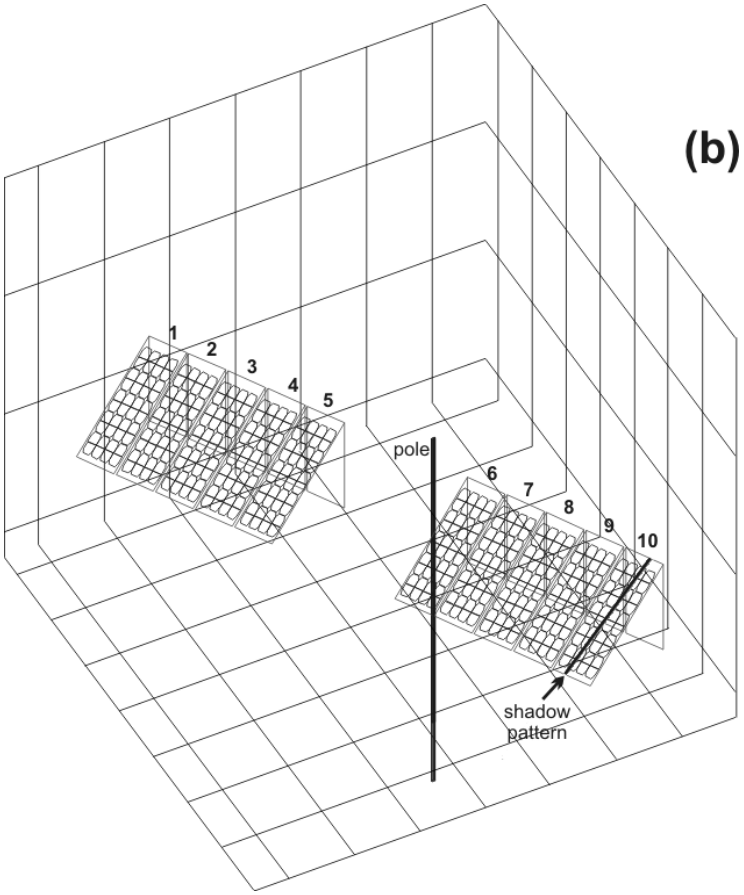

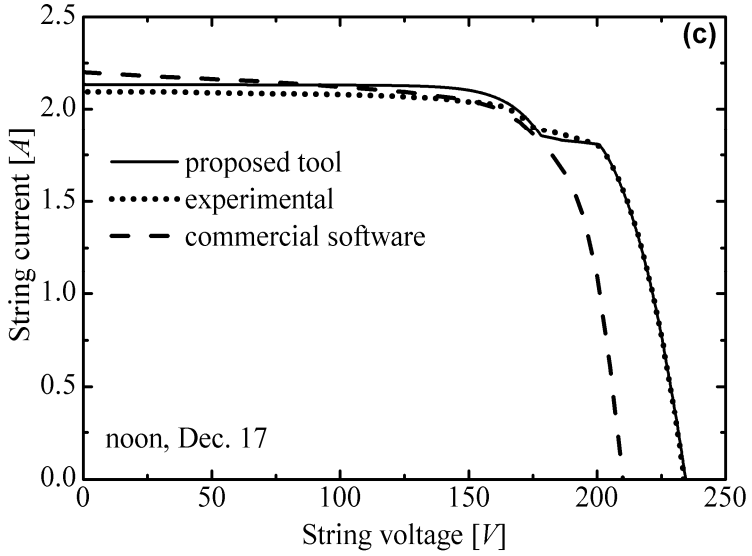

Fig 3.12 Shadow due to a pole placed in front of the string at noon, December 17: (a) real scenario; (b) 3-D representation obtained through the proposed tool; (c) I-V characteristic, as determined by the proposed tool, measurements, and by a commercial software package.

The comparison reveals that the commercial software totally disregards the impact of the small shadow projected by the pole on the I-V curve, which is somewhat "missed" although falling on two subpanels. Furthermore, this curve is also quite different from the experimental sunny counterpart. An extensive analysis was conducted, which allowed concluding that (i) the commercial software does not take properly into account the effects related to the temperature, (ii) it may significantly underestimate or overestimate small-shadow effects on the electrical characteristics, and consequently on the energy yield, (ii) only obstacles with simple geometries can be drawn.

A second study was conducted in order to estimate the losses induced by permanently small area shadows on the PV field, in this case a realistic TV antenna was drawn in the PV plant scenario. It is worth noting that this obstacle cannot be reproduced in alternative programs. Fig 3.13a and Fig 3.13b show the calculated shadow and the electrical characteristics at noon, September 15 (n=255), respectively. It can be noted that the P-V curve exhibits an irregular behavior (with two maxima) induced by the non-uniform shading over both subpanels belonging to module #4.

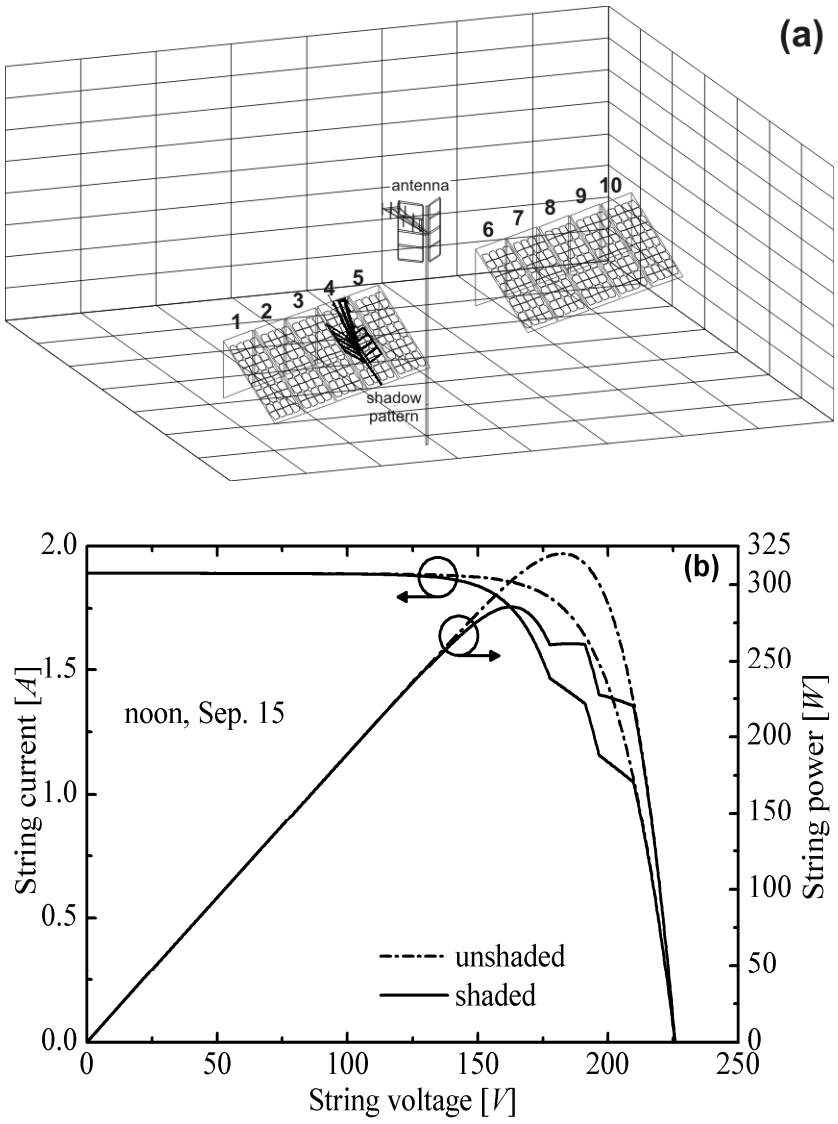

Fig 3.13 (a) Shadow due to a TV antenna placed in front of the string at noon, September 15, and (b) corresponding electrical characteristics compared to those obtained by removing the antenna; all results were obtained through the proposed tool.

Fig 3.14 provides the average daily energy along one year, which is evaluated through the following procedure:

- the I-V characteristic of the string was determined at each sunlight hour of the 15th day of each month;
- detection of the MPP for each I-V curve;

- the daily energy was computed by integrating the evolution of maximum power over the sunlight hours of the day;
- in the occurrence of multiple power maxima, two MPP trackers were emulated: (i) an *ideal* one (namely a distribute MPPT) suited to always reach the global maximum and (ii) a potential P&O faulty, which can fix the operating point in the local maximum closest to the open-circuit voltage V_{oc}.

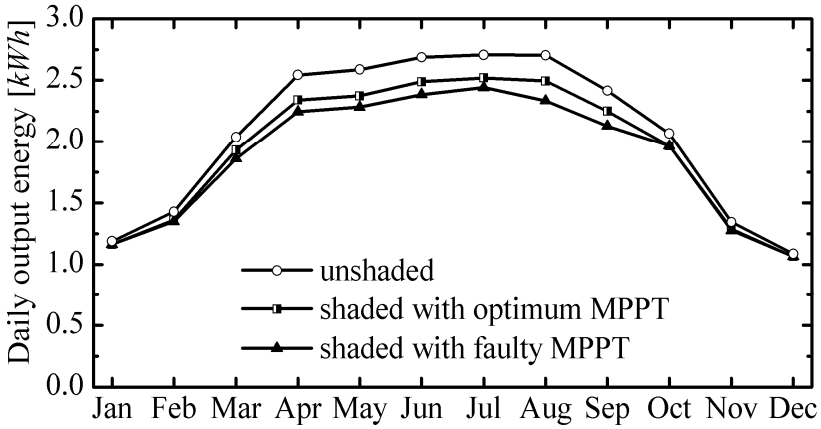

Fig 3.14 Energy produced by the string under test along one year; the curve simulated under sunny conditions is compared to that obtained by placing a TV antenna in the same position as in Fig 3.13b with an optimum and a faulty MPP tracker.

Fig 3.14 proves that in spite of the small shaded area the TV antenna may lead a reduction in the energy yield of the whole year, which for the scenario under investigation amounts to about 6.3% in case of ideal MPPT and 9.3% for a centralized MPPT approach.

Another study was performed in order to analyze the impact of self-shading and masking effect. In this case was placed in front of the string under test an obstacles which emulates another row of panels. The distance S (see Fig 3.2) between them is reduced from 1.37 m (at which no self-shadow is cast on noon, December 21) to 0.68 m.

Fig 3.15, illustrates the average daily energy provided in all the months of the year, if the spacing S between strings is too small, the combined action of self-shading and masking due to the preceding row entails a dramatic collapse in the string production, especially in the months with low solar altitude. In particular, compared to the case

in which no row is located in front, the yearly energy reduces by 3.8% (S=1.37 m), 13.5% (S=1.03 m), and 49% (S=0.68 m).

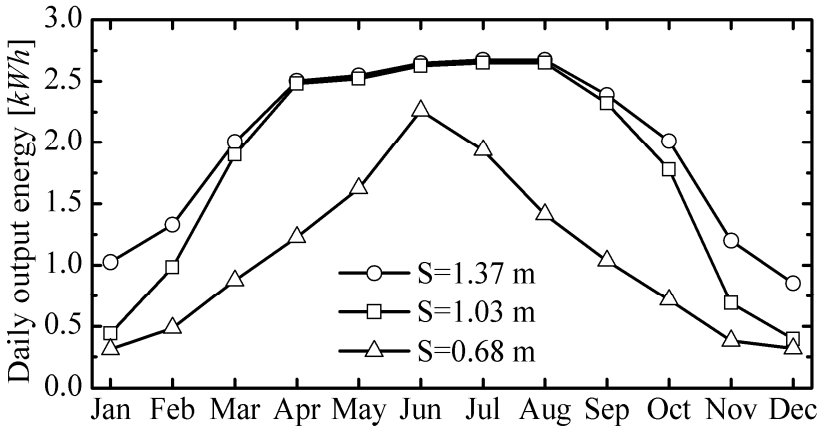

Fig 3.15 Daily energy produced by the string under test along one year, as simulated by our tool in the presence of a preceding string with spacing S amounting to 1.37, 1.03, and 0.68 m.

Other simulations were performed in order to understand how a module responds in terms of ET effect to an architectural shadow falling on one of the panel of the string under test with the pattern evolution illustrate in Fig 3.16 during 33 minutes-long time frame. In this case a realistic MPPT action was accounted for.

After the first two minutes, when the shadow covers the first cell, this cell warms considerably up (Fig 3.16c) generating a hot-spot. When the shaded area slight increases a non intuitive result is obtained, namely the temperature of shaded cells decreases while the fully lighted cells warm up. This is a non intuitive result because there is the balancing of two opposite effects, the shaded cells have less irradiance so they temperature should decrease but they are also reversed bias, increasingly their dissipated powers. It is worth noting that only this tool can provide this type of analyses thanks to the proposed strategy which provides the possibility to change the temperature during the simulation run.

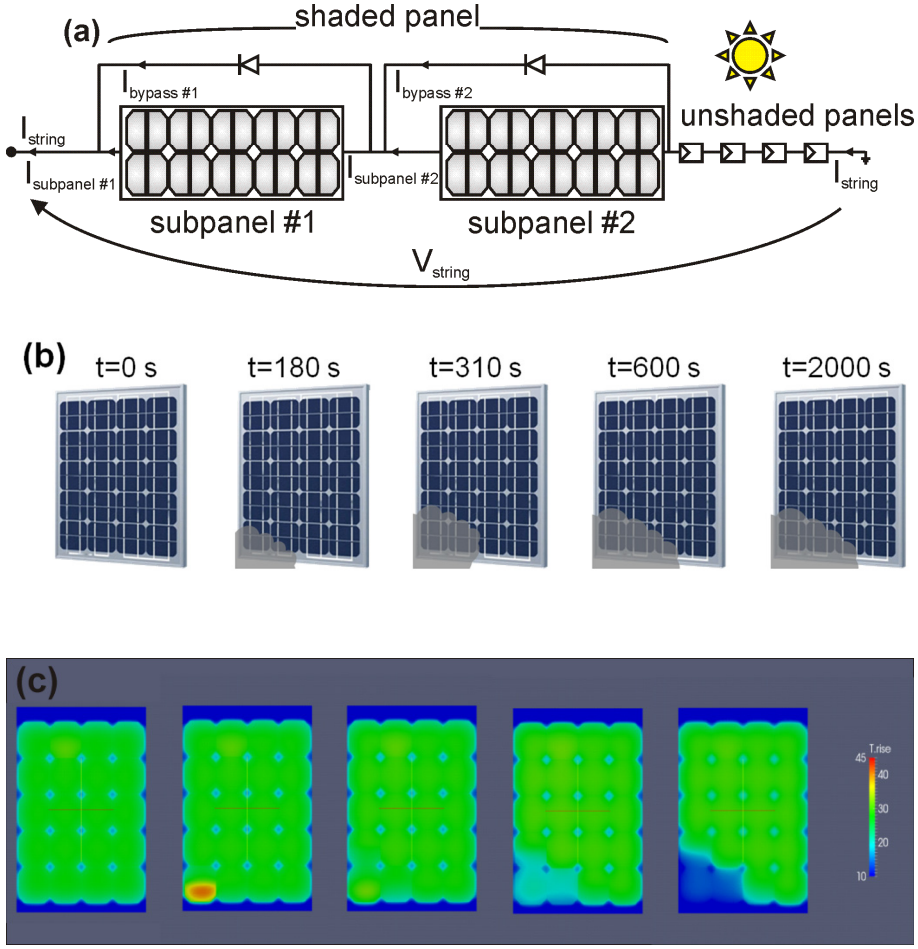

Fig 3.16 Schematic representations of (a) the string under test and of (b) the shadow pattern vs. time on the shaded panel (c) temperature field of the shaded module.

3.6 References

[1] V. d'Alessandro, F. Di Napoli, P. Guerriero, and S. Daliento, "An automated high-granularity tool for a fast evaluation of the yield of PV plants accounting for shading effects," Renewable Energy, vol. 83, pp. 294-304, November 2015.

[2] P. Guerriero, F. Di Napoli, F.Cominale, V. d'Alessandro, and S. Daliento, "Accurate analysis of small shadows effects on photovoltaic systems yield," in Proc. IEEE International Symposium on Power

Electronics, Electrical Drives, Automation and Motion (SPEEDAM), 2014, pp. 987-992.

[3] F. Di Napoli, V d'Alessandro, S. Daliento, and P. Guerriero, "Accurate yield prediction for PV plants in the presence of shadows due to fully arbitrary obstacles," in Proc. 46th Conference del Gruppo Elettronica (GE) 2014.

[4] AutoCAD, User's Manual, Autodesk Building Design Suite, 2012.

[5] N. Robinson, Solar radiation. Elsevier, New York, 1966.

[6] D. Passias and B. Källbäck, "Shading effects in rows of solar cell panels," Solar Cells, vol. 11, no. 3, pp. 281-291, 1984.

[7] J. A. Duffie and W. A. Beckman, Solar engineering of thermal processes. John Wiley & Sons, 2006.

[8] U. Eicker, Solar technologies for buildings. John Wiley & Sons, 2003.

[9] G. N. Tiwari and S. Dubey, Fundamentals of photovoltaic modules and their applications. The Royal Society of Chemistry, Cambridge, UK, 2010.

[10] S. B. Sadineni, R. F. Boehm, and R. Hurt, "Spacing analysis of an inclined solar collector field," in Proc. ASME 2nd International Conference on Energy Sustainability, 2008, pp. 417-422.

[11] D. T. Reindl, W. A. Beckman, and J. A. Duffie, "Evaluation of hourly tilted surface radiation models," Solar Energy, vol. 45, no. 1, pp. 9-17, 1990.

[12] V. Quaschning and R. Hanitsch, "Shade calculations in photovoltaic systems," in Proc. ISES Solar World Conference, 1995.

[13] H. Yang and L. Lu, "The optimum tilt angles and orientations of PV claddings for building-integrated photovoltaic (BIPV) applications," ASME Journal of Solar Energy Engineering, vol. 129, no. 2, pp. 253-255, 2005.

[14] H. C. Hottel and A. F. Sarofin, Radiative transfer. McGraw-Hill, New York, 1967.

[15] T. Maor and J. Appelbaum, "View factors of photovoltaic collector systems," Solar Energy, vol. 86, no. 6, pp. 1701-1708, 2012.

[16] B. J. Garnier and A. Ohmura, “The evaluation of surface variations in solar radiation income,” Solar Energy, vol. 13, no. 1, pp. 21-34, 1970.

[17] J. Appelbaum and J. Bany, “Shadow effect of adjacent solar collectors in large scale systems,” Solar Energy, vol. 23, no. 6, pp. 497-507, 1979.

[18] R. E. Jones and J. F. Burkhart, “Shading effects of collector rows tilted toward the equator,” Solar Energy, vol. 26, no. 6, pp. 563-565, 1981.

[19] J. Bany and J. Appelbaum, “The effect of shading on the design of a field of solar collectors,” Solar Cells, vol. 20, no. 3, pp. 201-228, 1987.

[20] K. Ya. Kondratyev, Radiative heat exchange in the atmosphere. Oxford, Pergamon Press, 1965.

[21] O. Barra, M. Conti, E. Santamata, R. Scarmozzino, and R. Visentin, “Shadows’ effect in a large scale solar power plant,” Solar Energy, vol. 19, no. 6, pp. 759-762, 1977.

[22] P. P. Groumpos and K. Khouzam, “A generic approach to the shadow effect of large solar power systems,” Solar Cells, vol. 22, no. 1, pp. 29-46, 1987.

[23] D. Weinstock and J. Appelbaum, “Optimal solar field design of stationary collectors,” ASME Journal of Solar Energy Engineering, vol. 126, no. 3, pp. 898-905, 2004.

[24] S. Elies, T. Reis, B. Müller, U. Kräling, and K. Kiefer, “Influence of row-shading on the performance of PV systems – Simulation and measurement,” in Proc. European Photovoltaic Solar Energy Conference and exhibition, 2010, pp. 4640-4646.

[25] K. Brecl and M. Topič, “Self-shading losses of fixed free-standing PV arrays,” Renewable Energy, vol. 36, no. 11, pp. 3211-3216, 2011.

[26] J. W. Bishop, “Computer simulation of the effects of electrical mismatches in photovoltaic cell interconnection circuits,” Solar Cells, vol. 25, no. 1, pp. 73-89, 1988.

[27] R. A. Messenger and J. Ventre, Photovoltaic System Engineering. CRC Press, Boca Raton, 2004.

[28] H. S. Rauschenbach, Solar cell array design handbook. Van Nostrand Reinhold Co., 1980.

[29] M. G. Villalva, J. R. Gazoli, and E. Ruppert Filho, “Comprehensive approach to modeling and simulation of photovoltaic arrays,” IEEE Transactions on Power Electronics, vol. 24, no. 5, pp. 1198-1208, 2009.

[30] PVGIS: http://re.jrc.ec.europa.eu/pvgis/ (Dec. 2013)

[31] PSPICE, User’s Manual, Cadence OrCAD 16.5, 2011.

[32] V. d’Alessandro, P. Guerriero, S. Daliento, and M. Gargiulo, “A straightforward method to extract the shunt resistance of photovoltaic cells from current–voltage characteristics of mounted arrays,” Solid-State Electronics, vol. 63, no. 1, pp. 130-136. 2011.

[33] S. Wendlandt, A. Drobisch, T. Buseth, S. Krauter, and P. Grunow, “Hot spot risk analysis of silicon cell modules,” in Proc. EUropean PhotoVoltaic Solar Energy Conference (EUPVSEC), pp. 4002-4006, (2010).

[34] K. A. Kim and P. T. Krein, “Photovoltaic hot spot analysis for cells with various reverse-bias characteristics through electrical and thermal simulations,” in Proc. IEEE workshop on COntrol and Modeling for Power Electronics (COMPEL), (2013).

[35] D. Giaffreda, P. Magnone, M. Meneghini, M. Barbato, G. Meneghesso, E. Zanoni, E. Sangiorgi, and C. Fiegna, “Local shunting in multicrystalline silicon solar cells: Distributed electrical simulations and experiments,” IEEE Journal of Photovoltaics, 4, 1, pp. 40-47, (2014).

[36] J. P. Kim, H. Lim, J. H. Song, Y. J. Chang, and C. H. Jeon, “Numerical analysis on the thermal characteristics of photovoltaic module with ambient temperature variation,” Solar Energy Materials & Solar Cells, 95, 1, pp. 404-407, (2011).

[37] P. Maffezzoni and D. D’Amore, “Compact electrothermal macromodeling of photovoltaic modules,” IEEE Trans. Circuits and Systems – II: Express Briefs, 56, 2, pp. 162-166, (2009).

[38] P. Maffezzoni, L. Codecasa, and D. D’Amore, “Modeling and simulation of a hybrid photovoltaic module equipped with a heat-recovery system,” IEEE Trans. Industrial Electr., 56, 11, pp. 4311-4318, (2009).

[39] K. Sayed, M. Abdel-Salam, M. Ahmed, and A. A. Ahmed, “Electro-thermal modeling of solar photovoltaic arrays,” in Proc. ASME Int. Mechanical Engineering Congress & Exposition (IMECE), (2011).

[40] K. Górecki, P. Górecki, and K. Paduch, “Modelling solar cells with thermal phenomena taken into account,” Journal of Physics: Conf. Series, 494, 012007, (2014).

[41] M. Usama Siddiqui, A. F. M. Arif, L. Kelley, and S. Dubowsky, “Three-dimensional thermal modeling of a photovoltaic module under varying conditions,” Solar Energy, 86, 9, pp. 2620-2631, (2012).

[42] A. D. Jones and C. P. Underwood, “A thermal model for photovoltaic systems,” Solar Energy, 70, 4, pp. 349-359, (2001).

[43] S. Armstrong and W. G. Hurley, “A thermal model for photovoltaic panels under varying atmospheric conditions,” Applied Thermal Engineering, 30, 11-12, pp. 1488-1495, (2010).

[44] W. Marańda and M. Piotrowicz, “Extraction of thermal model parameters for field-installed photovoltaic module,” in Proc. IEEE Int. Conf. MIcroELectronics (MIEL), pp. 153-156, (2010).

[45] I.-R. Caluianu and F. Băltăreţu, “Thermal modelling of a photovoltaic module under variable free convection conditions,” Applied Thermal Engineering, 33-34, pp. 86-91, (2012).

[46] Y. Lee and A. A. O. Tay, “Finite element thermal analysis of a solar photovoltaic module,” Energy Procedia, 15, pp. 413-420, (2012).

[47] V. d’Alessandro, F. Di Napoli, P. Guerriero, and S. Daliento, “A novel circuit model of PV cell for electrothermal simulations” in Proc. RPG Conference, 2014.

[48] L. Codecasa, V. d’Alessandro, A. Magnani, N. Rinaldi, and P. J. Zampardi, “FAst Novel Thermal Analysis Simulation Tool for Integrated Circuits (FANTASTIC),” in Proc. THERMINIC, 2014.

[49] V. d'Alessandro, A. Magnani, L. Codecasa, F. Di Napoli, P. Guerriero, and S. Daliento, "Dynamic Electrothermal Simulation of Photovoltaic Plants," in Proc. IEEE International Conference on Clean Electrical Power (ICCEP), 2015, pp 682-688.

[50] P. Bellezza Quater, F. Grimaccia, S. Leva, M. Mussetta, and M. Aghaei, “Light unmanned aerial vehicles (UAVs) for cooperative inspection of PV plants,” IEEE Journal of Photovoltaics, vol. 4, no. 4, pp. 1107-1113, 2014.

[51] L. Codecasa, V. d'Alessandro, A. Magnani, N. Rinaldi, and P. J. Zampardi, "FAst Novel Thermal Analysis Simulation Tool for Integrated Circuits (FANTASTIC)," in Proc. IEEE THERMINIC (2014).

[52] R. H. Winkler, "Thermal properties of high-power transistors," IEEE Trans. Electron Devices, ED-14, 5, pp. 260-263, (1967).

[53] J. Ding, X. Cheng, and T. Fu, "Analysis of series resistance and P–T characteristics of the solar cell," Vacuum, 77, 2, pp. 163-167, (2005).

[54] S. Banerjee and W. A. Anderson, "Temperature dependence of shunt resistance in photovoltaic devices," Appl. Phys. Letters, 49, 1, pp. 38-40, (1986).

[55] www.etsolar.com.ar/folletos/ET-M54050(50w).pdf.

[56] Comsol 3.5a, User's Manual, Comsol AB, 2008.

[57] S. Sharples and P. S. Charlesworth, "Full-scale measurements of wind-induced convective heat transfer from a roof-mounted flat plate solar collector," Solar Energy, vol. 62, no. 2, pp. 69-77, 1998.

[58] http://www.windfinder.com/

Chapter 4

4 High granularity power conversion

4.1 Proposed strategy

The distributed power conversion approach ensures the best performances in terms of MPPT efficiency (efficiency to track the global MPPT in all operating conditions), but the solutions presented in the PV market to realize this topology are expensive and exhibit considerable conversion power losses. A centralized conversion approach ensures the same performance of a distributed one, in terms of MPPT efficiency when the PV plant operates in uniform condition as illustrated in Fig 4.1, where a string made by three panels is considered. In this case the P-V curve of the string has a single maximum which is equal to the sum of the three MPPs of each panel, for this case the centralized approach ensures the same MPP achievable by the distributed approach. Fig 4.2 illustrates the characteristics of three panels in mismatch condition and the P-V of a string composed by these three modules. The distributed approach ensures that each panel operates in its MPP so the power at the input of the converter is the sum of the three MPPs of each panel. The centralized approach operates on the characteristic of the string thus the maximum input power achievable is the global MPP of the string which is lower than the value reached by the distributed conversion. Anyway, the losses could be greater in this case, due to the MPPT failure explained in the first chapter of this work.

The best trade-off between MPPT capabilities and switching power losses should join the advantages of the distributed approaches with the reduced losses of single stage topologies. Cascaded H bridge (CHB) multilevel converters, where each H-bridge is connected to a single PV source (the system H-bridge plus solar panel is hereafter referred to as "cell"), seem to be an attractive choice [1]-[12] (each H-

bridge is rated to low power thus its switching power devices exhibit low power dissipation).

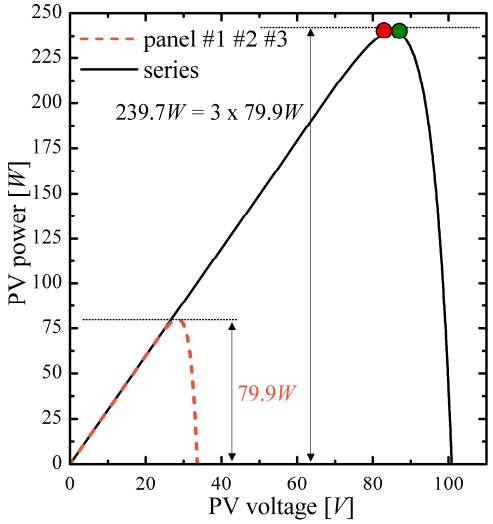

Fig 4.1 String of 3 panels under uniform condition: operating points in case of centralized approach (red circle) and distributed approach (green circle).

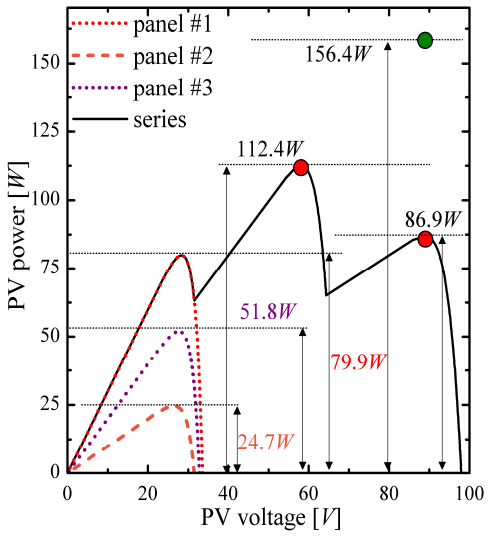

Fig 4.2 String of 3 panels under mismatch condition: operating points in case of centralized approach (red circles) and distributed approach (green circle).

The main advantages of this circuit topology are the following:

- a modular structure able to be adapted to different voltage and power levels thus allowing the sharing of voltage boosting among the cascade (i.e. series) of the H-bridge cells;
- a multilevel waveform expandable to a number of voltage steps depending on the number of used cells;
- the circuit topology permits to control separately the voltage of each dc-link, so providing a distributed MPPT.

The increase in the number of voltage levels in the inverter output waveform also allows to reduce the total harmonic distortion (THD), improving the quality of the output current with respect to conventional converters. As a consequence, the output filter requirements become weak in the compliance with the grid harmonics standards. A drawback is the more elaborate control strategy, since the topology is more complex with respect to the standard converters. In fact, different H-bridge cells share the same grid current, hence a unique grid current control loop must be implemented, moreover the N input voltage levels need to be controlled. As a consequence there are N+1 variables to be controlled, but the control action can be performed only through the N modulation indexes of the H-bridges. This implies critical instability issues, in particular in case of unbalanced conditions due to cells' different temperatures and solar radiations [6], thus the control method must assure a stable circuit operation.

In this scenario the CHB topology is proposed as a high granularity conversion approach which tries to overcome the drawbacks of the other high granularity solutions in the PV market.

This chapter deals with an innovative strategy to control the circuit first in single phase configuration and then in a three phase one. Differently from all other control strategies presented so far for this topology in PV applications, the proposed approach mixes the stair case modulation technique with Pulse Width Modulation (PWM) one. In the first modulation approach each solar panel can be either connected to the grid or bypassed, so that the output inverter voltage achieves only fixed values, while the PWM implies that each H-bridge operates at high frequency. In the proposed approach, only one H-bridge is in PWM mode while the others follow the stair case logic. The modulation state for each cell is determined by means of a special sorting algorithm which compares the errors between the actual value of the voltage measured across the input of each cell and the MPPT reference values. This modulation provides a strong reduction of the

dynamic power losses since only one cell switches at each step of the sorting algorithm while the others are connected or bypassed. The complexity of the proposed algorithm needs an FPGA implementation when the number of cells increases. A single phase prototype made by three cells was built and a wide set of testes was conducted in order to assess the robustness in uniform and mismatch operating conditions along with the dynamic system response.

4.2 CHB topology and control strategy for single phase operation

Fig 4.3 shows the circuit topology for a single phase PV CHB inverter.

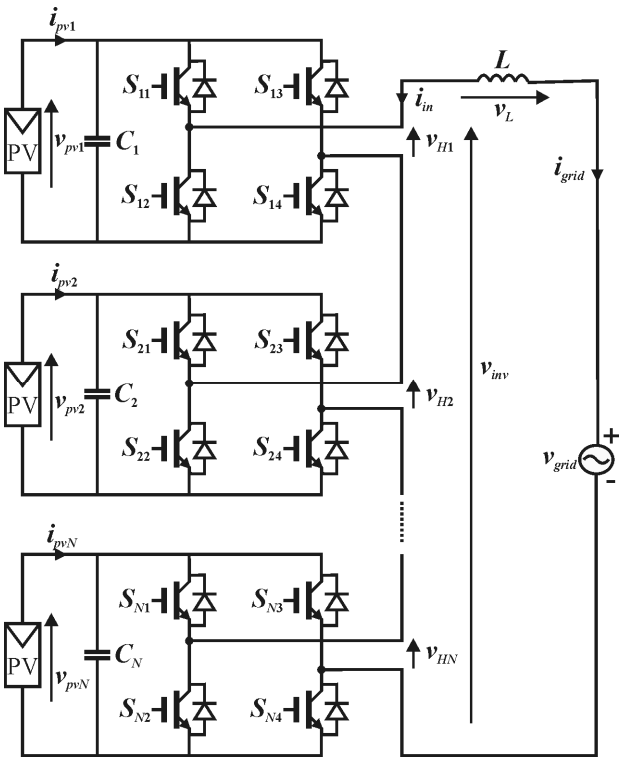

Fig 4.3 Single phase 2*N*+1 grid-tied PV CHB inverter.

In order to force active power from the dc sources (PV panels) into the grid the overall dc-link voltage needs to be higher than grid

voltage peak value. Therefore, the number N of cells and PV modules must be properly chosen in order to meet these requirements. In literature different modulation strategies for PV applications have been presented, the favourite one is PS-PWM (Phase Shifted Pulse Width Modulation), in [7] both PS-PWM and LS-PWM (Level Shifted PWM) are exploited. Another modulation approach is presented in [13] where PS-DPWM (Phase Shifted Discontinuous Pulse Width Modulation) is used to control a three phase grid-connected system, while in [14] a SHE (Selective Harmonic Elimination) is performed by using an ANN (Artificial Neural Network). PS-PWM and LS-PWM requires N different triangular carriers by considering a CHB made by N cells, these carriers are modified in phase (PS) or in the vertical position (LS) so leading to a complex modulator circuit. The operation as a distributed power converter requires that between the cells there is an unbalanced power distribution, since each cell has to stabilize the input PV source in the proper MPP, which in principle may not be the same for all cells. As a consequence those multicarrier modulation strategies need to be properly adapted to ensure correct operation of the structure also in case of power unbalance. In [7] an energy balance controller is used, where additionally rotating carrier approach is performed for LS-PWM in order to achieve desired cells' power balance. In [5] a voltage balancing strategy based on reactive power control is adopted, in [2] a power controller based on calculation of available power of each cell is performed, while in [4] and [13] a nonactive power control is proposed in order to meet nonactive power demand of a local load while realizing power factor correction and minimizing distribution losses. Instead, here it is proposed a different approach based on mixed staircase-PWM technique [15]-[17] performed by means of a sorting algorithm to determine which cell must be in PWM operation, while the others are in a fixed state in order to obtain the desired multilevel waveform. The proposed modulation is well suited for CHB topology with unequal dc sources and consequently unbalanced power distribution among the cells; moreover it provides reduced switching losses thus improving converter efficiency [18]. The sorting strategy is properly adapted to the PV application. For this reason, the choice of the cells' state is related to the need of charging or discharging a particular cell much more than the others according to the errors between the MPPT reference value and the actual voltage input level of each cell. In particular, the cell charging is achieved

bypassing the cell itself so resulting in direct connection to the PV panel which is the only source devoted to charge the power cell (e.g. the grid is not used to charge the dc-link capacitor of each cell since the power factor need to be equal to one).

In Fig 4.3 each PV generator is connected to a H-bridge inverter, while outputs (v_{Hi}) are connected in series to the grid in order to synthesize the desired ac output waveform:

$$v_{inv} = \sum_{i=1}^{N} v_{Hi} \quad (4.1)$$

Output voltage v_{Hi} (at the ac side) has three possible values depending on the state of the switches $S_{i,g}$ (i=1..*N*, g=1..4). Namely, $v_{Hi} = 0$ if either S_{i1} and S_{i3} or S_{i2} and S_{i4} are in the ON state; $v_{Hi} = +v_{pvi}$ when S_{i1} and S_{i4} are ON; $v_{Hi} = -v_{pvi}$ when S_{i2} and S_{i3} are ON. Switching states are reported in Tab 4.1.

state	S_{i1}	S_{i2}	S_{i3}	S_{i4}	v_{Hi}
0	on	off	on	off	0
0	off	on	off	on	0
+1	on	off	off	on	$+v_{pvi}$
-1	off	on	on	off	$-v_{pvi}$

Tab 4.1 Switching states.

In other terms, by assuming the switch states as binary signals (i.e. switch on corresponds to 1, while switch off corresponds to 0), the ac voltage v_{inv} can be written as follows:

$$v_{inv} = \sum_{i=1}^{N} v_{Hi} = \sum_{i=1}^{N} (S_{i1} - S_{i3}) v_{pvi} = \sum_{i=1}^{N} h_i v_{pvi} \quad (4.2)$$

where the modulation factor h_i can assume three possible values (+1, -1, 0). The proposed algorithm, differently from the multicarrier approaches, has only one modulation factor *h*, so that (4.2) can be written as

$$v_{inv} = \sum_{i=1}^{k-1} \pm(v_{pvi}) + h_k v_{pvk} \quad (4.3)$$

where k identifies, during each sorting cycle, the only cell driven in PWM mode. The remaining N-k cells do not appear because corresponding to h=0. The sign +/- into the sum depends on whether the corresponding h is kept to 1 or -1. From Fig 4.3 it can be noted that the states defined by h=+/-1 correspond to the discharging of the dc-link capacitors C_i, (namely the dc-link directly connected to the grid) while h=0 makes the capacitor to be charged because no power is delivered to the grid. Either the sign is + or - depends on whether is in the positive half cycle or in the negative half cycle respectively. In order to write the open loop state equations for the control problem, it is possible to replace h_i with a continuous switching function $\bar{h}_i$, for all cells, (even if one cell for sorting cycle is in PWM mode) bounded in the interval [-1, +1]; thus, current i_{in} injected into the grid can be related to the voltages across each cell

$$\begin{aligned} &\frac{di_{in}}{dt} = \frac{v_L}{L} = \frac{v_{grid} - v_{inv}}{L} = \\ &= \frac{v_{grid} - \sum_{i=1}^{N} \bar{h}_i v_{pvi}}{L} \qquad i = 1,..,N \quad (4.4) \\ &\frac{dv_{pvi}}{dt} = \frac{1}{C_i}(i_{pvi} + \bar{h}_i i_{in}) \end{aligned}$$

The adopted control strategy needs to accomplish the following tasks:

- independent control of each dc-link voltage in order to provide a distributed MPPT;
- transfer of the overall active power from PV generators to the grid;
- the output current i_{in} (see Fig 4.3) must be injected into the grid with low harmonic content at unity power factor;
- synthesis of a multilevel ac waveform (v_{inv}) at the output of the cascaded converter;
- stabilization of the converter operation even in the case of unbalanced conditions.

In order to meet the previous requirements a main inverter control is employed as described in Fig 4.4. The PI section provides the reference voltages v_{inv}^{ref} and it has standard features. The first PI regulates the overall dc-link voltage to the sum of the references (v_{pvi}^{ref}) given by the MPPTs, performed individually for each cell. The voltages measured across the dc-link capacitors are properly filtered (v_{pvi_f}) by using a 100 Hz band-stop digital filter in order to suppress the ac fluctuations, thus ensuring that the control operates with dc values as input data. The outputs of the filter are input signals for both the MPPT blocks (whose outputs are the reference voltages v_{pvi}^{ref}) and the sorting block which defines the errors $\Delta v_{pvi} = v_{pvi}^{ref} - v_{pvi\_f}$.

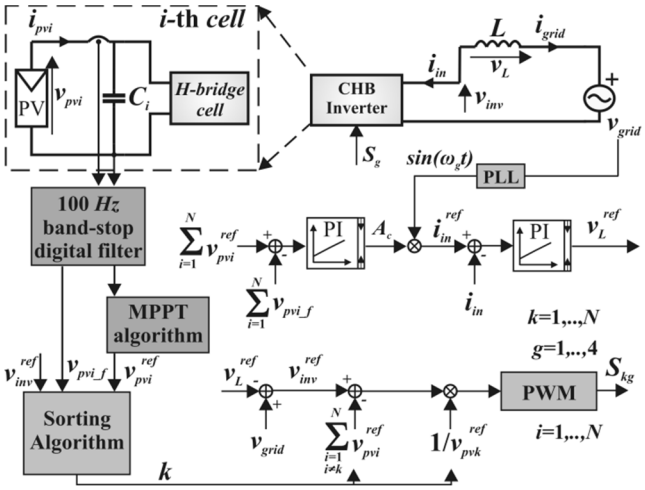

Fig 4.4 Block diagram of the whole control system.

At the output of the first PI controller there is the desired amplitude of the converter input current, which is related to the active power to be transferred to the grid in order to force the dc-link voltages to the reference values. This amplitude is then multiplied by a unity sine wave to derive the current reference. Since the output current (i.e. $i_{grid} = -i_{in}$) must be synchronized with the grid voltage, a PLL (Phase Locked Loop) circuit provides the proper sinusoidal waveform, in phase and with the same frequency of the grid voltage.

The second PI calculates the voltage reference across the inductor which provides the desired shape of the current to be injected into the grid. This value must be add to the grid voltage in order to

obtain the ac side inverter voltage reference output v_{inv}^{ref} . According to (4.3) v_{inv} can be synthesized by adding up the output voltages v_{Hi} of *k-1* cells (by permanently connecting them for an entire control sorting cycle) plus one cell in PWM mode, while the others are kept in the zero output voltage state.

The sorting algorithm flowchart is shown in Fig 4.5.

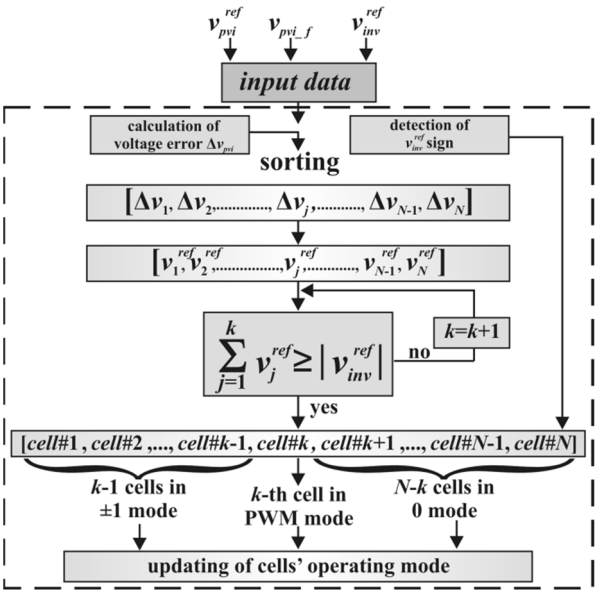

Fig 4.5 Flowchart of the sorting algorithm.

It is executed with period T_{sort}; at each sampling time the voltage error Δv_{pvi} between the MPPT reference (v_{pvi}^{ref}) and the actual filtered dc-link voltage (v_{pvi_f}), is mapped for all cells in ascending order ([Δv_1,.., Δv_j ,.., Δv_N]). The last cell in the sorted vector has the greatest positive error which means it has to charge the dc-link capacitor, because the actual value is lower than the MPPT reference. While the first cell has the lowest negative error, it means that the measured voltage is greater than its MPPT reference so the dc-link capacitor must be discharged much more than the other cells. The algorithm also defines a second vector composed by only v_{pvi}^{ref} , sorted according to the corresponding error ([v_1^{ref} ,.., v_j^{ref} ,.., v_N^{ref}]). Through an iterative procedure, involving the reference inverter output voltage (v_{inv}^{ref}), the algorithm identifies the index *k* which defines the *k-1* cells

of the sorted vector being directly connected to the grid (±1 mode), while the *k*-th cell is forced to operate in PWM and the others are bypassed (0 mode). In this way the sorting algorithm allows uneven power generation from the cells, thus performing the distributed MPPT in mismatch conditions.

Fig 4.6 shows an example with N=3. Index j represents the ordering index of the sorted vector, while index i indicates the cell's position in the physical circuit as reported in Fig 4.3.

The sorting algorithm is executed at every T_{sort} of about 0.4 ms. The dc-link filtered voltages (v_{pvi_f}, i=1,2,3), the MPPT references (v_{pvi}^{ref}, i=1,2,3), and the instantaneous value of v_{inv}^{ref}, are the input variables of the iterative procedure. The sign of v_{inv}^{ref} allows to determine if the *k-1* cells directly connected to the grid have to fix a positive or negative value of v_{pvi} (e.g., in the case of Fig 4.6 the positive half-cycle is considered).

Than the voltage errors ($\Delta v_{pvi} = v_{pvi}^{ref} - v_{pvi\_f}$, i=1,2,3) at each dc-link are calculated, thus obtaining a first not ordered vector [Δv_{pv1}, Δv_{pv2}, Δv_{pv3}]. This vector is sorted in ascending order [Δv_1, Δv_2, Δv_3].

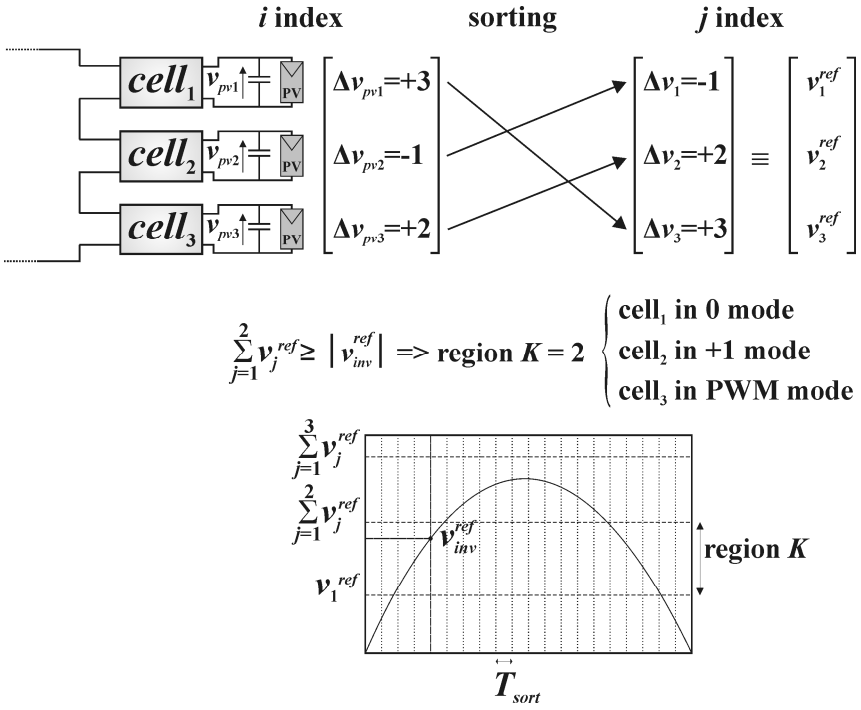

Fig 4.6 Example of a single sorting control cycle with N=3.

In Fig 4.6, the first element Δv_1 of the sorted vector corresponds to the cell with the lowest negative voltage error (in this example, $cell_2$), while the last element Δv_3 corresponds to the cell with the highest positive voltage error (in this example, $cell_1$).

Starting from the sorted vector of the voltage errors, a sorted vector of the MPPT voltage references is obtained $v_1^{ref}, v_2^{ref}, v_3^{ref}$, where v_1^{ref} corresponds to $cell_2$ (i.e. is equal to v_{pv2}^{ref}), v_2^{ref} corresponds to $cell_3$ (i.e. is equal to v_{pv3}^{ref}) and v_3^{ref} corresponds to $cell_1$ (i.e. is equal to v_{pv1}^{ref}). Now, the identification of the k index can be performed by an adaptive division of v_{inv}^{ref} in three regions through an iterative procedure: when the sum of the sorted dc-link MPPT reference voltages (i.e. v_j^{ref} j=1,2,3), starting from the first position of the vector, is greater than the instantaneous absolute value of v_{inv}^{ref} (i.e. $\sum_{j=1}^{k} v_j^{ref} \geq \left| v_{inv}^{ref} \right|$), then the index k is identified. As reported in Fig 4.6, $\sum_{j=1}^{2} v_j^{ref} \geq \left| v_{inv}^{ref} \right|$ thus the index k = 2 and the cell #2 (k-th cell) of the sorted vector, corresponding to $cell_3$ in the physical circuit, will be in PWM mode.

While the first k-1 = 1 cells will be in +1 mode (namely in this example it is $cell_2$ corresponding to first position of the sorted vector) and the last N-k = 1 cells will be in 0 mode (in this example it is $cell_1$ corresponding to last position of the sorted vector). It is worth noting that purpose of the proposed control is not a voltage balancing among cells, but stable system operation under unbalanced conditions, which is mandatory in order to perform a distributed MPPT. The mixed modulation method with unequal dc sources represents a novelty with respect to [15]-[17].

The MPPT adopted for each cell (see Fig 4.7) is a traditional perturb and observe (P&O) MPPT method, properly adapted to the particular application under investigation. The algorithm is executed periodically (T_{MPPT} =0.2 s) and individually for each cell. Each MPPT block receives as input the filtered quantities v_{pvi_f} and i_{pvi_f} and multiplies both values in order to obtain PV power at a given MPPT iteration step, used to determine the next voltage reference value. The iteration period T_{MPPT} should be large enough to ensure that voltage control loop reaches the imposed voltage reference at every iteration step. In the following experiments, the voltage reference step is fixed to 0.5 V, while the MPPT time period is equal to 0.2 s. The first 0.1 s

are required to drive the system in steady state, the other 0.1 s are employed to evaluate a mean of the input variables.

The MPPT algorithm performs other two controls, in order to allow a suitable synthesis of the desired inverter voltage waveform (e.g., a minimum voltage at each dc-link is needed to cover the grid peak voltage plus the voltage drop across the inductor, in order to have an active power flow from the PV modules to the grid), while assuring a stable circuit operation (i.e., the performed voltage range must not include the flat region of the I-V curve [7]). The first control establishes a minimum value v_{pv_min} of the tracking voltage range. This latter value is properly chosen by taking in mind the temperature and irradiance range as well as the nominal ac fluctuations at the dc-link capacitor.

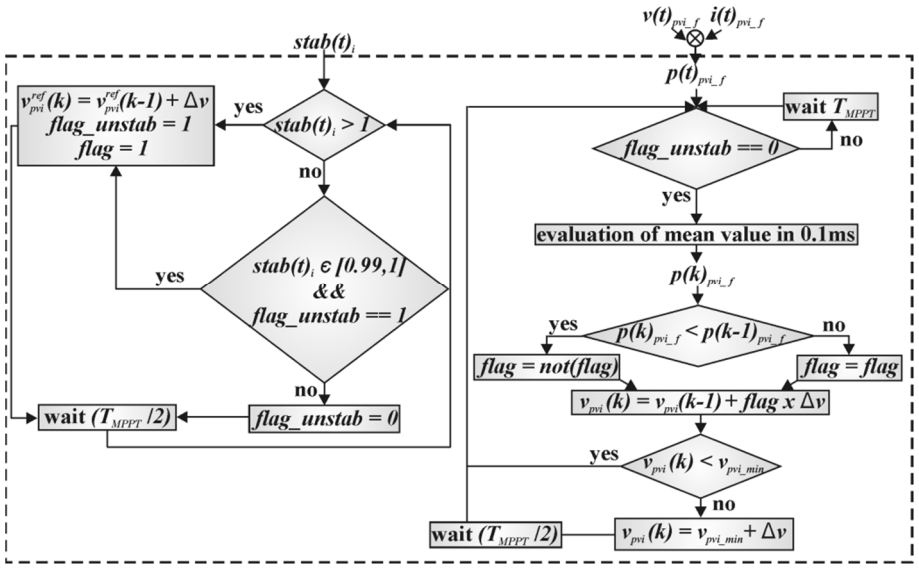

Fig 4.7 Block diagram of the MPPT.

The second control is required in order to avoid instability issues related with operation in mismatch conditions. Indeed, if the tracking brings some cells out of linearity (this occurrence can be monitored by means of the modulation index [12] which tends to be greater than 1) the algorithm stops to pursuit the MPP for the instable cells and increases the operating voltage until the modulation index recovers a less than one suitable value. The modulation index s_j of the j-th cell can be estimated according to this relation

$$s_j = \frac{i_{pvj\_f}\hat{V}_{grid}}{\sum_{i=1}^{N} v_{pvi\_f} i_{pvi\_f}} \quad (4.5)$$

The block diagram of the proposed MPPT is shown in Fig 4.7, as can been seen there are two loops which are executed at different frequencies, the MPPT iteration is at lower frequency with respect to the stability control loop which is executed at double frequency. This choice is linked to the need to regain quickly stability operation when instability conditions are detected.

4.3 CHB control strategy for three phase operations

The proposed control strategy is extended to the three phase case; a further challenge is to guarantee the equilibrium among the line currents even when the PV subfields, connected to each phase, provide unbalanced powers (for instance when partial shading occurs among subfields linked to different inverter legs). Fig 4.8 shows the three phase topology of the multilevel CHB inverter. The structure of each leg is a single phase CHB and the three legs are connected in a star configuration.

For each leg the sorting algorithm is individually performed as long as an individual MPPT algorithm is executed for each cell. The innovative modulation strategy continues to operate as previous illustrated in each leg in order to synthesize $v_{inv,p}$ with p index identifying the phase. All equations for the single phase control are still correct, taking into account the p index for each phase.

The ac voltage $v_{inv,p}$ at the output of the p-th leg can be written as follows:

$$v_{inv,p} = \sum_{i=1}^{N} v_{Hi,p} = \sum_{i=1}^{N} (S_{i1,p} - S_{i3,p}) v_{pvi,p} = \sum_{i=1}^{N} h_{i,p} v_{pvi,p} \quad (4.6)$$

The modulation strategy adopted implies only one set of modulation factors h for each phase, so the equation (4.3) becomes:

$$v_{inv,p} = \sum_{i=1}^{k-1} \pm(v_{pvi,p}) + h_{k,p} v_{pvk} \quad (4.7)$$

where k continues to identify, during each control cycle, the unique cell driven in PWM mode in the single phase. So each phase has only one cell in PWM mode during each iteration cycle of the sorting algorithm.

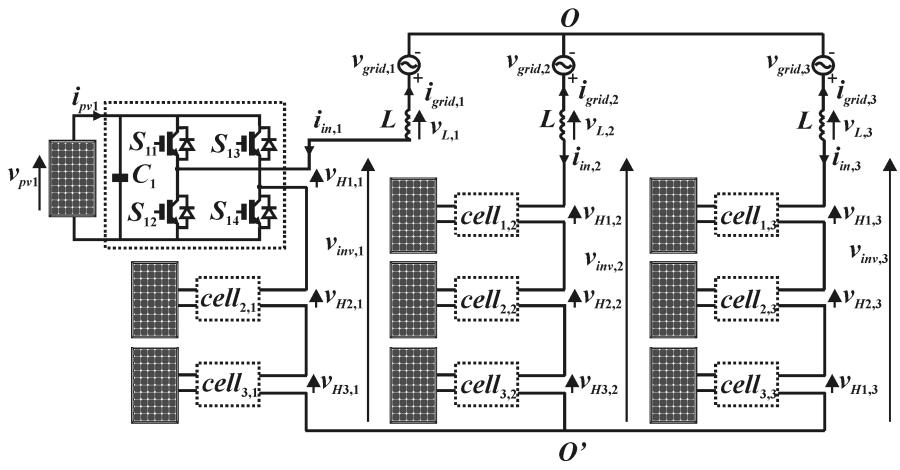

Fig 4.8 Three phase 7 levels grid-tied PV CHB multilevel inverter.

The PI control loop is different with respect to the single phase case, and it is depicted in Fig 4.9. It provides the reference voltages $v_{inv,p}^{ref}$ for the three phase, the outer loop adjusts, for each phase, the sum of the dc-link voltages $v_{pv,i}$ in accordance with the sum of the references $v_{pvi,p}^{ref}$. As can be seen the first PI evaluate the reference currents I_p^{ref} for each phase, thus the reference active power P_p^{ref}.

In the inner loop a multivariable PI controller [19] regulates both the direct and the reactive grid currents. To this end the three reference powers given by the first PI are summed in order to get the direct current reference i_d^{ref}, while the reactive current reference i_q^{ref} is set to zero in order to achieve unity power factor.

Currents i_d and i_q are achieved by converting the measured grid currents (*abc* coordinates) into *dq* coordinates. The outputs of the multivariable PI are the inverter reference voltages in *dq* coordinates

which are then converted to the three phase reference voltages (*abc* coordinates); the synchronization with the grid of the *dq* transformation is performed by means of the Phase Locked Loop (PLL) circuit.

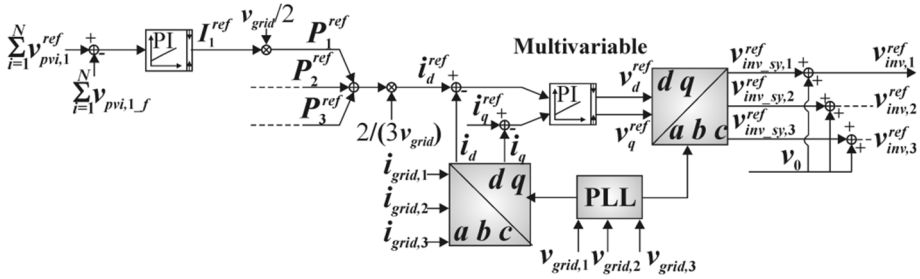

Fig 4.9 PI control loop for the three phase CHB.

It is important to note that the independent MPP tracking performed for each cell may generate different input powers for each leg, thus inherently leading to unbalanced grid currents. In order to overcome this undesired drawback a proper homopolar zero-sequence voltage component, v_0, is added. Indeed, according to [20], for a given power unbalances among the phases, defined as

$$\Delta P_p = P_p^{ref} - \sum_{h=1}^{3} \frac{P_p^{ref}}{3} \qquad p = 1,2 \quad (4.8)$$

v_0 has to deliver the amount of unbalance between the legs. The multivariable PI generates three reference voltages symmetric and balanced ($\hat{v}_{inv\_sy,p}^{ref}$) which deliver the power P_p^{ref}, while the homopolar voltage allows to move the inverter neutral point so as to have unbalanced inverter voltages at the output of each legs. The homopolar component ensures that the three output currents continue to be balanced even if the power delivered by each leg is different. The magnitude and phase angle of the homopolar component are determined considering that the inverter output currents have only a direct sequence while the output voltage of each leg can be written in terms of a direct sequence plus a zero sequence. Taking into account only the first harmonic component of these voltages and currents, the active power delivered by each leg can be written

$$P_k = \frac{1}{2}\hat{v}^{ref}_{inv\_sy,p}\hat{i}^{ref}_{d,p}\cos\ \varphi + \frac{1}{2}\hat{v}^{ref}_{0}\hat{i}^{ref}_{d,p}\cos\left(\frac{2\pi(p-1)}{6} - \varphi_0\right) \qquad p = 1,2 \quad (4.9)$$

where φ is the angle between the grid voltage direct sequence ($v_{grid,1}$ is considered with phase angle equal to zero) and the inverter current direct sequence, while φ_0 is the angle between the homopolar vector and the grid voltage direct sequence. The active power of each leg is sum of two components, the first is equal to P_p^{ref} of the equation (4.8) while the second term depending on the homopolar component which has to deliver the unbalance power ΔP_p. So the zero sequence magnitude and phase angle can be found solving these equations

$$\Delta P_p = \frac{1}{2}\hat{v}^{ref}_{0}\hat{i}^{ref}_{d,p}\cos\left(\frac{2\pi(p-1)}{6} - \varphi_0\right) \qquad p = 1,2 \quad (4.10)$$

which provides this solution

$$\begin{cases} \hat{v}_0 = \dfrac{4}{\sqrt{3}i_d^{ref}}\sqrt{\Delta P_1^2 + \Delta P_1\Delta P_2 + \Delta P_2^2} \\ \varphi_0 = \arctan\left[\dfrac{2}{\sqrt{3}}\left(\dfrac{\Delta P_2}{\Delta P_1} + \dfrac{1}{2}\right)\right] \end{cases} \quad (4.11)$$

The reference voltages provided by the PI loop are synthesized according to (4.7).

4.4 Numerical analysis

The operation of the proposed topology and the control strategy described in the previous paragraphs were analyzed by exploiting the Matlab/Simulink integrated with XSG (Xilinx System Generator). In the following only three phase simulations of the system are presented; the simulated circuit was a three phase system with three solar panels connected to each phase, each of them feeding a devised H-bridge. The PV generators analyzed in this work were described in simulation by means of a physical model based on a

generalized form of the five parameters (i_{ph}, I_{sat}, n, R_s, R_{sh}) single diode model. The current source i_{ph} accounts for the photogenerated current; the reverse saturation current I_{sat} and the ideality factor n account for the dark I-V characteristic; R_s and R_{sh} are the series and shunt resistance, respectively, accounting for parasitic effects.

Based on the single cell model, the I-V characteristic of a string, made up of n_2 PV modules, each of them composed of n_1 solar cells, is described by this simplified model (a cell level model of the panel is not taken into account):

$$i_{pv} = i_{ph} - I_{sat}\left[\exp\left(\frac{v_{pv} + n_1 n_2 R_s i_{pv}}{n_1 n_2 n V_T}\right) - 1\right] - \left(\frac{v_{pv} + n_1 n_2 R_s i_{pv}}{n_1 n_2 R_{sh}}\right) \quad (4.12)$$

where v_{pv} is the voltage across an entire string; V_T is the thermal voltage, R_s, R_{sh}, i_{ph}, I_{sat} and n are the five parameters of the single diode model. This equation assumes that all the cells have the same irradiance condition and equal parameters. In order to properly estimate the behavior of the PV generator by means of this model, an accurate calibration of its parameters is required. This procedure involves measurements of the I-V characteristic during normal operating conditions. Required data were obtained through a custom PV I-V tracer which allows in-situ measurements of the I-V curves for series connected solar panels. Model parameters describing solar panel exploited for the testes ([21]) are evaluated by means of fitting procedure and they are summarized in Tab 4.2, while Fig 4.10 shows the comparison between the measured I-V curve and the corresponding curve given by (4.12).

Parameter	**Value**
i_{ph}	3.22 *A*
I_{sat}	1.30e-7 *A*
n	1.06
R_s	2.50e-2 Ω
R_{sh}	100 Ω
n_1	72
n_2	1

Tab 4.2 Values adopted for the PV model parameters.

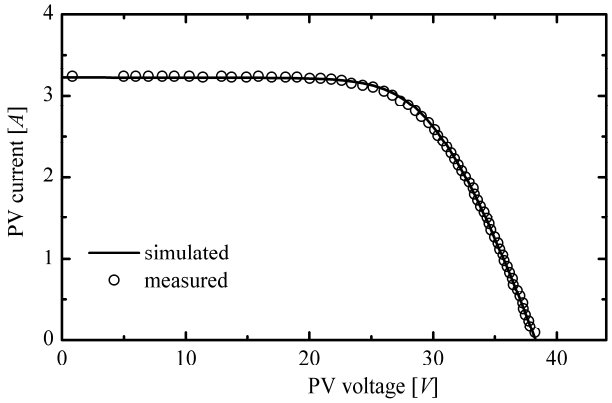

Fig 4.10 Comparison between measured I-V characteristic and simulated one through the model properly calibrated.

The simulation was built by exploiting both specially suited elemental blocks taken from the Xilinx library and custom, homemade, Verilog modules. The main advantage of this approach is that the control code could be directly implemented on a Xilinx FPGA platform; moreover it allowed very realistic simulations because the actual behavior of the hardware implementation on FPGA of the control code was emulated. The circuit parameters chosen for the simulation accomplish with the experimental set-up: dc-link capacitance $C=C_{i,p}$=4.6 mF (i=1,2,3; p=1,2,3); line inductance L=5 mH; grid peak voltage of 66 V (the grid connection was made with an auto-transformer). The capability of tracking the MPP of individual solar panels along with the quality of the current injected into the grid in terms of total harmonic distortion (THT) and power factor (PF) were monitored in three operating conditions:

- uniform illumination over all solar panels;
- not uniform illumination;
- dynamic illumination changing;

The first set of results is given in Fig 4.11, Fig 4.12, Fig 4.13.

The curves shown in Fig 4.11a, Fig 4.11b, and Fig 4.11c, refer, respectively, to the three legs of the circuit. Since uniform illumination was considered all P-V curves coincide each other; thus, for example, the P-V curves of the three solar panels connected to the first leg (Fig 4.11a) are represented by a unique curve.

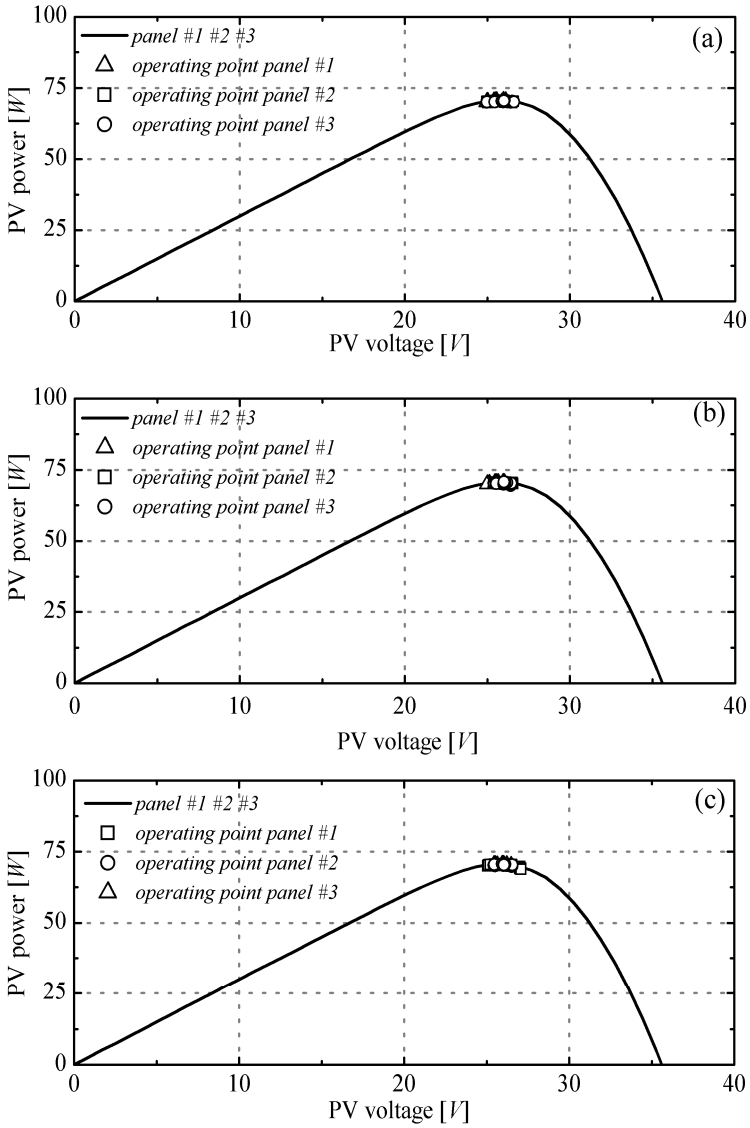

Fig 4.11 Uniform condition. Operating point positions corresponding to panel #1, panel #2 and panel #3 superposed on the individual P-V curves in phase 1 (a), phase 2 (b) and phase 3 (c).

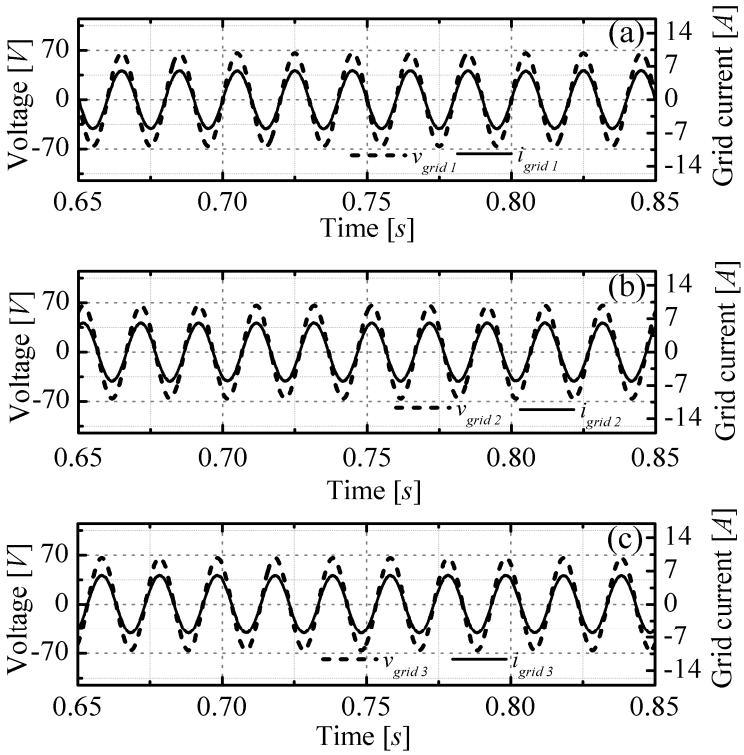

Fig 4.12 Uniform condition. Time behavior of the output currents compared to the grid voltages related to phase 1 (a), phase 2 (b) and phase 3 (c).

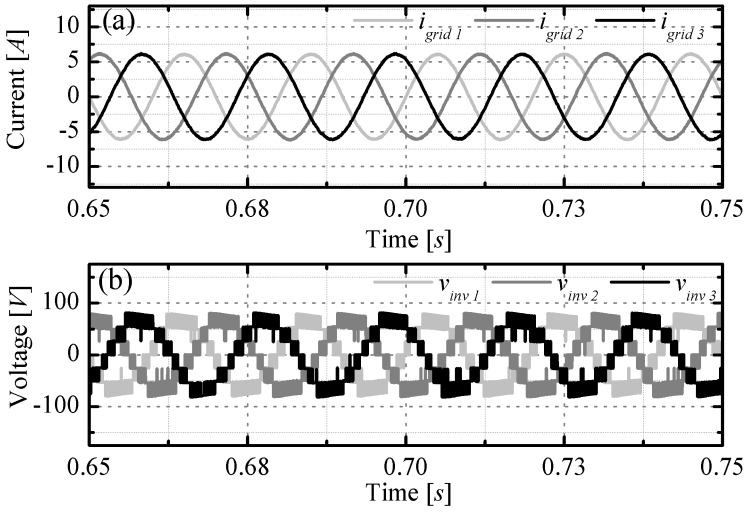

Fig 4.13 Uniform condition. Time behavior of the grid currents (a) and of the modulated voltages (b).

The maximum power points of the solar panels were independently tracked; therefore, the operating points actually assumed by each solar panel are shown by means of different symbols (squares, circles, triangles). As can be seen, all solar panels operate very close to their respective MPP with small oscillations ascribable to the limit cycle of the P&O tracking algorithm.

Fig 4.12 shows the three grid currents, superposed to the respective grid voltages and reveals that the power factor is unity.

Fig 4.13, shows the phase relation among the three currents (Fig 4.13a) and the modulated seven well spaced discrete levels voltage waveforms produced by the sorting algorithm (Fig 4.13b). The three voltages are symmetric and balanced so in this case (uniform illumination) the homopolar component v_0 (see (4.11)) is equal to zero. The frequency of the sorting algorithm was f=2.5 kHz.

The results in case of mismatch conditions are reported in Fig 4.14, Fig 4.15 and Fig 4.16.

The irradiance values for the nine panels in this experiment are reported in Tab 4.3, so that the power delivered by each leg is different each other. From Fig 4.14 it can be observed that, also in this case, all solar panels operate at their respective MPP. The control system guarantees balanced grid currents even if supplied powers on the three legs were different each other. The consequence of power unbalance is that the control action synthesizes unbalanced outputs $v_{inv,p}$ by adding the homopolar voltage component v_0 in order to ensure the equilibrium of the three grid currents. The effectiveness of this strategy is clearly visible in Fig 4.15, showing the superposition of the grid currents with the grid voltages, and Fig 4.16 showing the phase relation among the grid currents and the inverter output voltage waveforms. In particular, from Fig 4.16b the three inverter output voltages are no more balanced while assuring balanced currents. The last experiment was performed by linearly varying, from 625 W/m^2 to 375 W/m^2, the irradiance impinging on the first solar panel of the first leg, in a time interval starting at 0.4 s and ending at 0.8 s, so that the MPP of that panel changed from 75 W to 45 W.

Fig 4.17 shows that the MPP of the shaded panel is correctly tracked during irradiance variation; at the same time, the power factor is unity in all three legs (Fig 4.18). As evidenced in Fig 4.19 the three grid currents are well balanced (Fig 4.19a), while the phase relation among the voltages (Fig 4.19b) changes during time.

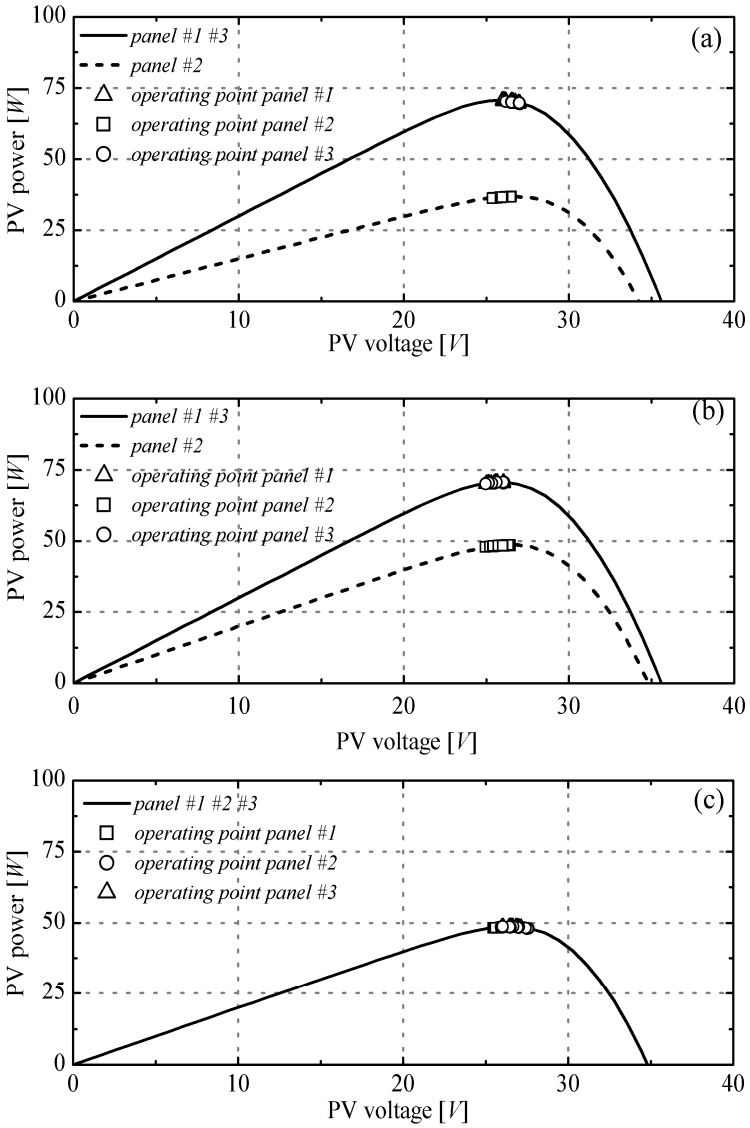

Fig 4.14 Mismatch condition. Operating point positions corresponding to panel #1, panel #2 and panel #3 superposed on the individual P-V curves in phase 1 (a), phase 2 (b) and phase 3 (c).

phase	**1**	**2**	**3**
Cell 1	625 W/m^2	625 W/m^2	417 W/m^2
Cell 2	313 W/m^2	417 W/m^2	417 W/m^2
Cell 3	625 W/m^2	625 W/m^2	417 W/m^2

Tab 4.3 PV panel irradiance values for the simulation in mismatch condition.

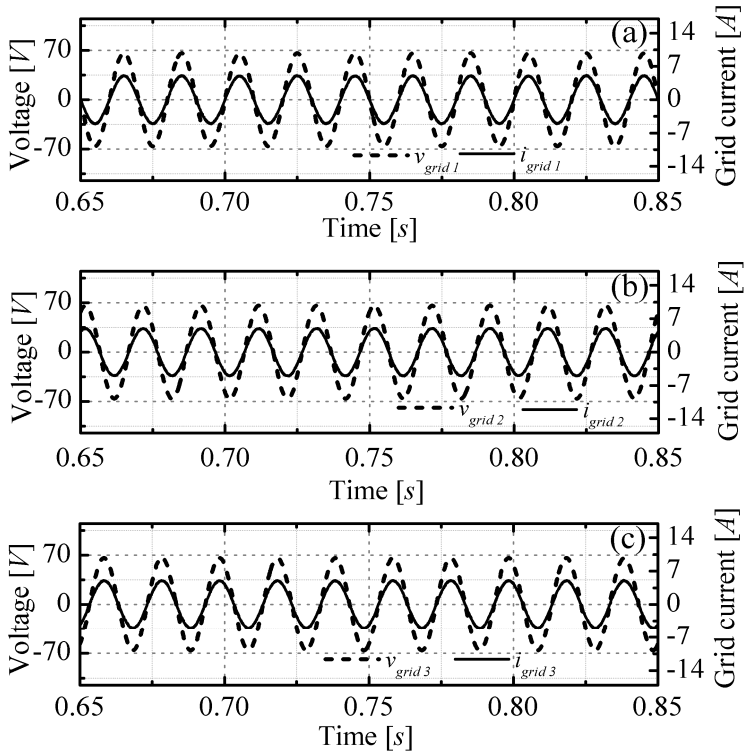

Fig 4.15 Mismatch condition. Time behavior of the output currents compared to the grid voltages related to phase 1 (a), phase 2 (b) and phase 3 (c).

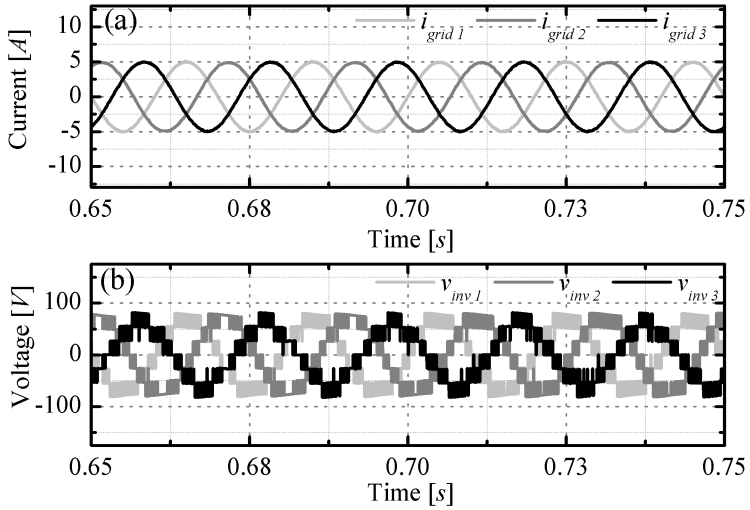

Fig 4.16 Mismatch condition.Time behavior of the grid currents (a) and of the modulated voltages (b).

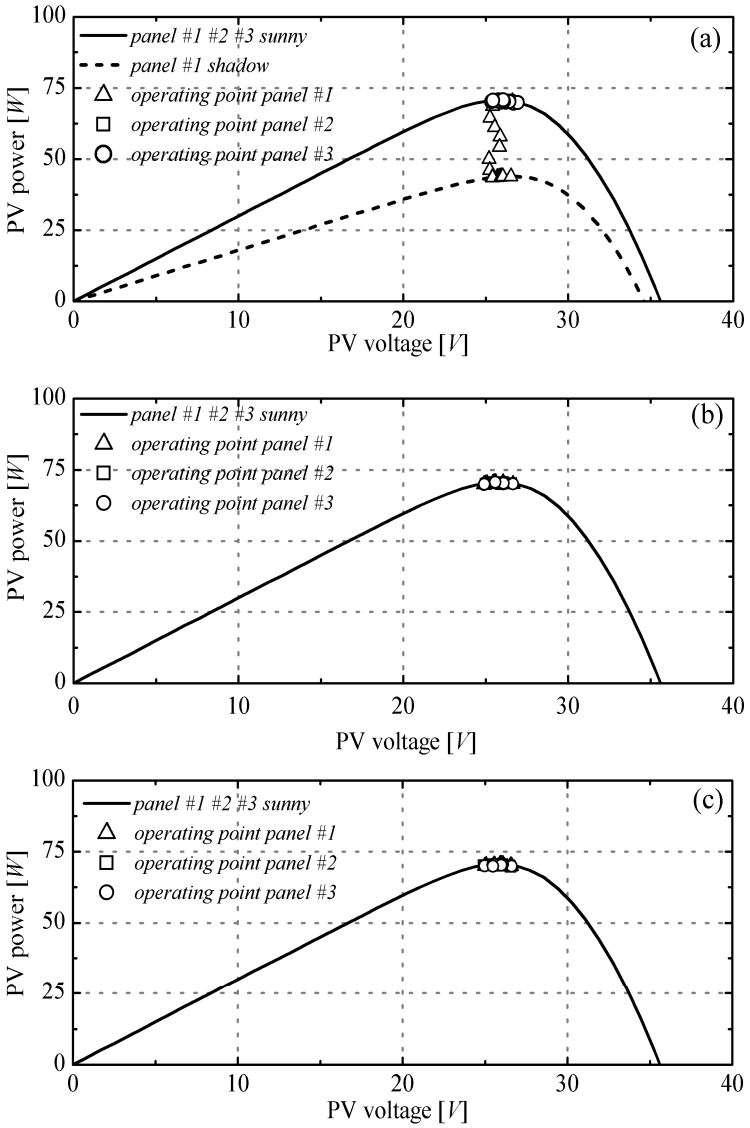

Fig 4.17 Sudden change. Operating point positions corresponding to panel #1, panel #2 and panel #3 is superposed on the individual P-V curves in phase 1 (a), phase 2 (b) and phase 3 (c). In particular in (a) the P-V curve of the panel #1 in shaded condition is also shown.

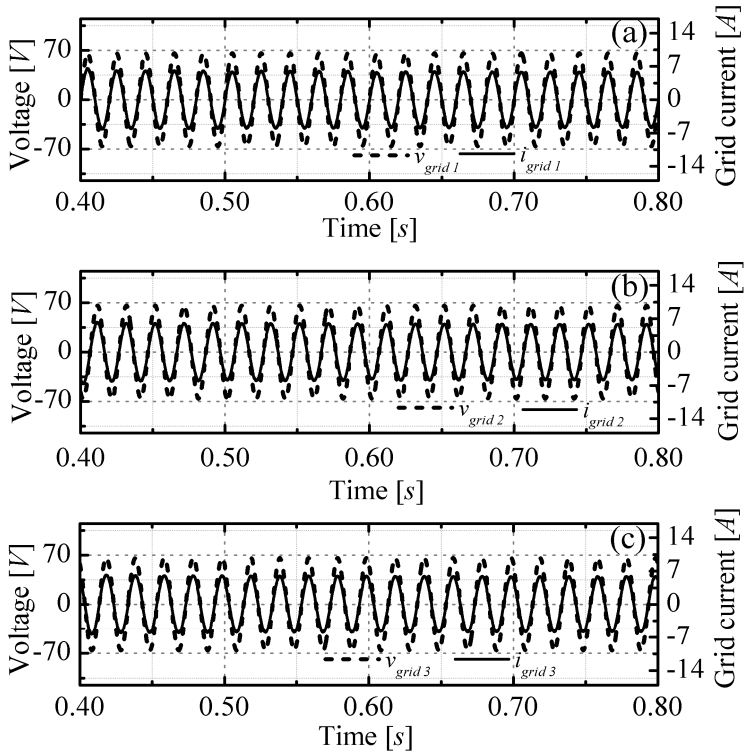

Fig 4.18 Sudden change. Time behavior of the output currents compared to the grid voltages related to phase 1 (a), phase 2 (b) and phase 3 (c).

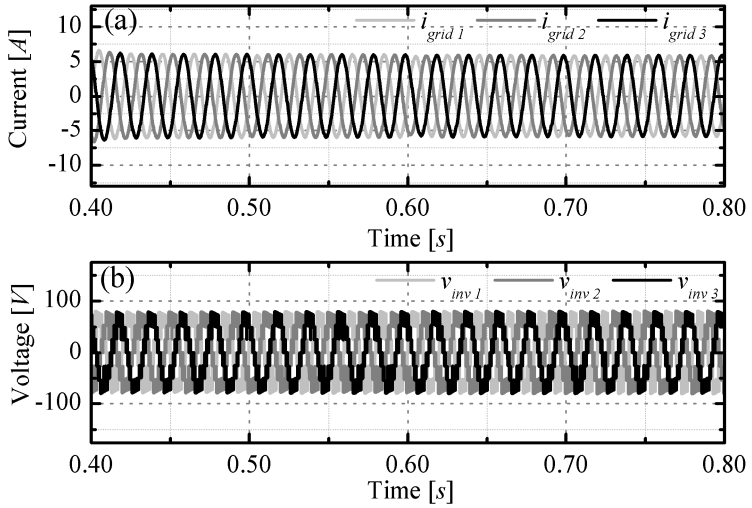

Fig 4.19 Sudden change. Time behavior of the grid currents (a) and of the modulated voltages (b).

4.5 Experimental setup and results

A laboratory prototype of a single phase grid-tied PV CHB multilevel inverter has been built, in order to experimentally validate the proposed circuit design and control approach. It consists of three H-bridges connected in series. Each cell includes one PV module, thus the available total dc-link voltage is lower than the peak grid voltage (i.e. 230 V_{RMS}). For this reason, an auto-transformer has been interposed between the inverter output and the grid with the aim of meeting the grid voltage level.

The test has been conducted by using a real-time hardware platform (dSpace ds1006) equipped with a FPGA Xilinx Virtex-5 (see Fig 4.20).

The measurement and control sections are mainly implemented on the FPGA by means of IP blocks from the Xilinx library and of Verilog custom modules in order to obtain fully dedicated digital circuits adapted to the proposed algorithm. The designed power cell consists of four IGBT IRGB4056DPbF with a breakdown voltage of 600 V and a continuous collector current of 12 A at 100°C. As can be noted the devices are oversized with respect to the voltage adopted for the test, thus the structure exhibits a low conversion efficiency, but the aim of the prototype is to test the MPPT efficiency and the quality of the current injected into the grid. The dc-link capacitance is 4.6 mF while the inductance of line filter inductor is L=5 mH. Each cell is equipped with a resistive divider at the dc-link in order to generate the proper voltage level to put in input to a 12-bit SAR A/D converter (ADS7816), whose digital output is sent to the dSpace platform with a maximum throughput rate of 200 kHz. The three cells are inserted in a back-plane (see Fig 4.20) equipped with a mux and demux with the same select lines. The demux input is a signal which enables the voltage measurement of a particular cell, based on the selection signals, those also address the corresponding output of the mux, whose inputs are the 12-bit serial data (i.e. digital version of dc-link voltage) of each cell. The transformer secondary side exhibits a voltage amplitude of about 43 V_{RMS} and a frequency of 50 Hz in agreement with the available PV voltage levels.

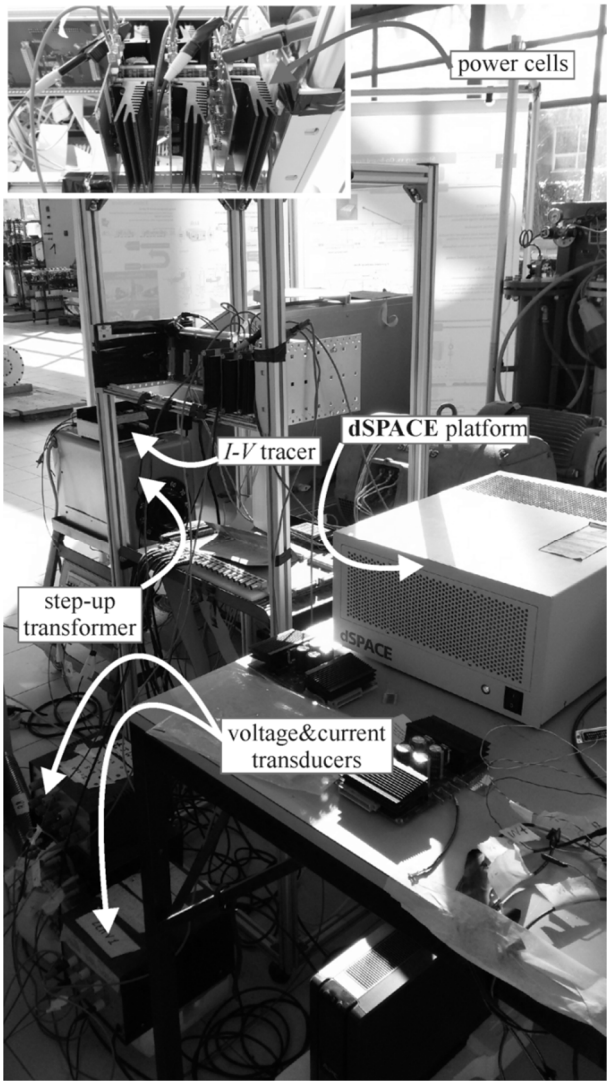

Fig 4.20 Laboratory prototype of a single phase PV CHB multilevel inverter made by three H-bridge cells.

The measurement process of all dc-link voltages is performed each T_0=0.1 ms. A custom Verilog module properly synchronizes the reading process so that it is completed at the end of time T_0 and the read data are available in a bank of registers until the next reading cycle starts.

The duration of the reading period T_0=0.1 ms accomplishes with the need to have $T_0 < T_{sort}$. The sorting algorithm is executed at

every T_{sort} = 0.4 ms. The custom Verilog MPPT block performs the algorithm, described in Fig 4.7, every T_{MPPT} = 200 ms.

The measured PV voltages and currents are filtered before they were sent to the sorting block and also to the MPPT block. The digital filter (100 Hz band-stop) is obtained by using a delay line (a chain of registers properly synchronized in order to perform the desired delay). Moreover, the dead-time between the gate signals of the switching devices of the same H-bridge cell leg is realized by a custom Verilog module on the FPGA.

A wide experimental campaign has been performed in order to verify the effectiveness of the proposed circuit and control design. In the test setup, three commercial PV panels [21] installed on the roof of the Department of Electrical Engineering and Information Technologies in Naples have been used. The instantaneous behavior of the PV panel in terms of I-V characteristic is monitored through the I-V tracer, previous exploited for evaluation of the parameters of the PV model (4.12). In normal operating conditions ("sunny" case), all panels have been kept under the same irradiance value (about 830 W/m^2), while in the partial shading test conditions, panel #2 and panel #3 have been subjected to a partial shadowing obtained by superposing a plastic optical filter on a small part of the three sub-panels, thus reducing the available irradiance down to about 690 W/m^2 and 580 W/m^2. The latter case covers a wide range of architectural shading events (e.g. poles, chimneys, TV antennas, etc.) often affecting small/domestic PV plants.

Fig 4.21 reports the steady state behavior of voltage v_{pvi}, its filtered value v_{pvi_f} and the MPPT voltage reference for the three panels. The input voltage v_{pvi} exhibits the inherent 100 Hz ac fluctuation of a DC-AC conversion, while its filtered version v_{pvi_f} does not reveal it. Moreover, v_{pvi} achieves the desired reference value in every MPPT iteration, thus confirming that the MPPT time step has been properly chosen with regard to the circuit dynamics. The positions of the operating points of the three panels are shown in Fig 4.22, superposed on the I-V curves (Fig 4.22a) and the related P-V curves (Fig 4.22b). All panels reach the desired maximum point, so leading to an overall static MPPT efficiency of 99.5%. Fig 4.23 depicts the modulated waveform v_{inv}, where the 7 levels are correctly synthesized, and the grid voltage v_{grid}. Moreover, the time behavior of the grid current i_{grid} is shown in order to highlight that its shape does not exhibit distortions and its PF is almost equal to one. The THD

value is properly calculated by taking into account the first 40 harmonics. It is of about 1.50%, thus resulting in agreement with the standard requirements for grid-tied application.

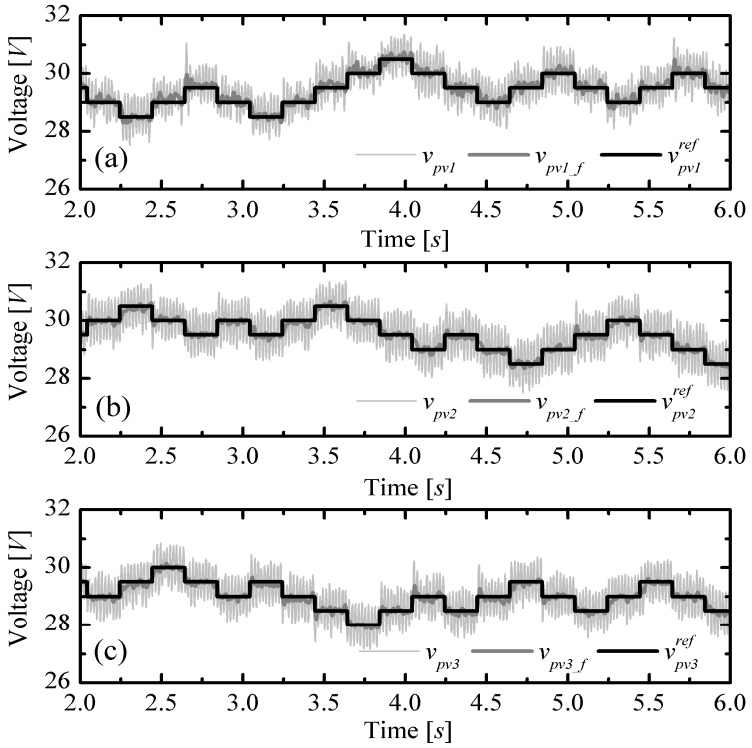

Fig 4.21 PV voltage reference time behavior compared to the measured PV voltage and the filtered one for the panel #1 (a), the panel #2 (b), and the panel #3 (c), respectively.

The case of partial shading conditions is reported in Fig 4.24. The position of the operating points of each cell is superposed to the I-V curves (Fig 4.24a) and the related P-V curves (Fig 4.24b). As in the case of uniform condition, each panel achieves its corresponding MPP, as a consequence each cell operates at different power levels but the inverter performances are not affecting by this operating condition. The obtained MPPT efficiency is close to 99%. This experimental result confirms the validity of the proposed control strategy which is able to obtain a distributed MPPT, guaranteeing a stable circuit operation.

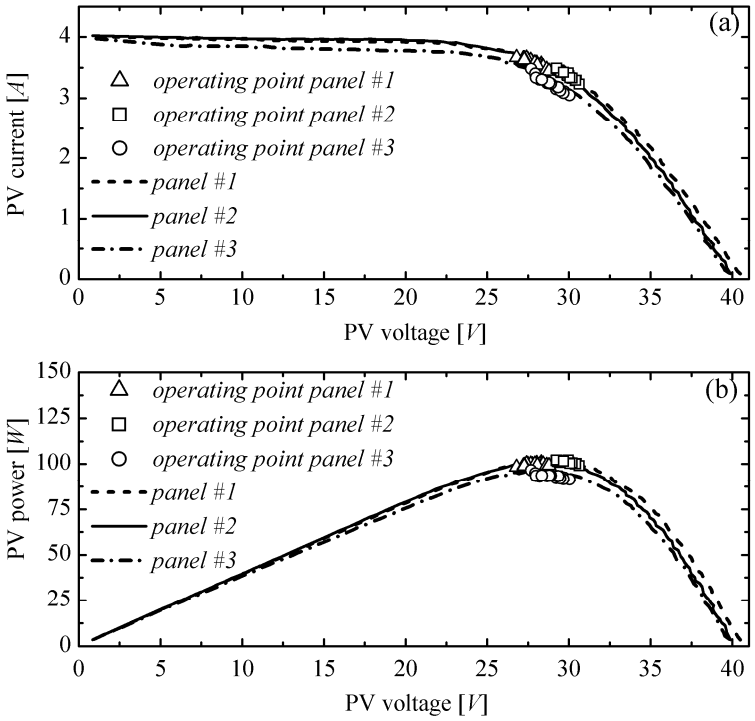

Fig 4.22 Uniform condition. Operating point positions corresponding to panel #1, panel #2, and panel #3 are superposed on the individual I-V curves (a) and P-V curves (b) corresponding to panel #1, panel #2 and panel #3.

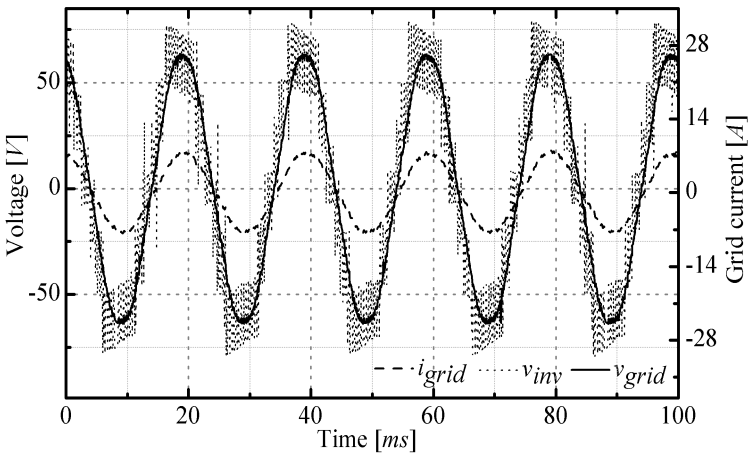

Fig 4.23 Time behavior in normal operation. The modulated voltage v_{inv} is compared to the grid voltage v_{grid}. The behavior of the output current i_{grid} is also reported.

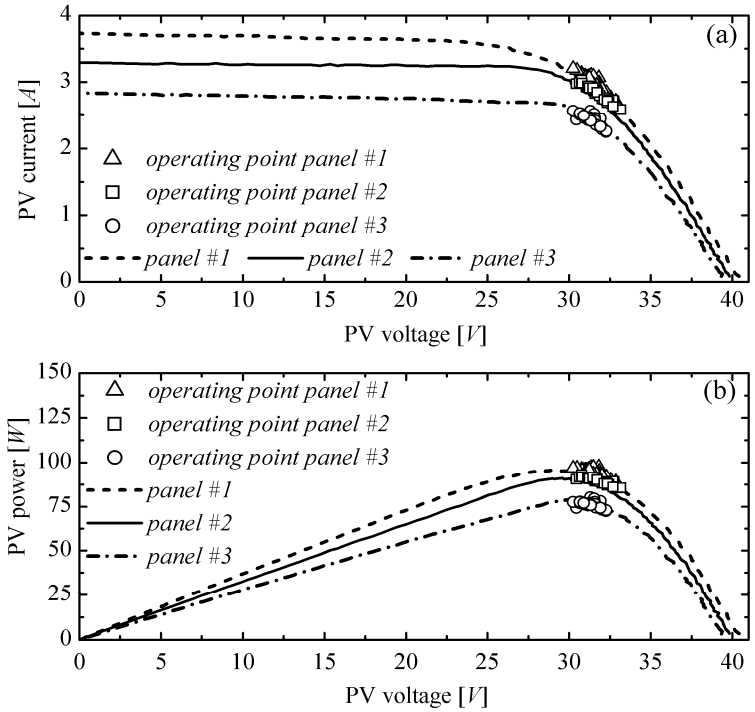

Fig 4.24 Mismatch condition. Operating point positions corresponding to panel #1, panel #2, and panel #3 is superposed on the individual I-V curves (a) and P-V curves (b) corresponding to panel #1, panel #2 and panel #3.

The inverter behavior was dynamically characterized while the system moved from uniform to mismatch conditions in order to monitor the dynamic performances. During the test, the irradiation of a single module (panel #1) was abruptly changed and the dc-link voltages along with the output waveforms were monitored.

Fig 4.25 reports the position of the operating points for each PV panel. During the test panel #2 and panel #3 were kept under almost same irradiance value (about 400 W/m^2). Initially, panel #1 was subjected to the same irradiance, after 6 s (see Fig 4.26) it was covered by a semitransparent filter reducing light intensity to about 250 W/m^2. Both sunny and shaded curves are reported in Fig 4.25. As can be seen the operating points of each solar panel are always close to its own MPP, thus evidencing the effectiveness of the distributed tracking procedure. All MPPs are well tracked even after obscuring panel #1. The static MPPT efficiency, calculated over an observation period of 2 s, during uniform irradiation was 99.5 %, while in

mismatch conditions this value slightly decreased to 98.5 %. As can be inferred from Fig 4.26, reporting the power delivered by panel #1 during the experiment, after obscuring (t=6 s), the solar panel achieved the new stable operating point almost instantly as the new MPP is reached after only 2 T_{MPPT} (the route followed by the operating point can be seen in Fig 4.25 by looking at the triangles between the shaded and the sunny curves). The same suitable behavior was observed when sunny conditions were again established (t=13 s). Fig 4.27, shows the current injected into the grid during both the high-low and low-high irradiance transitions (the time intervals shown in Fig 4.27a and Fig 4.27b are those comprise between the dashed lines drawn in Fig 4.26) and the grid voltage along with the multilevel voltage v_{inv} synthesized by the CHB. The results confirm the reliability of the system in dynamic conditions. In both transitions the current form is always in phase with the grid voltage so as to have an almost unit power factor (PF) (PF=0.982 in falling irradiation edge and PF=0.988 in the rising one).

To better quantify the enhancement of the overall MPPT efficiency due to the proposed distributed conversion approach, in Fig 4.28 the P-V and I-V curves measured in the last experiment, considering for the panel #1 the shaded characteristic, are illustrated along with the characteristics of a string composed by these three modules, taking also into account the bypass diodes effect on the shaded panel. In particular, three ideal diodes exhibiting a constant forward voltage of 1 V were considered. As expected, the power value corresponding to the global MPP (i.e. 137 W) is lower than the sum of the maximum power (i.e. 157.7 W) referring to the panels considered individually. This last value is the input power reached by the proposed approach, which exploits a distributed MPPT. Thus in this case this topology provides the same advantages of an AC-module approach.

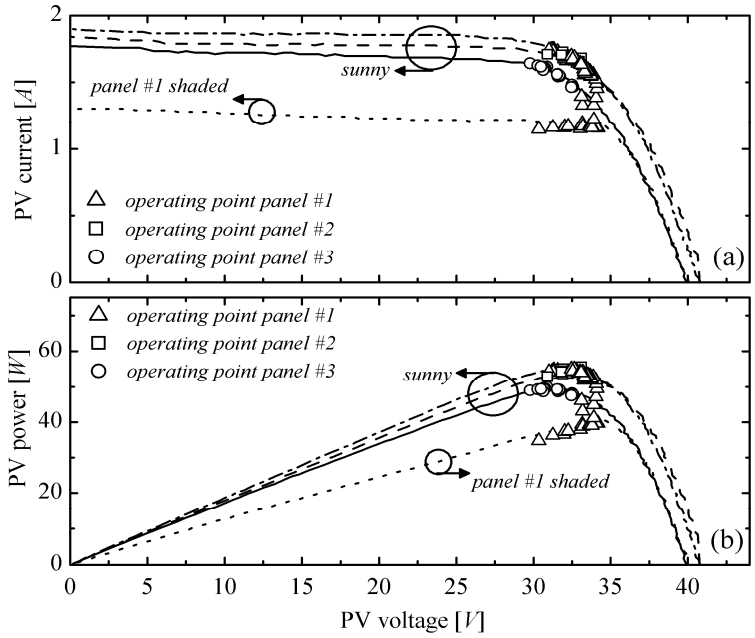

Fig 4.25 Sudden irradiation change. Operating point positions corresponding to panel #1, panel #2, and panel #3 are superimposed to the individual I-V curves (a) and P-V curves (b) corresponding to panel #1 in sunny condition, to panel #1 in shadow condition to panel #2 and to panel #3.

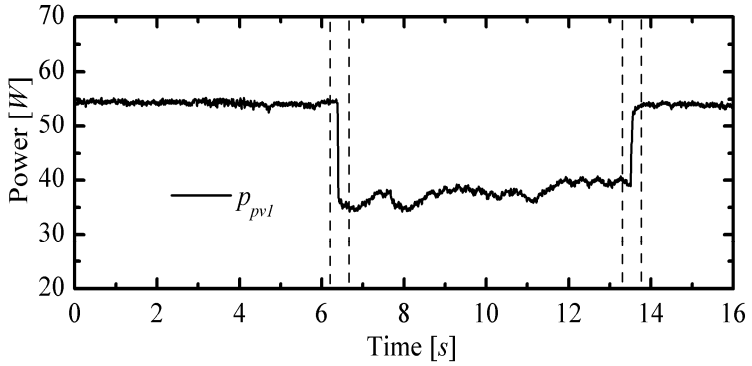

Fig 4.26 Sudden irradiation change. Panel #1 power time behavior.

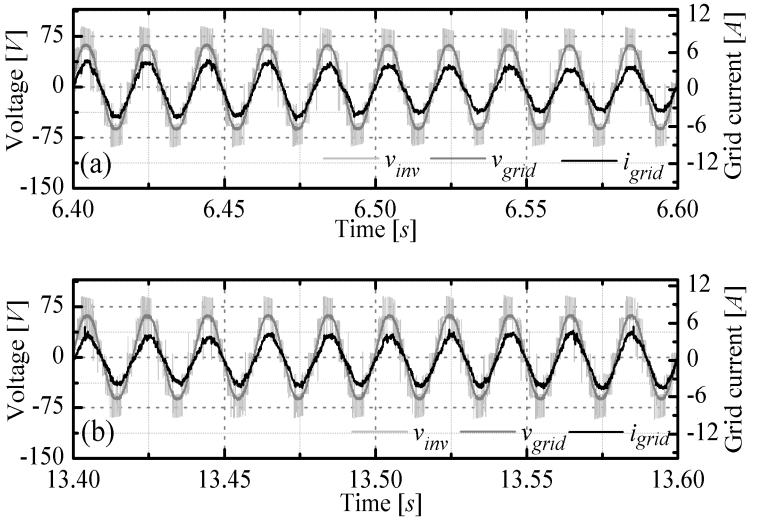

Fig 4.27 Sudden irradiation change. Grid voltage v_{grid}, grid current i_{grid}, and CHB modulated voltage v_{inv} against time during the falling (a) and the rising (b) irradiation edges of panel #1, respectively.

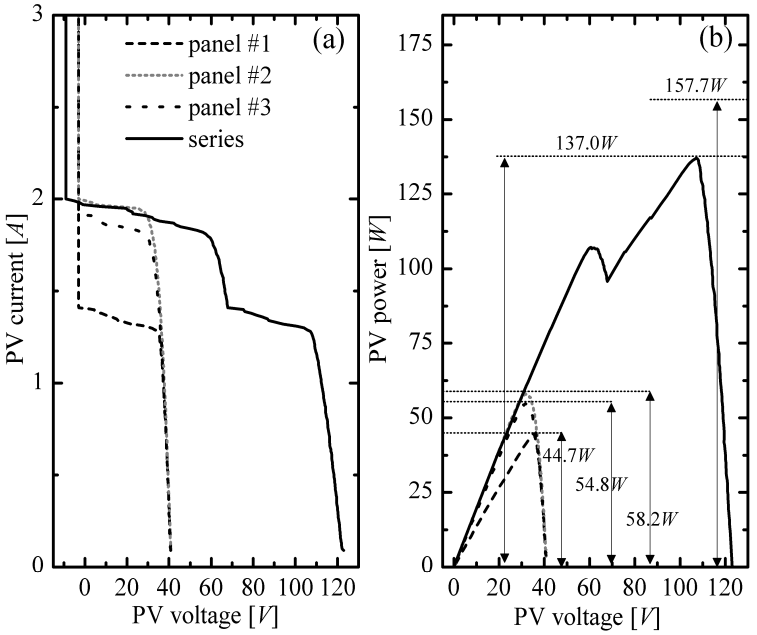

Fig 4.28 Centralized vs distributed MPPT conversion. In (a), I-V curves corresponding to the individual PV panels are compared to the curve of the series. In (b), the corresponding P-V curves are reported in order to highlights the difference in terms of producible power.

4.6 References

[1] L.G. Franquelo, J. Rodriguez, J.I. Leon, S. Kouro, R. Portillo, M. AM. Prats, “The age of multilevel converters arrives,” IEEE Industrial Electronics Magazine, vol.2, no.2, pp. 28-39, June 2008.

[2] O. Alonso, P. Sanchis, E. Gubia, L. Marroyo, "Cascaded H-bridge multilevel converter for grid connected photovoltaic generators with independent maximum power point tracking of each solar array," in Proc. IEEE 34th Annual PESC, 2003, pp.731-735.

[3] J.J. Negroni, F. Guinjoan, C. Meza, D. Biel, P. Sanchis, "Energy-Sampled Data Modeling of a Cascade H-Bridge Multilevel Converter for Grid-connected PV Systems," in Proc. 10th IEEE International Power Electronics Congress, Oct. 2006, pp.1-6.

[4] B. Xiao, F. Filho, L.M. Tolbert, "Single-phase cascaded H-bridge multilevel inverter with nonactive power compensation for grid-connected photovoltaic generators," in Proc. ECCE, 2011, pp.2733-2737.

[5] M.A. Rezaei, S. Farhangi, H. Iman-Eini, "Enhancing the reliability of single-phase CHB-based grid-connected photovoltaic energy systems," in PEDSTC, 2011, pp.117-122.

[6] E. Villanueva, P. Correa, J. Rodriguez, M. Pacas, "Control of a Single-Phase Cascaded H-Bridge Multilevel Inverter for Grid-Connected Photovoltaic Systems," IEEE Transactions on Industrial Electronics, vol.56, no.11, pp.4399-4406, Nov. 2009.

[7] J. Chavarria, D. Biel, F. Guinjoan, C. Meza, J.J. Negroni, "Energy-Balance Control of PV Cascaded Multilevel Grid-Connected Inverters Under Level-Shifted and Phase-Shifted PWMs," IEEE Transactions on Industrial Electronics, vol.60, no.1, pp.98-111, Jan. 2013.

[8] M. Coppola, F. Di Napoli, P. Guerriero, D. Iannuzzi, S. Daliento, and A. Del Pizzo, "An FPGA-based advanced control strategy of a grid tied PV CHB inverter," IEEE Transactions on Power Electronics, vol. 31, no. 1, pp. 806-816, Jan. 2016.

[9] M. Coppola, F. Di Napoli, P. Guerriero, A. Dannier, D. Iannuzzi, S. Daliento, and A. Del Pizzo, "Maximum power point tracking algorithm for gridtied photovoltaic cascaded Hbridge inverter," Electric Power Components and Systems, vol. 43, no. 8-10, pp 951-963, May 2015.

[10] M. Coppola, F. Di Napoli, P. Guerriero, A. Dannier, D. Iannuzzi, S. Daliento, and A. Del Pizzo, "FPGA implementation of an adaptive modulation method for a three-phase grid-tied PV CHB inverter," in Proc. IEEE 3rd International Conference on electrical systems for aircraft, railway, ship propulsion and road vehicles (ESARS), pp 1-10, 2015.

[11] F. Di Napoli, M. Coppola, P. Guerriero, D. Iannuzzi and S. Daliento, "Effective control strategy for photovoltaic cascaded H-bridge inverters developed on FPGA platform," in Proc. IEEE 11th Conference on Ph.D. Research in Microelectronics and Electronics (PRIME), pp 49-52, 2015.

[12] A. Eskandari, V. Javadian, H. Iman-Eini, M. Yadollahi, "Stable operation of grid connected Cascaded H-Bridge inverter under unbalanced insolation conditions," in Proc. 3rd International Conference EPECS, 2013, pp.1-6.

[13] B. Xiao, L. Hang, L. M. Tolbert., "Control of three-phase cascaded voltage source inverter for grid-connected photovoltaic systems," in Twenty-Eighth Annual IEEE APEC, 2013, pp.291-296.

[14] F. Filho, L.M. Tolbert, Yue Cao, B. Ozpineci, "Real-Time Selective Harmonic Minimization for Multilevel Inverters Connected to Solar Panels Using Artificial Neural Network Angle Generation," IEEE Transactions on Industry Applications, vol.47, no.5, pp.2117-2124, Sept.-Oct. 2011.

[15] H. Iman-Eini, J.-L. Schanen, S. Farhangi, J. Roudet, "A Modular Strategy for Control and Voltage Balancing of Cascaded H-Bridge Rectifiers," IEEE Transactions on Power Electronics, vol.23, no.5, pp.2428-2442, Sept. 2008.

[16] H. Sepahvand, L. Jingsheng, M. Ferdowsi, K.A. Corzine, "Capacitor Voltage Regulation in Single-DC-Source Cascaded H-Bridge Multilevel Converters Using Phase-Shift Modulation," IEEE Transactions on Industrial Electronics, vol.60, no.9, pp.3619-3626, Sept. 2013.

[17] Feel-Soon Kang, Sung-Jun Park, Su Eog Cho, Cheul-U Kim, T. Ise, "Multilevel PWM inverters suitable for the use of stand-alone photovoltaic power systems," IEEE Transactions on Energy Conversion, vol.20, no.4, pp.906-915, Dec. 2005.

[18] J. Rodriguez, S. Bernet, Bin Wu, J.O. Pontt, S. Kouro, "Multilevel Voltage-Source-Converter Topologies for Industrial Medium-Voltage Drives," IEEE Transactions on Industrial Electronics, vol.54, no.6, pp.2930-2945, Dec. 2007.

[19] B. Bahrani; S. Kenzelmann, and A. Rufer, "Multivariable-PI-Based dq Current Control of Voltage Source Converters With Superior Axis Decoupling Capability," IEEE Transactions on Industrial Electronics, vol.58, no.7, pp.3016-3026, July 2011.

[20] D. Iannuzzi, M. Pagano, L. Piegari, and P. Tricoli, "A star-configured cascade H-bridge converter for building integrated photovoltaics," Ninth International Conference on Ecological Vehicles and Renewable Energies (EVER), pp.1,7, 25-27 March 2014.

[21] Shell Solar Product Information Sheet, "Shell SQ150-PC Photovoltaic solar Module".

Chapter 5

5 Conclusions

In this thesis *high granularity* approaches have been presented, which are integrated in different levels of a PV system (monitoring, modeling and power conversion levels), in order to improve the PV yield, reducing the losses due to MPPT errors in *mismatch* conditions. In particular:

- An individual PV panel sensor network has been proposed. The sensor measures various key parameters of a PV panel, namely, short-circuit current, open-circuit voltage, and actual operating point without affecting the energy production. Moreover the sensor exhibits a wide operating area, working properly even under bypass condition of the host module.
- The sensor has been equipped by a panel voltage zeroing system for effectively zero all voltages and currents in a solar field. The circuit is based on the cooperation of a solid state switch, which allows single panel sectioniong, and an electromechanical relay, that effectively shorts circuit the external terminals of the solar panel. The short circuit condition is fully reversible.
- Both wireless and wired communication interfaces have been implemented, in particular the power line communication has been adopted as wired protocol.
- A wide experimental investigation has been performed in order to verify the effectiveness of the proposed high granularity monitoring system, tested in different configurations. It has been demonstrated that a proper inspection of the collected data allows gaining a complete insight into the behavior of the PV plant and its interaction with the inverter in all operating conditions.
- This information about the operation of each panel embedded in a PV string can strongly improve the overall efficiency of a PV system and the measurements have been employed to design

an information based MPPT algorithm. Experiments comparing the operation of a standard P&O algorithm with the proposed approach have demonstrated the capability of this new approach to locate the true MPP, thus avoiding power losses due to tracking failures. Moreover, a faster convergence has been reached with respect to a classic P&O algorithm.

- The measurements, collected by the sensor, have been also exploited to perform an automatic PV system reconfiguration. The proposed method allows unambiguous identification of cases where bypassing is effective. Tests have evidenced the reliability of the proposed reconfiguration approach.
- A high granularity circuit model of a PV field has been implemented in an automated tool for a fast evaluation of the PV yield. The model takes into account the electrothermal effect which takes place into a PV module. The tool is based on the interaction between various commercial software packages (AutoCAD, Matlab, and PSpice) so as to enjoy several appealing features: (i) it is fully automated; (ii) it employs accurate formulations to compute the relative position of the PV plant under test with respect to the Sun, the solar irradiance; (iii) contrarily to other approaches which adopt complex mathematical methods, the shadow evaluation is effectively performed also in the cases of geometric complex obstacles; (iv) a high granularity circuit cell level description of the whole PV plant is considered, thus obtaining accurate simulation results; (v) in spite of the fine discretization, very low computation time is required in comparison to analogous numerical methods.
- The tool represents a first attempt to perform dynamic ET simulations of PV plants. The approach relies on the automatic generation of an electrical equivalent macrocircuit representing ET behavior of the single PV module, which can be solved by PSpice like simulators. The approach has been used to determine the detrimental influence of architectural shading on the dynamic ET behavior of a PV string. Circumscribed overheating mechanisms have been detected and explained. In addition to the increase in the accuracy of the energy yield estimation, the proposed approach is particularly indicated to support and ease the analysis and interpretation of aerial thermography data, nowadays employed to perform diagnostics of PV field.
- The tool has been validated by analyzing some scenarios where the shadows are produced by small obstacles, which

are complex to handle by available commercial tools devised for the design of PV systems. In particular, it has been found that the effects of small area shadows cannot be a priori neglected. Moreover, the tool has also been exploited to examine the detrimental impact of self-shading and masking mechanisms, typically occurring in poorly designed PV plant with crammed rows. It is concluded that the tool can successfully contribute to improve the system design and to find the optimum power conversion topology for the PV field under test, so as to maximize the annual collected energy, as well as to provide a fast, yet accurate, estimation of the yield of installed plants.

- The results of this tool have contributed to determine the optimum level of granularity of the conversion topology to adopt in a given PV field, in particular the *cascaded multilevel converter* topology has been investigated, where a certain number of solar panels are connected to dedicated H-bridges. The optimum number of PV modules for each cell along with the number of the cells can be found by means of this proposed tool.
- A novel control strategy for this converter has been presented, which overcomes the issues related to its applicability in a PV system. The new approach is based on a mixed staircase-PWM techniques, so as to join advantages of single stage converters with MPPT capabilities of distributed converter topologies. The special sorting procedure allows just one H-bridge to operate in PWM mode while the others are "blocked", thus achieving a significant reduction of the dynamic power dissipation. Experiments performed on a three cells one phase prototype have evidenced the correct operation of the proposed approach.
- The control strategy has been extended to a three phase structure and the reliability of the proposed approach has been evidenced by means of Matlab/Simulink analysis showing the capability of system to take under control all relevant parameters: power factor; balance of the currents; solar panel maximum power points. Performance has been investigated under both uniform and mismatch conditions, other than under dynamic changing conditions.

This work has also accomplished the task to solve some questions and issues concerning the PV application and illustrated in the first chapter of this work:

1) How can I find effectively where the problem is located in a PV field?
2) Can I access to a PV field safely?

3) Why my PV field does not provide the return of money I expected?
4) Which is the best power conversion topology in terms of cost and energy yield?
5) Is there a high modular high granularity conversion topology to improve my energy yield?

The proposed high granularity monitoring approach can simplify the process of locating possibly failures into a PV plant. Moreover the disconnection section and the PLC interface of this sensor can be exploited as a secure system to "switch off" the dangerous voltages presented on a PV field during daylight, thus guaranteeing safe access. The results obtained through the high granularity model exploited in the proposed tool have shown that the commercial software are not able to estimate correctly the energy yield of a PV plant, since they are not able to take properly into account the losses due to small area shadows and the ET effects presented in a PV module. Moreover the tool can be exploited to evaluate the best conversion topology to adopt for a given PV plant. Lastly the CHB topology seems to be a high modular high granularity conversion topology able to improve the energy yield of a PV plant, overcoming the drawbacks of the AC-module approach.

6 List of publications

[1] V. d'Alessandro, F. Di Napoli, P. Guerriero, and S. Daliento, "An automated high-granularity tool for a fast evaluation of the yield of PV plants accounting for shading effects," Renewable Energy, vol. 83, pp. 294-304, November 2015.

[2] P. Guerriero, F. Di Napoli, V. d'Alessandro, and S. Daliento, "Accurate maximum power tracking in photovoltaic systems affected by partial shading," International Journal of Photoenergy, vol. 2015, Article ID 824832, 10 pages, 2015.

[3] M. Coppola, F. Di Napoli, P. Guerriero, A. Dannier, D. Iannuzzi, S. Daliento, and A. Del Pizzo, "Maximum power point tracking algorithm for gridtied photovoltaic cascaded Hbridge inverter," Electric Power Components and Systems, vol. 43, no. 8-10, pp 951-963, May 2015.

[4] P. Guerriero, G. Vallone, F. Di Napoli, V. d'Alessandro, and S. Daliento, "Monitoring and Diagnostics of PV Plants by a Wireless Self-Powered Sensor for Individual Panels," IEEE Journal of Photovoltaic, vol. 6, no 1, pp 286-294, Jan. 2016.

[5] M. Coppola, F. Di Napoli, P. Guerriero, D. Iannuzzi, S. Daliento, and A. Del Pizzo, "An FPGA-based advanced control strategy of a grid tied PV CHB inverter," IEEE Transactions on Power Electronics, vol. 31, no. 1, pp. 806-816, Jan. 2016.

[6] F. Di Napoli, P. Guerriero, V. d'Alessandro, and S. Daliento, "Single panel voltage zeroing system for safe access on PV plants," IEEE Journal of Photovoltaic, vol. 5, no. 5, pp. 1428-1434, Sept. 2015.

[7] P. Guerriero, F. Di Napoli, F.Cominale, V. d'Alessandro, and S. Daliento, "Accurate analysis of small shadows effects on photovoltaic systems yield," in Proc. IEEE International Symposium on Power Electronics, Electrical Drives, Automation and Motion (SPEEDAM), 2014, pp. 987-992.

[8] P. Guerriero, F. Di Napoli, V. d'Alessandro, and S. Daliento, "A wireless controlled circuit for PV panel disconnection in case of fire," in Proc. IEEE International Symposium on Power Electronics, Electrical Drives, Automation and Motion (SPEEDAM), 2014, pp. 982-986.

[9] P. Guerriero, G. Vallone, M. Primato, F. Di Napoli, L.Di Nardo, V. d'Alessandro, and S. Daliento, "A wireless sensor network for the monitoring of large PV plants," in Proc. IEEE International Symposium on Power Electronics, Electrical Drives, Automation and Motion (SPEEDAM), 2014, pp. 960-965.

[10] M. Coppola, P. Guerriero, F. Di Napoli, S. Daliento, and D. Lauria, "A PV AC-module on coupled-inductors boost DC/AC converter," in Proc. IEEE International Symposium on Power Electronics, Electrical Drives, Automation and Motion (SPEEDAM), 2014, pp. 1015-1020.

[11] F. Di Napoli, V d'Alessandro, S. Daliento, and P. Guerriero, "Accurate yield prediction for PV plants in the presence of shadows due to fully arbitrary obstacles," in Proc. 46th Conference del Gruppo Elettronica (GE), 2014.

[12] F. Di Napoli, P. Guerriero, V d'Alessandro, and S. Daliento, "A power line communication on DC bus with photovoltaic strings," in Proc. IET 3rd Renewable Power Generation Conference (RPG), 2014, pp. 8.16-8.16.

[13] V. d'Alessandro, F. Di Napoli, P. Guerriero, and S. Daliento, "A novel circuit model of PV cell for electrothermal simulations," in Proc. IET 3rd Renewable Power Generation Conference (RPG), 2014, pp. 7.3.4-7.3.4.

[14] M. Coppola, F. Di Napoli, P. Guerriero, A. Dannier, D. Iannuzzi, S. Daliento, and A. Del Pizzo, "FPGA implementation of an adaptive modulation method for a three-phase grid-tied PV CHB inverter," in Proc. IEEE 3rd International Conference on electrical systems for aircraft, railway, ship propulsion and road vehicles (ESARS), 2015, pp 1-10.

[15] P. Guerriero, F. Di Napoli, V. d'Alessandro and S. Daliento, "Dynamic reconfiguration of solar systems for avoiding MPPT faults due to architectural partial shading," in Proc. IEEE 15th Internetional Conference on Environment and Electrical Engineering (EEEIC15), 2015, pp 1229-1234.

[16] V. d'Alessandro, A. Magnani, L. Codecasa, F. Di Napoli, P. Guerriero, and S. Daliento, "Dynamic Electrothermal Simulation of

Photovoltaic Plants," in Proc. IEEE International Conference on Clean Electrical Power (ICCEP), 2015, pp 682-688.

[17] P. Guerriero, F. Di Napoli, V. d'Alessandro and S. Daliento, "Experimental comparison between an “information based” MPPT algorithm and standard P&O in both partial shading and uniform illumination," in Proc. IEEE International Conference on Clean Electrical Power (ICCEP), 2015, pp 610-616.

[18] F. Di Napoli, M. Coppola, P. Guerriero, D. Iannuzzi and S. Daliento, "Effective control strategy for photovoltaic cascaded H-bridge inverters developed on FPGA platform," in Proc. IEEE 11th Conference on Ph.D. Research in Microelectronics and Electronics (PRIME), 2015, pp 49-52.

Under review and submitted

[19] S. Daliento, F. Di Napoli, P. Guerriero and V. d'Alessandro, "A modified bypass circuit for improved hot spot reliability of solar panels subjected to partial shading," under revision in Solar Energy.

[20] M. Coppola, F. Di Napoli, P. Guerriero, A. Dannier, D. Iannuzzi, S. Daliento and Andrea Del Pizzo, "Distributed MPPT approach for a three-phase grid-tied cascade inverter," under revision in Solar Energy.

[21] F. Di Napoli, A. Magnani, M. Coppola, P. Guerriero, V. d'Alessandro, L. Codecasa, P. Tricoli and S. Daliento, "Real-time temperature cycling estimation of IGBT power modules with power in-line measurements and compact thermal modeling," under revision in IET 5rd International Conference on Renewable Power Generation (RPG), 2016.

[22] A.Magnani, M.Riccio, F. Di Napoli, P. Guerriero, L.Codecasa, V. d’Alessandro, G.Breglio, S. Daliento, A.Irace and N.Rinaldi "Thermal Feedback Blocks for Fast and Reliable Electro-Thermal Circuit Simulation of Power Circuits at Module Level," accepted for presentation at 28th International Symposium on Power Semiconductor Devices and ICs (ISPSD), 2016.

[23] P. Guerriero, F. Di Napoli, V. d'Alessandro and S. Daliento, "Real time monitoring of solar fields with cost/revenue analysis of fault fixing," accepted for presentation at IEEE International conference on Environment and Electrical Engineering (EEEIC), 2016.

[24] P. Guerriero, F. Di Napoli, V. d'Alessandro and S. Daliento, "A new bypass circuit for hot spot mitigation," accepted for presentation at 23rd

International Symposium on power electronics, electrical drives, automation and motion (SPEEDAM), 2016.

7 Ringraziamenti

Prendendo spunto da un mio collega e carissimo amico, dopo aver presentato in inglese il mio lavoro e i risultati conseguiti nella mia tesi, preferisco utilizzare la mia lingua per esprimere al meglio i miei ringraziamenti a tutti coloro che mi hanno accompagnato in questo percorso di vita e di studio.

Innanzi tutto sono estremamente grato al prof. Santolo Daliento per l'esperienza che mi ha concesso di vivere in questi tre anni di dottorato di ricerca, per i suoi insegnamenti, per la pazienza con cui ha sopportato le mie ansie e soprattutto per i consigli da padre (non da professore) che spesso mi ha dato. Non dimenticherò mai la sua vicinanza quella mattina in ospedale.

Un immenso grazie va a Pierluigi Guerriero, già correlatore della mia tesi specialistica e oggi amico fidato oltre che collega validissimo. La sua disponibilità verso i problemi di chiunque e la sua dedizione alle diverse attività di ricerca, sono state di esempio e stimolo per una continua crescita professionale e umana.

Ringrazio il prof Vincenzo d'Alessandro per avermi dato la possibilità di collaborare in alcune delle sue ricerche, condividendo la sua professionalità e conoscenza con il suo solito modo impeccabile. Inoltre lo ringrazio per avermi trattato da amico, allietando i pranzi all'università e le gite al "*little truck*" con la sua simpatia.

Voglio ringraziare il prof Diego Iannuzi per avermi dato la possibilità di lavorare con il gruppo di elettrica, facendo accrescere le mie conoscenze circa l'elettronica di potenza, materia che sempre mi ha affascinato e che non è stata trattata con sufficiente dettaglio durante il percorso di laurea. Lo ringrazio inoltre, insieme al prof Andrea Del Pizzo e Adolfo Dannier, per la possibilità offertami di poter continuare a lavorare nel gruppo e per la fiducia accordata che spero possa essere ampiamente ripagata.

Un grazie speciale a Marino Coppola per aver instaurato con me, da subito, un rapporto di amicizia, senza mai mettermi pressione

nelle continue scadenze che incorrono nel lavoro. Lo ringrazio soprattutto per la sua disponibilità e affetto.

Un sentito grazie, poi, al prof. Pietro Tricoli dell'*University of Birmingham* per avermi offerto ospitalità nel suo gruppo di ricerca, pur trovandosi a vivere un periodo non facilissimo della sua vita.

Sono molto contento di aver avuto l'occasione di stringere amicizia con il gruppo degli "optoelettronici" che, pur con la loro indiscutibile professionalità, rendono comunque il lavoro all'Università pieno di sorrisi e di momenti di condivisione. Grazie per avermi fatto sentire anche parte del loro gruppo. In particolare sono grato a Gianpaolo Romano per la sua amicizia e la sua disponibilità sin dal nostro primo incontro, nei banchi dell'aula T4 durante la prova scritta di ammissione al dottorato di ricerca. Spero che con il tempo lui riesca a comprendere che deturpare i tergicristalli delle macchine altrui è un reato perseguibile penalmente.

Un grazie speciale ad Alessandro Magnani, collega dalla preparazione eccezionale e amico unico, lo ringrazio, professionalmente per la collaborazione offerta in alcuni dei lavori pubblicati durante questi tre anni e lo ringrazio, da amico per aver supportato le mie idee e ancor di più per aver visto in me una persona di cui potersi fidare.

Un grazie immenso a Darjn Esposito, mio vicino di scrivania, la sua amicizia è il regalo più bello di questa esperienza. Non dimenticherò mai quando il laboratorio diventava il peggior vicolo di Napoli nei momenti in cui i risultati del lavoro non erano quelli attesi o quando gli impegni di lavoro diventavano numerosi. Lo ringrazio per essermi stato molto vicino nelle difficoltà di questi tre anni, per il supporto e il sincero affetto che mi ha sempre mostrato.

Un grazie particolare a Pasquale Cennamo, che mi ha reso parte della sua vita mostrandomi un affetto fraterno, a lui va la mia ammirazione più profonda per il coraggio e la dignità impareggiabile con cui affronta le difficoltà che la vita gli presenta.

Ringrazio la mia famiglia, i miei cari che oggi non ci sono più, i miei sette zii Fumo con le loro rispettive famiglie, i miei cugini, i miei amici di vecchia data e quelli recenti, perché sono stati, sono e saranno sempre la mia continua fonte di forza. Soprattutto voglio ricordare Teresa e dirle grazie per ogni momento indimenticabile che mi ha fatto vivere e in particolare per quella notte del 29/11/2014 in cui, come la sorella che non ho mai avuto, non mi lasciò solo. A Marco ed Oriana un grazie speciale per avermi accolto nelle loro

famiglie e per l'affetto fraterno, il sostegno e i momenti indimenticabili che mi hanno donato. La mia profonda gratitudine va a Fabio, Luca, Antonella, Valentina, Marina, Nando e Dario, per essere stati sempre il timone nella mia vita, soprattutto in quei momenti in cui la mia bussola aveva perso il Nord. Un grazie dolce a Raffaella e a sua madre per tutto e in particolare per l'aiuto offertomi in Inghilterra, a Raffy la mia stima incondizionata per l'esempio di caparbietà, fede e tenacia con cui affronta la vita.

Non posso non dimenticare l'amico di sempre Antonio, con lui ho affrontato tutto il mio percorso scolastico e non solo, purtroppo non riesco a vederlo come una volta, ma lo ringrazio per essere un punto fisso nella mia vita, un esempio e, a prescindere da tutto, un sicuro conforto in tutte le difficoltà che la vita potrà riservarmi.

Vorrei ringraziare tutte le persone che conosco, ogni volto che ho incontrato nella mia vita, perché ognuno di loro, nel bene o nel male, ha contribuito a quello che sono oggi, insegnandomi qualcosa di unico.

Infine non posso non ringraziare Nicoletta che, pur arrivando alla fine di questo percorso, ha subito contribuito in maniere forte con il suo sostegno, soprattutto nella stesura di questo elaborato. La ringrazio per essere così speciale nella mia vita e per aver condiviso questa sua unicità con me.

Ora per me inizia un nuovo capitolo della vita, ma vi porterò tutti con me nelle mie prossime avventure.

sii tu il cambiamento
che vuoi vedere nel mondo